EFFECTS OF HYDROPHOBIC SURFACE TREATMENTS

ON DROPWISE CONDENSATION AND FREEZING OF WATER

A Dissertation

by

JOHN ARTHUR BRYANT

Submitted to the Office of Graduate Studies of
Texas A&M University
in partial fulfillment of the requirements for the degree of

DOCTOR OF PHILOSOPHY

December 1995

Major Subject: Mechanical Engineering

UMI Number: 9615775

UMI

300 North Zeeb Road
Ann Arbor, MI 48103

EFFECTS OF HYDROPHOBIC SURFACE TREATMENTS

ON DROPWISE CONDENSATION AND FREEZING OF WATER
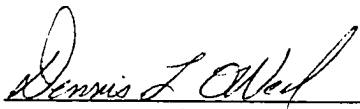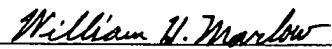
A Dissertation

by

JOHN ARTHUR BRYANT

Submitted to Texas A&M University
in partial fulfillment of the requirements
for the degree of

DOCTOR OF PHILOSOPHY

Approved as to style and content by:
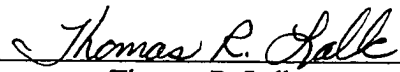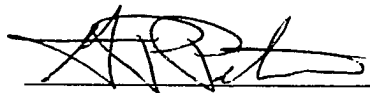
Dennis L. O'Neal	William H. Marlow
(Chair of Committee)	(Member)
Thomas R. Lalk	G. P. Peterson
(Member)	(Member)

G. P. Peterson
(Head of Department)

December 1995

Major Subject: Mechanical Engineering

ABSTRACT

Effects of Hydrophobic Surface Treatments on Dropwise Condensation

and Freezing of Water. (December 1995)

John Arthur Bryant, B.S., New Mexico State University;

M.S., University of Texas at El Paso

Chair of Advisory Committee: Dr. Dennis L. O'Neal

The effects of hydrophobic coatings on the dropwise condensation process for a flat horizontal copper plate held at a temperature much lower than the surrounding air was investigated. Extensive qualitative and quantitative data were taken to describe these effects in terms of dropsize distributions, heat and mass transfer coefficients, and digital imaging of the microscopic condensing droplets in terms of various extensive properties.

Conditions of the tests were laminar flow (Reynolds numbers of 600 to 1600), condensing surface temperature of -10.0°C, air temperatures of 1.5 to 7.5°C, and relative humidities of 50 to 90%. Digital imaging of the condensation process was done using a medium power microscope coupled to a solid-state camera and a computer-based image capture system. Three different treatments were used on the polished copper condensing surface; no coating, a silicone conformal coating, and a long-chain sulfur based coating. Results for the heat transfer data showed an increase of approximately 33% for condensation over a dry surface for the conditions of the study. The mechanism of condensation appeared consistently to be dropwise. A method to predict the Nusselt number, nucleation time, mean cluster size and the droplet surface density in terms of extensive properties that are known a priori was also developed based on the experimental data.

A condensation model was developed based on heat transfer relationships for the condensation process and the psychrometric qualities of the ambient air. The inputs to the model were the surface temperature of the condensing system, the contact angle of the liquid phase in contact with the surface, the moisture content and temperature of the air stream, and the velocity of the air flowing over the condensing surface. Comparisons were made between the experimental results and those predicted by the model for dropsize distributions and mass of condensate on the surface. The results from the model were within ±25% of the experimental values.

It was found that the application of a hydrophobic coating on a surface that is to be operated at a temperature below the freezing point of water will delay the onset of ice nucleation by 15 to 35% over an uncoated surface.

To my love, Elizabeth

To my son, Stephen

To my Father, Frank

To my Mother, Florence

To Pauline and Jack

ACKNOWLEDGMENTS

I am very fortunate to have had the guidance and friendship of Dr. Dennis O'Neal during my studies. He had a keen insight into complex problems and invariably seemed to know which path to take. I know my committee members had busy schedules and I would like to thank them for taking the time to serve on my committee and offer help and suggestions when I had questions. Dr. Lalk, as always, seemed to ask those questions whose answers begged true understanding of the subject.

My wife, Elizabeth, who put up with many late nights and listened patiently while I tried out concepts. Her help with keeping our daily lives going can never truly be compensated.

Jack and Pauline Whitehead hold a special place in my heart. They have supported Elizabeth and me in many ways since we started our undergraduate education many years ago. I can never thank them enough.

TABLE OF CONTENTS

LIST OF FIGURES

FIGURE   Page

FIGURE   Page

FIGURE
Page

LIST OF TABLES

CHAPTER I

INTRODUCTION

Air-to-air heat pumps are capturing an increasing share of the market for heating systems in Texas and the southeastern United States. During the past 15 years, manufacturers have implemented many improvements in heat pumps such as improved heat transfer surfaces, compressors, and fan designs. These changes have increased the seasonal heating efficiency and reliability of the systems.

A phenomenon that continues to adversely affect the heating efficiency of heat pumps is the frost that forms on the outdoor heat exchanger during periods of mild winter weather. Typical conditions conducive to frost formation are outdoor temperatures ranging from -10° to 7°C and outdoor relative humidities above 50% (ASHRAE 1993). When a heat pump system is operating in the heating mode, the outdoor heat exchanger (evaporator) is operating below the freezing point of the water vapor in the surrounding air. As water vapor condenses on the evaporator it subcools, coalesces into droplets, and with further subcooling nucleates to ice. The ice embryos provide the sites for subsequent frost growth.

The frost growth process and it's effects on heat transfer to a heat exchanger have been extensively studied (O'Neal and Tree 1985, Tao and Besant 1993). Frost growth on a heat pump evaporator surface reduces airflow and, coincidentally, the capacity of the system. Eventually, the heat pump must be switched to the defrost mode that allows hot refrigerant gas to be circulated through the evaporator. This causes the frost to melt and drain away from the evaporator surface. At the end of the defrost period, the heat pump switches back to the heating mode and the process begins again. The normal defrost cycle used by U.S. manufacturers is called the

---

This dissertation follows the form of the A.S.M.E. *Journal of Heat Transfer.*

reverse-cycle defrost. During the reverse-cycle defrost, the unit operates in the air conditioning mode with the outdoor fan off. Because the unit is extracting heat from the building during the defrost, electric backup heat must be run simultaneously to maintain temperatures in the building. Defrost times typically take five to ten minutes with this technology (ASHRAE 1991).

Studies at Oak Ridge National Laboratory have indicated that frosting/defrosting losses may degrade the seasonal heating efficiency of heat pumps by as much as 20% (Baxter and Moyers 1983). Early studies at Ontario Hydroelectric identified several ways to reduce frosting/defrosting losses including a low leakage reversing valve, heat exchanger redesign and modified defrost initiation scheme (Young 1980). A more recent study at Texas A&M University identified a change in defrost method (called the two-stage defrost) that could reduce the energy penalty of the defrost cycle by as much as 9% (O'Neal et al. 1989). Reducing the energy penalty of the frost/defrost cycle on heat pumps could have a significant impact on future electrical energy use in Texas and areas where heat pumps are applied.

To date, there have been no studies done on developing or application of a hydrophobic coating that would prevent or delay ice/frost growth on a heat pump heat exchanger surface. There have been numerous investigations into the application of hydrophobic coatings for ships or structures which are subject to severe icing (Katoh et al. 1989). additionally, much work has been done concerning application of these coatings on aircraft lifting surfaces (Itagaki 1983a). These studies have shown that ice will not form as quickly on a hydrophobic surface as it does on an uncoated surface and that there is a marked reduction in the adhesion strength of ice to a substrate surface with a hydrophobic coating.

Background

Condensation occurs when a vapor contacts a solid surface that is held at a temperature lower than the saturation temperature of the vapor. One of the main objectives of condensation research has been to quantify various effects on the condensation mass flux and the heat flux at the cooling surface, to which heat is transferred through the condensate (Fujii 1991). Condensation is characterized as either film or dropwise depending on whether or not the condensate has an affinity for the condensing surface. This affinity of a liquid for a surface defines the wettability of the fluid. The bulk of research on water vapor condensation seems to be focused on steam and various condenser geometries and almost all of these studies have been performed under steady-state conditions.

In a preliminary study conducted by the author, two thin plates of aluminum and copper were coated with a hydrophobic polymer and two were left untreated. The plates were mounted onto a heat exchanger that allowed control of the plate surface temperature. During free convective condensation and frost growth experiments, the plates were cooled rapidly and held at a surface temperature below the freezing point of water. Water droplets were observed condensing on the surface of the plates and coalescing until they nucleated to ice. At that time, the frost growth phase began and continued until defrost was initiated. Significantly, there was a five to ten minute delay in the times for ice nucleation to occur for the coated versus the uncoated plates. It was also determined from these early experiments that the primary difference between the treated and untreated surfaces seemed to be the terminal droplet size and size distribution prior to ice nucleation. The terminal droplet size could be described as the average water droplet size just prior to nucleation to ice. The subsequent variance in frost characteristics appeared to arise from these differences.

The purpose of this study was to quantify the distribution of drop sizes occurring on a cold surface undergoing condensation and ultimately, ice and frost growth. The study was carried out utilizing wettable metal surfaces and metal surfaces treated with a hydrophobic polymer. The primary focus of the study was to identify factors that most influence water droplet size and distribution during the condensation process. The temporal emphasis was from the beginning of condensation through nucleation to ice embryos. Microscopy imaging and digital imaging techniques were used to quantify the condensation process for droplet diameters in the 10 to 200 micrometer range. This same technique was used to characterize the droplet contact angle on surfaces with different treatments that are known to affect droplet nucleation (Carey 1992a). This research should increase the understanding of the transient condensation process and lead to better methods of frost and ice control on cold surfaces.

Chapter II presents a review of the applicable literature to the problem of condensation, drop size distributions, and hydrophobic surface treatments. Chapter III describes the experimental apparatus and procedures used during the study. Chapter IV presents the results and discussion of the experimental work. Modeling and simulation of the dropwise condensation process and dropsize distributions are described in Chapter V. Chapter VI presents a comparison and discussion of the model and experimental results. Chapter VII presents conclusions and directions for future work.

CHAPTER II

LITERATURE REVIEW

There is an extensive collection of literature available that describes the general characteristics and mechanisms of dropwise condensation and frost growth for different flow conditions and flow geometries. Additionally, there is a diverse body of work available on hydrophobic surface coatings. However, there is little information concerning either steady or transient condensation of atmospheric water vapor onto a surface held below the freezing point of the surrounding water vapor/air mixture. There also seems to be a lack of literature on the very early stages of condensation and ice/frost nucleation that address the effect of the droplet distributions on heat transfer to the surface. The present work draws from several distinct areas of interest and as such the applicable literature was arranged into the following sections:

1. Hydrophobic Surfaces - Most hydrophobic surface literature describes adhesion reduction of contaminants to the surface, impact on contact angle for various fluids, and promotion of dropwise condensation in steam systems.

2. Condensation - The bulk of this work is confined to steam condensation but basic mechanisms are applicable.

3. Drop Size Distributions - The majority of the literature describes drop size distributions in terms of steam systems.

4. Early Stage Heat and Mass Transfer - Work was identified that described the early microscopic stages of condensation and drop growth rate.

Each of these sections will be fully discussed and the relevance to the present study emphasized.

Hydrophobic Surfaces

For applicable heat and mass transfer processes, the occurrence of icing and/or frosting can either be beneficial or inconvenient. Investigation into the frosting problem on HVAC coil surfaces only began in the late 1950's. Today there are thermal storage systems that take advantage of the ice growing process to store "cooling energy" in ice tanks for use at times of peak cooling loads. In either case, the control and removal of accumulations of frost and/or ice is a difficult process and an on-going topic of research interest. In any of the applications mentioned above, there have been specific research efforts conducted into the fundamentals of the icing process as well as methods to prevent or delay the onset of the icing process.

If the temperature of a surface exposed to a humid air stream is at or below the freezing point, water will condense and a layer of porous ice crystals will form. In the case of refrigeration equipment, this process occurs when one opens the freezer compartment of a refrigerator. The frost layer continues to grow and through simultaneous heat transfer and mass diffusion, the layers become more dense and thick as the frost grows outward. The heterogeneous nucleation of ice is different only in that the process involves the ice-water interface directly instead of resulting from the growth of frost from the air-water vapor process. Recently, Saito and Tokura (1991) reviewed the literature concerned with the frosting process on cold surfaces. They classified the literature into categories depending on the frosting phenomena; frost formation in forced (flat plates, cylinders, tubes, heat exchangers) and natural convection (flat plates, horizontal cylinders, narrow spaces), frost formation in cryogenic temperatures, heat and mass transfer coefficients on the surfaces of frost layers, thermal properties of frost and methods for predicting the growth rate of frost layers, and other recent studies on frost formation. In their review, they stated that

successful methods to prevent frosting on cold surfaces had not yet been developed. There have been methods developed which delay or allow effective removal of an ice and or frost layer. Pingry and Engdahl (1965) reviewed the literature and some of the studies underway at that time concerning the ice-frost phenomena. They also categorized frost-ice control schemes as either *prevention* or *removal*. They felt that hydrophobic surfaces alone would not prevent ice or frost formation, but they could delay the formation and decrease the adhesion strength of the formation. Ice-frost removal systems were classified as either mechanical or thermal. They felt that these were "brutish" methods and were hopeful that if enough knowledge could be developed about ice adhering to engineering surfaces, its' formation could then be controlled.

The United States Environmental Protection Agency (EPA) funded a project to develop a hydrophobic coating for pavement that would mitigate ice or frost growth (Ahlborn 1976). The researchers followed traditional theories for choosing which of the (then) commercially available hydrophobic coating materials to test. Their criteria was based on Young's equation for surface energy and the Dupre' equation for the work of adhesion. Measurements of the contact angle θ are used to estimate the work of adhesion. From Young's equation,

$$\cos\theta = (\sigma_{sv} - \sigma_{sl})/\sigma_{lv} \qquad\qquad 2.1$$

where σ is the interfacial (surface) tension between the phases and s, l, and v refer to the solid, liquid and vapor phases respectively. When combined with the Dupre' equation for reversible adhesion work yields,

$$W_A = \sigma_{lv}(1+\cos\theta) + RT \int_p^{p_o} \frac{\Gamma}{p}\, dp = \sigma_{lv}(1+\cos\theta) + \pi_{sv} \qquad\qquad 2.2$$

Here Γ was the surface concentration of the vapor adsorbed from the liquid and p and p_o are the vapor pressure and saturated vapor pressure respectively. This equation

assumes that any change in W_A due to the solidification of water is negligible. From equation 2.2, if the work of adhesion is to be minimized the surface energy of the material must be as small as possible and the contact angle should be as large as possible. From these basic theories, they determined that a truly hydrophobic coating must have the following characteristics: minimum surface energy, a thickness of several thousand angstroms (helps to overcome long-range forces through many monolayers), virtually no solubility in water, and a contact angle as large as possible with a minimum value of 60 degrees on a smooth surface. However, they noted that molecular orientation was important and that the chemical species dominating the surface coating controlled the surface energy. To help overcome the long-range forces, they suggested that inert binders be used in a hydrophobic formulation. The binder could act as a "holder" for the preferential active ingredient of the compound and would also act as a diluting agent thereby reducing costs. Their final list of criteria for testing of hydrophobic coatings was:

1.   There was not an appreciable improvement in ice adhesion reduction if an extremely hydrophobic material was selected (those with contact angles greater than 110°).

2.   Extremely hydrophobic materials may actually exhibit high adhesion due to excess hydrophilic sites.

3.   Materials containing Si-C bonds are probably not UV stable.

4.   A stable (i.e. taken at equilibrium conditions) contact angle of water on the hydrophobic material (indicating low solubility) is probably more important than a very high contact angle.

5.   A coating should be several hundred nanometers thick to block the dipole dispersion forces.

The field tests of three hydrophobic coatings on pavement surfaces showed that two of the materials had considerable promise for delaying icing or allowing easier removal of accumulated ice on a paved surface. Another benefit of these coatings was the low environmental impact when compared to sand/salt ice control

Jellinek et al. (1978) investigated the adhesion of ice on different formulations of block-copolymer coatings. This study seems to be the most fully developed and experimentally sound work found in this review. The adhesion of ice on these coatings was found to depend on the siloxane content and its block lengths, the glass temperature of the copolymer, and the hydrophobic properties of the film surfaces; i.e., the polysiloxane block was preferentially situated in the film surface. The copolymer was supplied by General Electric and was a class of poly(dimethysiloxane) bisphenol-A polycarbonate block copolymers. The results indicated that a block-copolymer with 65% weight of polysiloxane, a chain length of 20, and glass temperature of -66°C showed the lowest adhesive strength of all films tested. Some representative values are shown in Table 2.1.

Table 2.1 Adhesive strengths of ice on aluminum and concrete substrates.

Treatment	Aluminum	Concrete
Polymer + Toluene	0.16 kg/cm^2	0.57 kg/cm^2
Polymer + Toluene + 10% silicone oil	0.04 kg/cm^2	0.033 kg/cm^2
No treatment	5.56 kg/cm^2	7.56 kg/cm^2

These investigators used Attenuated Total Reflectance (ATR) measurements to determine if the siloxane blocks were in a preferential location in the surface of the polymer. The method allowed the determination of the location of chemical groups by

measuring the absorbance ratios for transmission and reflectance. They found that the polysiloxane groups were located closer to the surface of the polymer as a function of percentage weight siloxane. The chemical structure of the polymer (Figure 2.1) shows the preferential orientation of the methyl groups.
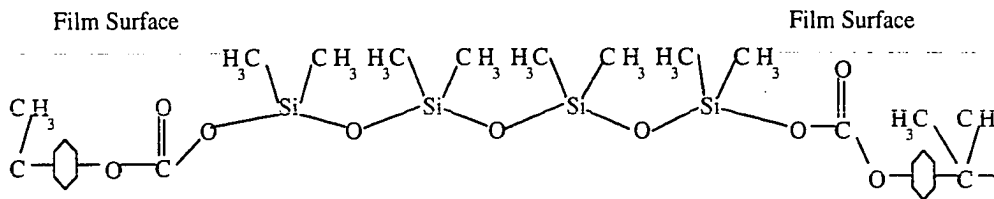
Figure 2.1. Ordering of supermolecular groups in poly(dimethysiloxane) bisphenol-A polycarbonate block copolymer (Jellinek et al., 1978).

The experiments and the range of the results presented showed that a good hydrophobic surface was not sufficient to lower ice adhesion strengths. It was postulated that if the weight content, glass temperature, and chain length were outside a given range, the properties of the coating become "similar" to those of ice and adhesion was increased. For the best results, it was suggested that the rheological and mechanical properties of ice and the coating should be as different as possible.

Other investigators (Mussalli et al. 1987 and Katoh et al. 1989) looked at the adhesion strength of ice on polyethylene substrates as a method of ice control. The Mussalli study concerned the use of a hydrophobic coating on water-intake trash racks to control frazil ice. They used the head loss as a function of time to determine the effectiveness of the coatings tested. It was found that with a combination of a polyamine epoxy coating and mechanical shaking it took one third as much time to rid a rack of ice as with an uncoated rack. Katoh was interested in the use of polyethylene coatings on steel and concrete pilings as used at sea. In addition to the icephobic nature of the coating (which they tested in terms of ice adhesion strengths), they investigated

the wear resistance of the coatings when ice was abraded against them. Though neither of these studies went into depth concerning the theory of ice adhesion, they demonstrated some of the applications for icephobic coatings. A commonality for all of the above studies was that they were concerned with the adhesive strength of ice to a surface. Studies on the adhesive strength of frost to different surfaces were not found in this survey.

Östin and Johannesson (1990) conducted experiments with an air-to-air heat exchanger utilizing hydrophilic and hydrophobic polymer coatings. The experiments were designed to test the frost growth prevention qualities of these coatings. They used three silicone based hydrophobic coatings and one hydrophilic polyurethane composition. The hydrophilic coating contained ethylene glycol to aid in the prevention of frost or ice growth. They found that there was no difference in frost growth thickness between the bare aluminum surface and an aluminum surface treated with one of the hydrophobic coatings. The hydrophilic coating performed very well for the first three or four frosting cycles. After that, the ethylene glycol chemical would begin to leach out of the base coating and this would effectively end the coating's ability to prevent the formation of frost on the surface of the heat exchanger. This low cycling ability severely restricted the use of these type coatings on heat exchanger surfaces. For both types of coatings, the test conditions were not typical of those for heat pump operations.

Very recently, researchers at The Dow Chemical Company (Schmidt et al. 1994), developed a water based hydrophobic coating. The new coating contained perfluoroalkyl groups which became oriented while curing to yield surfaces with very low surface energy. Contact angles for water on these surfaces was found to be as high as 115°. These class of polymers could be used for additional testing in ice and frost adhesion studies.

Condensation

Two basic modes for condensation of a saturated vapor onto a cooled surface have been identified in the literature: filmwise and dropwise. The dominant mechanism depends on whether the surface is easily wetted by the liquid (filmwise) or does not wet the surface, (dropwise). The bulk of the literature describing these mechanisms deal with steam condensing on a cooled surface. Some of the literature focuses on surfaces that has been treated to promote dropwise condensation.

The benefits for improved heat transfer during dropwise condensation have been investigated since Schmidt et al. (1930) first studied and reported on the process. Tanasawa (1978) reviewed the state of the art concerning dropwise condensation and summarized on microscopic mechanisms of condensation and heat transfer measurement. He describes a "life-cycle" of the condensation process. Initially, microscopic droplets form on a bare condensing surface. These droplets grow due to the continued transfer of mass from the vapor. At some point in their growth, they begin to touch and because of surface tension effects, they coalesce. As the droplets continue to grow and coalesce, nucleation of new droplet embryos occurs in the area cleared by the coalesced drops. This model has been verified experimentally (McCormick and Baer 1963 and Umur and Griffith 1965). Atomic level molecular dynamic simulations have also confirmed the macroscopic engineering view of this condensation process (Peters and Eggebrecht 1991).

If the condensation is allowed to proceed, droplets will grow to a limiting size commonly referred to as the departure size. At that point the balance between the surface tension (adhesion force) and external forces such as gravity or shear is upset and the drop moves off the surface. For the case of a surface held much below the

freezing temperature of the condensate, the droplets will nucleate to ice before the departure size is reached.

As with Tanasawa's description, Meakin (1992) describes the condensation process as occurring in four stages. In Stage I isolated droplet embryos grow from nucleation sites. During this stage, the characteristic dimension, R_d , of the droplets is much smaller than the characteristic dimension associated with the separation, R_s , between the drops. In Stage II, R_d grows to a size comparable to R_s and droplets begin to coalesce. In Stage III, renucleation occurs on the areas that are cleared by the coalescence of large droplets. Stage IV is the point when some droplets have reached a large enough size that they can move from the surface (if the surface is inclined). This growth cycle is exactly similar for the case of atmospheric water vapor condensing on a cooled surface. However, droplets usually do not depart from the surface because they nucleate to ice.

There is still some question as to the mechanism of initial droplet formation (Cary 1992b). One theory is that the vapor actually condenses in a film and at a critical thickness ruptures into droplets (Welch and Westwater 1961, Sugawara and Karusuta 1966). The other postulates that the droplets grow from active nucleation sites such as microscopic pits and scratches on a cooled surface. Recently, a study proposed a mixed mode of condensation termed droplets and film coexisting (Song et al. 1991). A commonality amongst the studies supporting film type condensation was that the surfaces used were all easily wetted by the vapor being condensed (most commonly steam). Surfaces that have a lower surface energy than water vapor do not wet as easily and these hydrophobic surfaces usually promote dropwise condensation (Holden et al. 1987, Marto et al. 1986). According to a recent study (Hautmann and Klein 1991) this hydrophobic action extended to the molecular level. Using molecular-dynamic

calculations, they showed that water molecules deposited on hydrophobic or hydrophilic surfaces exhibit qualitatively different wetting behavior. They were able to extend the often used macroscopic concept of the contact angle to the microscopic scale. These studies all have import on the proposed work for the following reasons: 1) preliminary tests conducted by the author have shown distinct dropwise condensation on the surfaces treated with a hydrophobic coating, 2) the mechanism of condensation on the bare metal surfaces was not clear (film versus dropwise), and 3) the early tests have shown little difference in heat transfer between the coated and uncoated surfaces. It would seem prudent to use results obtained from previous work and compare to the results from this investigation. Though direct comparison are not be possible, trends might be and these could prove helpful for subsequent studies. Song et al. (1991) showed experimentally that the two mechanisms coexisted for stainless steel and copper samples. Tanasawa (1978) maintained that it did not matter to the macroscopic heat transfer process which mechanism dominated. What mattered was the relationship between the drop size distribution and the heat transfer rate.

Drop Size Distribution

Many researchers have recognized the importance of the drop size distribution in condensation heat transfer. Following an analytical development from Carey (1992c), an expression for the heat transfer coefficient for a surface undergoing dropwise condensation of saturated vapor was given as

$$h_d = \left(\frac{\pi}{2}\right)\int_{D_{\min}}^{D_{\max}} N(D)D^2 \frac{(1 - D_{\min}/D)}{(1/h_i + D/4k_l)}dD \qquad 2.3$$

where h_d was the heat transfer coefficient, k_l the thermal conductivity of the liquid droplet, and D the droplet diameter. The droplet size distribution $N(D)$ must be known

over the range of droplet diameters if the heat transfer coefficient was to be determined. For steam condensing on a mirror-smooth copper surface, Graham and Griffith (1973) found that the distribution was proportional to $D^{-3.5}$ for droplet sizes between 10 and 1000 µm. Another steam condensation study measured condensate droplet size distributions for drops having a radius as small as one micron (Tanaka and Hatamiya 1986). Their data were generated using surfaces of mirrored finished chromium and diamond machined gold. They found a relation for the drop size distribution in terms of the radius of a droplet r and the maximum droplet radius R_{max}

$$\overline{N}(r) = 0.118\, R_{max}^{-3} \left(\frac{r}{R_{max}}\right)^{-2.7}$$ 2.4

The graphical representation for this equation is shown in Figure 2.2. There were restrictions (surface finish, steam pressures, vapor velocity, non-condensables present, etc.) on the use of this equation and it was not applicable to other geometries or surfaces.

There have been other distributions (Le Fevre and Rose 1964) that described the fraction of surface area, f, covered by droplets in the range of r to R_{max} as

$$f\left(\frac{r}{R_{max}}\right) = 1 - \left(\frac{r}{R_{max}}\right)^{\frac{1}{3}}$$ 2.5

Tanasawa (1978) stated that knowledge of the drop size distribution was required to determine the heat transferred to a surface due to dropwise condensation. He described a relationship between the fraction f of surface area covered by droplets and a drop size distribution $N(r)$ as

$$N(r) = -\frac{1}{ar^2} df\left(\frac{r}{R_{max}}\right)\frac{1}{dr}$$ 2.6
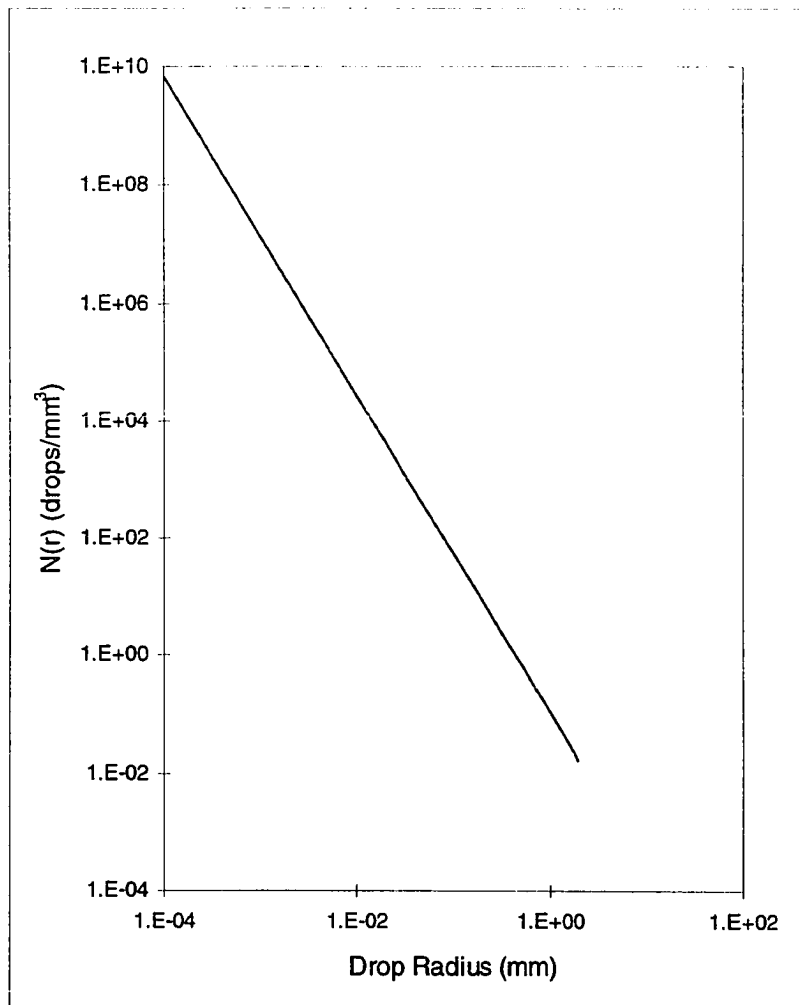
Figure 2.2. Droplet distribution from equation 2.4.

where r was the radius of a droplet at any instant, R_{max} was the droplet size just prior to departure from the surface and a was a ratio of area covered by the drop to the square of the radius. This distribution included droplets with contact angles other than 90°. Rose and Glicksman (1973) developed a model based on successive generations of geometrical droplet growth for the droplet distribution and suggested the following equation:

$$N(r)\mathrm{d}r = \frac{f}{\pi R_{\max}}\left[1+2\sum_{i=1}^{m}\left\{\frac{(1-f)^i}{\gamma^i}\left(1-\frac{1}{\gamma^i}\frac{r}{R_{\max}}\right)\right\}\right]\frac{\mathrm{d}r}{r^2}\qquad\qquad 2.7$$

In this equation, f was the area between the larger drops of previous generations, γ the

ratio of maximum radius of any generation to its immediate predecessor, and R_{max} the

maximum radius of the current generation. From earlier work done by Le Fevre and

Rose (1966), they also showed that the drop size distribution could accurately be

represented by

$$N(r)\mathrm{d}r = \frac{1}{3\pi\, r^2 R_{\max}}\left[\frac{r}{R_{\max}}\right]^{-\frac{2}{3}}\mathrm{d}r\qquad\qquad 2.8$$

This equation was applicable for a steam condensing system with approximately 55%

of the surface area covered by droplets. Their modeling efforts of the drop size

distribution agreed within the scatter of measurements for steam condensing systems.

Figure 2.3 shows curves for three different droplet site densities. Though not explicitly

shown in this figure, the curves for their theoretical work, Le Fevre and Rose's work,

and experimental data from Glicksman and Hunt (1972) all converge at radii greater

than approximately 10 microns. Significantly, they pointed out that their model was

based entirely on geometric considerations. For their work, this conclusion was

applicable only to measurements on drop diameters greater than 10 μm and contact

angles of less than or equal to 90 degrees. Their theory did not include temperature,

pressure, or any fluid property and they suggested *that the coupling between drop size*

distribution and heat transfer parameters was weak.
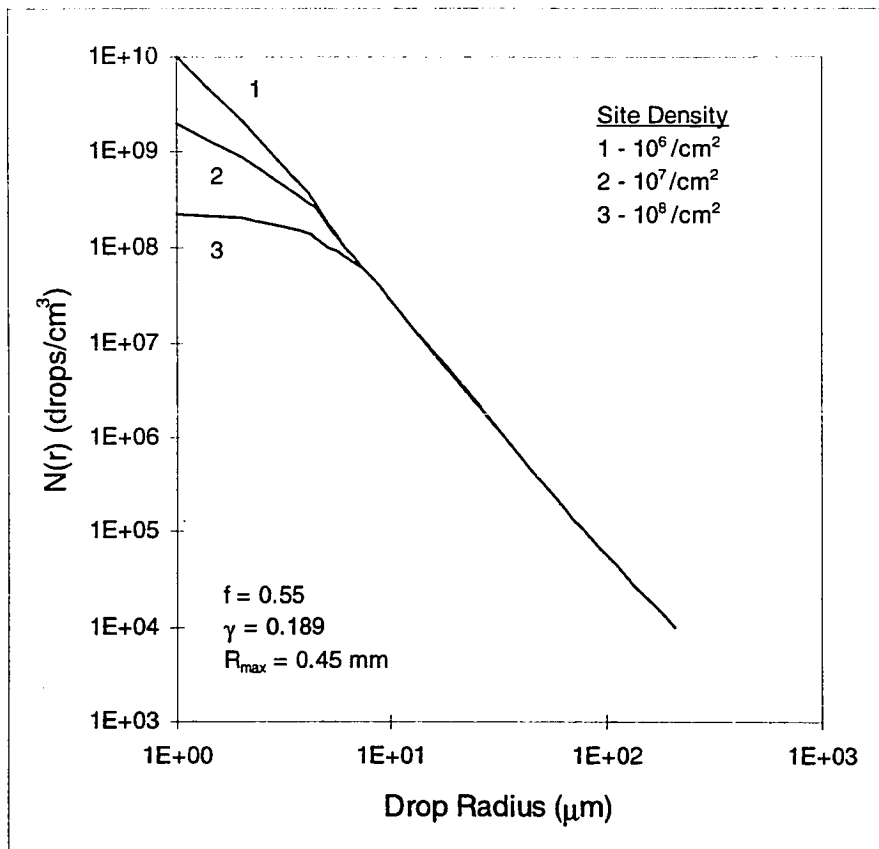
Figure 2.3. Theoretical drop density curves from equation 2.7 (Rose and Glicksman, 1973).

By considering basic heat transfer and thermodynamic mechanisms, Glicksman and Hunt (1972) determined drop size distributions for a steam condensing system. They utilized a numerical simulation to model the dropwise condensation process. To make the simulation manageable, they broke the condensation process into 6 stages with each stage representing a finite range of droplet radii. They evaluated the average behavior of primary drops by using the results of the first stage. The simulation continued by using stages with successively larger areas. They did not present the results of their drop size distribution explicitly in their paper, but did present graphical

results. Their model distribution agreed very well with the distribution proposed by Rose and Glicksman (equation 2.6). Figure 2.4 shows the results of their numerical simulations for steam condensation and different initial site densities. The simulation results for the early stages of condensation showed that the nucleation site density was an important variable and should be included in any experimental correlation. They reported nucleation site densities of 10^7 to 10^8 sites per cm^2. For their experimental verification of site density, they counted just visible drops on a condensing surface under high magnification.
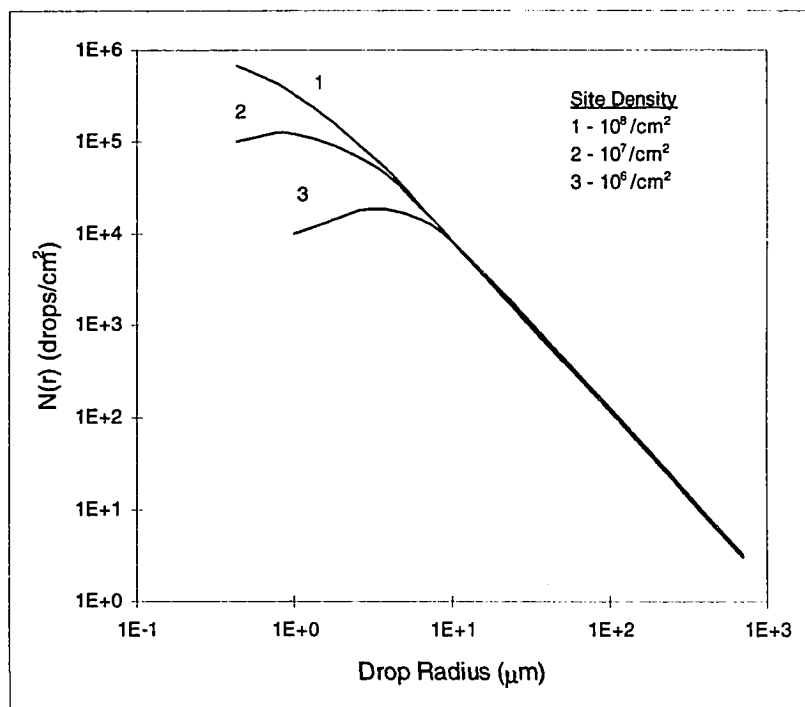
Figure 2.4. Average distribution of drop sizes with steam saturation temperature of 100°C (Rose and Glicksman, 1973)

This technique limited them to droplets of one micron radius or larger and was a result of the limitations of light microscopy. Their calculations showed that for condensing

steam and temperature differences of greater than one-half degree Fahrenheit, the minimum droplet radius would be less than one-tenth of a micron. These researchers found that a "universal distribution" of drop sizes holds for droplets of 20 microns radius or larger. This also agrees with findings by Tanaka (1975a). They also found that the drop size prediction for a single stage of their simulation agreed with steady state experimental data. This indicated that the model results could be used as a stand-alone module to predict long-term droplet growth. One limitation for this model was that all droplets were assumed to be hemispheres (contact angle = 90°). Also, the size of the droplet embryo was considered to be a constant for a given saturation temperature and vapor to condensing surface temperature difference.

Tanaka (1975a) described the dropwise condensation process as a transient phenomenon occurring repeatedly at random sites on a condensing surface. He modeled the process through statistical and geometrical considerations and solved the resulting equations to predict a universal drop-size distribution. He predicted two distributions; the universal distribution for large drop sizes and a steady distribution for microscopic drop sizes. Figure 2.5 shows the theoretical curve describing the drop size distribution for the large drop sizes. The hump at four micron radius was a result of two droplets coalescing.
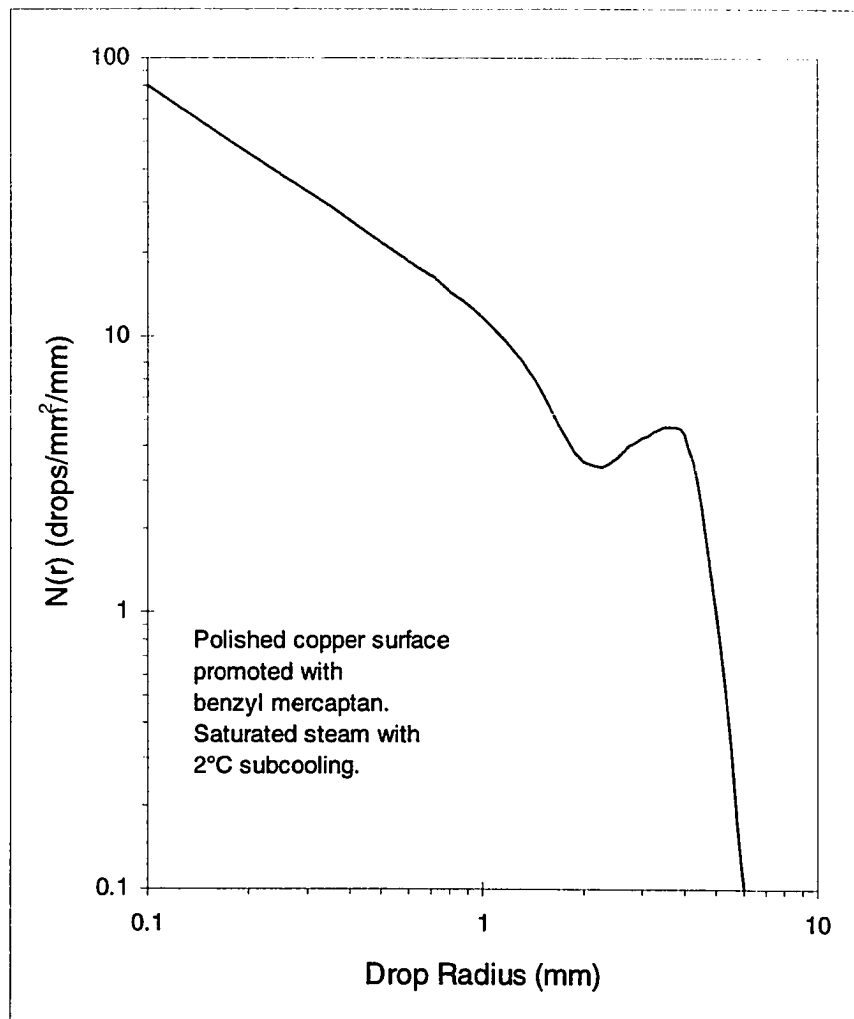
Figure 2.5. Theoretical Curve for large drop sizes (Tanaka, 1975a).

Tanaka (1975b) conducted experiments with condensing steam to verify his theory for dropwise condensation and drop size distribution. As he predicted, a "universal" drop size distribution for large drops (radii greater than 0.1 mm) was established. He also found an equilibrium region for small drops where the instantaneous distribution N was proportional to $r^{-2.7}$. This was in agreement with Rose and Glicksman (1973) who showed that the distribution N was proportional to $r^{-3.3}$.

Early Stage Heat and Mass Transfer

The early stage of the frost growth phenomena consists of the nucleation of liquid water droplets onto a cold surface, continued droplet growth due to heat and mass transfer mechanisms, and ultimately, the phase-change of the droplet into an ice embryo. This is an enormously complex process and researchers gained insight only through convenient assumptions and simplifications of the problem. The heat and mass transfer problem can be broken into the following topics, most of which are dependent upon each other; 1) mass diffusion to and from the droplet, 2) heat transfer through the droplet, 3) droplet radial growth, 4) effect of non-condensables on the process, and 5) the role of the condensation coefficient. Each of theses topics will be discussed with the emphasis being relevance to the current study.

The most common fluid studied in the literature is steam. This substance has very attractive qualities in terms of control for experimental purposes as well as being important to many industrial processes. Though not studied to the extent that steam systems are, water vapor and air systems are also very common. The air conditioning process is a widely studied air/water vapor system. The analysis of the condensation process for air/water vapor and steam systems is markedly different. Steam research has focused on basic mechanisms and methods to increase the amount of heat transferred for a given process. Much of this work has concentrated on the nucleation mechanics and early, microscopic stages of steam condensation. The air conditioning industry treats the condensation of water vapor as a secondary product of the cooling effect of the equipment. Conversely, the study of the frosting process has caused researchers to delve further and further into the microscopic stages of the frosting phenomena. Prior to the present study however, no one has investigated the early stages of water condensation leading to the nucleation of ice embryos. For this reason

there is a dearth of information directly applicable to this problem. It was felt that work that had been done in steam or atmospheric research could be applied directly to the current problem. Following is a review of the applicable steam and atmospheric research literature with reasons why this is not so.

Interfacial Heat Transfer

The most common "thread" found in the course of the steam literature review was the work published by Umur and Griffith (1965). These researchers developed the following form of Schrage's (1953) equation for the net rate of condensation per unit interfacial area

$$w = \left(\frac{2\alpha}{2-\alpha}\right)\left(\frac{g}{2\pi\overline{R}}\right)^{\frac{1}{2}}\left[\frac{P_v}{T_v^{0.5}} - \frac{P_i^{**}}{T_i^{0.5}}\right] \qquad 2.9$$

Using the Kelvin-Helmholtz relationship

$$\ln\frac{P_r^{**}}{P^*} = \frac{2\sigma v_l}{r\overline{R}T} \qquad 2.10$$

and assuming that the vapor was saturated (a critical simplification) and using the Clausius-Clapeyron relation yielded the following expression for the condensation rate

$$w = \left(\frac{2\alpha}{2-\alpha}\right)\left(\frac{g}{2\pi}\right)^{1/2}\frac{i_{fg}P_v^*}{R_g^{3/2}T_v^{5/2}}\left(1-\frac{r^*}{r}\right)(T_v - T_i) \qquad 2.11$$

This equation required that the interface temperature T_i be known before w could be evaluated. Acknowledging that the ratio of the interface and bulk vapor temperatures was rarely less than one, Umur and Griffith put forth the following equation for an "interfacial heat transfer coefficient"

$$h_i = \left(\frac{2\alpha}{2-\alpha}\right)\left(\frac{g}{2\pi}\right)^{1/2}\frac{i_{fg}^2 P_v^*}{R_g^{3/2}T_v^{5/2}}\left(1-\frac{r^*}{r}\right) \qquad 2.12$$

This important result has been heavily referenced since its introduction. It was essentially a mass transfer coefficient defined at the droplet/vapor interface and is prominent in subsequent droplet growth and heat transfer relationships. Neglecting sensible heat transfer, assuming hemispherical drops, and that heat transfer through the droplet was due to conduction alone, they developed the following steady state expression for the heat transferred through a droplet

$$q_d = 2\pi r k_l (T_v - T_s)\sum_{\substack{m=1\\odd}}^{\infty}\frac{m(2m+1)}{1+\frac{k_l}{h_i r}m}\left[\int_0^\infty P_m(x)dx\right] \qquad 2.13$$

Using this result and the volume of a hemispherical droplet then differentiating with respect to time yielded an equation for the droplet growth rate

$$\frac{dr}{dt} = \frac{k_l(T_v - T_s)}{\rho_l i_{fg} r}\sum_{\substack{m=1\\odd}}^{\infty}\frac{m(2m+1)}{1+\frac{k_l}{h_i r}m}\left[\int_0^1 P_m(x)dx\right]^2 \qquad 2.14$$

The critical quantity in the previous two equations was the temperature difference $(T_v - T_w)$. Though defined as the temperature difference between the vapor and surface, this quantity presents some difficulty and will be commented upon later in this section. Umur and Griffith compared their analytical solutions to one previous experimental result and were able to show good agreement. Additionally, they showed that pressure had a marked affect on the drop growth rate.

McCormick and Westwater (1966) presented results of their experimental work with dropwise condensation and compared their results to some previous analytical work. They concluded that the determination of the heat flux for a given application

could not be described with a simple analytical model, because the calculation involved the nucleation, growth, and coalescence of every droplet on a surface. They developed the following empirical equation for G, the droplet growth rate, as

$$G = \left(\frac{D^2}{t}\right)\left(\frac{T_s}{0.79 + \Delta T}\right)\left(\frac{\rho_l}{\rho_v}\right)$$

2.15

In this equation, ΔT was in degrees Fahrenheit and described the temperature difference through the "thermal boundary layer". They acknowledged that none of the theories at that time correctly predicted the experimentally observed droplet growth rates. They also found that changes in neighboring droplets (i.e. coalescence and growth) had an effect on the drop growth rate. They also referenced equation 2.14 in their work and noted that in order for this equation to match their experimental drop growth rate, it was necessary to use a ΔT that was approximately one fifth of the experimental ΔT. For example, one of their runs was at a ΔT of 1.31° F and equation 2.14 required a ΔT of 0.27° F. The first of many confusing statements in the literature concerning equation 2.14 also appeared in their paper. They described the temperature difference (T_v - T_w) from equation 2.14 as the difference between the temperature at the base of the droplet and the bulk vapor temperature. Ostensibly, this was the same equation defined by Umur and Griffith who defined this temperature difference as the bulk vapor temperature minus the surface temperature. In any event, the differing interpretations have a dramatic affect on the resulting droplet growth rate.

Mikic (1968) simplified equation 2.13 and the result is given in equation 2.16.

$$q_d = \frac{4\pi\left(rk_l\left(T_v - T_c\right)\right)}{1 + \left(\frac{2k_l}{h_i r}\right)}$$

2.16

Though very similar to equation 2.13, Mikic defined the temperature difference in terms of T_v as the vapor temperature and T_c as the surface temperature under an "active" droplet. Again, this choice for the temperature difference was not quite the same as the original definition as put forth by Umur and Griffith. The main thrust of Mikic's work was the development of the concept of constriction resistance and its impact on heat transfer in dropwise condensation. He postulated that as a droplet grew it became less effective at conducting heat. This led to droplets becoming larger, with larger resistances to heat transfer on the surface, and to the idea of active versus inactive droplets.

Glicksman and Hunt (1972) assumed that the total temperature drop from the vapor to the condensing surface was the sum of the temperature differences due to curvature, interfacial mass transfer, and conduction which was given by

$$\Delta Tt = \Delta Tc + \Delta Ti + \Delta Tcd \qquad\qquad 2.17$$

respectively, with

$$\Delta Tc = \frac{2T_s \sigma}{i_{fg} \rho\, r}\,, \qquad \Delta Ti = \frac{\sigma}{h_i 2\pi r^2}\,, \text{ and} \qquad \Delta Tcd = \frac{QS}{k\pi r} \qquad 2.18a, b, c$$

In equation 2.18b, the interfacial heat transfer coefficient h_i could be evaluated from Schrage (1953)

$$h_i = \left(\frac{2\alpha}{2-\alpha}\right)\left(\frac{M}{2\pi \overline{R} T_s}\right)^{.5} \frac{i_{fg}^2}{T_s v_g} \qquad\qquad 2.19$$

where the condensation coefficient α was assumed to be unity. In this equation, they defined T_s to be the saturation temperature for the vapor. They also gave the following equation for the heat transferred through a droplet as

$$Q_d = \frac{\left(T_s - T_w\right) - \dfrac{2T_s\sigma}{i_{fg}\rho\, r}}{\dfrac{1}{h_i\, 2\pi r^2} + \dfrac{1}{4k_l\pi r}}$$

2.20

This equation was a simplified version of 2.13 with yet again unique temperature differences defined. In this equation T_s was the saturation temperature and T_w was the solid surface temperature. This equation, as with all other simplifications of 2.13, are developed with the assumption that the drops are hemispherical, there are no noncondensables, and the process was steady-state.

The interfacial heat transfer coefficient as developed by Umur and Griffith (1966) also has had a rather rough time in the literature. Equation 2.12 is the original form as published. A different form (Tanaka 1986) of this equation was given in the literature as

$$h_i = \left(\frac{2\alpha}{2 - \alpha}\right)\left(\frac{1}{2\pi R_g T_s}\right)^{1/2} \frac{i_{fg}^{\,2}}{T_s v_g}$$

2.21

As given in this equation, T_s was the saturation temperature of the vapor. It seems that the temperature at which the coefficient should be evaluated shifted according to whomever was referencing it. For example, Maa (1983) gave the interfacial heat transfer coefficient as

$$h_i = \left(\frac{2\alpha}{2 - \alpha}\right)\left(\frac{1}{2\pi R_g \overline{T}}\right)^{1/2} \frac{i_{fg}^{\,2}}{T_s v_g}$$

2.22

Though almost identical to equation 2.21, Maa defined $\overline{T}$ as the average droplet surface temperature. For a saturated vapor, this temperature should be very close to the bulk vapor temperature. Cary's (1992) version of this parameter was given by

$$h_i = \left(\frac{2\alpha}{2-\alpha}\right)\left(\frac{1}{2\pi R_g T_v}\right)^{1/2} \frac{i_{fg}^2}{T_v v_g} \qquad 2.23$$

In this equation Cary used T_v, the temperature of the bulk vapor. The point to be made here was that there seemed to be a wide variety of choices for temperature references and temperature differences when using equations 2.21 to 2.23. The choice for reference temperature in the interfacial heat transfer coefficient is not as critical as is the choice for the temperature differences in equations such as 2.13 and 2.14. This is the driving potential in these equations and even a cursory uncertainty analysis would reveal the importance of the quantity.

Condensation Coefficient

Another modifier in the above equations and one that is still the subject of much research was the condensation coefficient, α. This factor was introduced through kinetic gas theory as a means of quantifying that not all vapor molecules that strike a condensing phase enter that phase. Some are reflected (evaporate) and some condense. This factor was experimentally determined for many condensing vapor systems, but by far the most common substance was in the water vapor system. Values for the condensation coefficient were reported in the literature as low as 0.006 and frequently was assumed to be unity (Mills and Seban 1967). This wide range of values seems to indicate that no one value exists as a general descriptor for the condensation coefficient for water vapor.

More recently Tanaka and Hatamiya (1986), reported a value of approximately 0.45 for a pure steam vapor system. These researchers found that even trace amounts of noncondensable gas (contaminants) greatly reduced the value for the condensation coefficient.

Researchers studying cloud physics and modeling cloud droplet nucleation, growth and precipitation have been more consistent on the value for the condensation coefficient. Values in their literature span from approximately 0.003 to 0.4. The effect of noncondensable gas (air) was evident in the consistently low value for the condensation coefficient. Even in this field of research though, the evaluation of this coefficient was not static. Okuyama and Zung (1967), showed that α was related to the Gibbs free energy associated with condensation and the free-angle ratio δ by

$$\alpha(r) = \delta \exp\left[-2\pi r^2 \sigma / R_v T\right] \qquad 2.24$$

The free-angle ratio was the ratio of the rotational partition functions of a molecule in the bulk liquid phase and in the gas phase. This ratio had values of 0.04 or 1.0 in the literature (Chen 1974). The range of the free-angle ratio can affect the value of the condensation coefficient by an order of magnitude. Equation 2.24 shows that, assuming δ is unity, the condensation coefficient is near unity for droplets near the critical radius and decreases rapidly as the droplet continues to grow. This model for the condensation coefficient matches very well with what physically happens during the very early stages of vapor condensation. Indeed, physicists studying condensation patterns (Viovy et al. 1988) described the early condensation (t < 1s) as "a furious and complex activity" with subsequent time decades consisting of continuous smooth growth from the supersaturated vapor.

If the free-angle ratio was chosen as 0.04, the condensation coefficient started at a value of approximately 0.04 which agreed well with the range of values quoted in the cloud physics literature of 0.03 - 0.04. A recent experimental determination for the condensation coefficient (Hagen et al. 1989) showed a value of unity at the onset of nucleation and decreased to a value of approximately 0.01. Two primary sources of

error in the evaluation of the condensation coefficient were identified in the literature; 1) uncertainty in the measurement of surface temperature, and 2) the effect of contaminants such as noncondensable gas. These sources of error created a wide range of values for the condensation coefficient from both steam and atmospheric sciences. For the present study, the coefficient as described by Okuyama and Zung with δ equal to 1.0 was used.

Non-Condensables

The effect of non-condensables on the condensation of saturated steam has been studied by numerous investigators. In fact, for studies involving steam as the condensing vapor, elaborate precautions were taken to eliminate non-condensables from the vapor stream. The presence of very minute amounts of non-condensable gas influences the heat transfer resistance at the liquid-vapor interface (Collier 1972). The non-condensable gas accumulates at the interface as it is carried by the condensing vapor. The partial pressure of the accumulating gas increases above that in the bulk vapor which generates a potential for gas diffusion away from the interface. The buildup also causes a reduction in the partial pressure of the vapor at the interface. This, in turn, reduces the saturation temperature at which condensation takes place. The end effect is to lower the driving thermal potential $(T_i - T_w)$ which reduces heat transfer. The effect of non-condensable gas on the overall heat transfer rate for a steam condensing system is shown in Figure 2.6. Here, the heat transfer ratio is defined as the ratio of the heat transfer rate with noncondensable air present to that which would have occurred with a pure vapor (Collier 1972). Collier's analytical result demonstrated the dramatic effect of even a small amount of non-condensable gas on the heat transfer occurring in the steam condensation process.
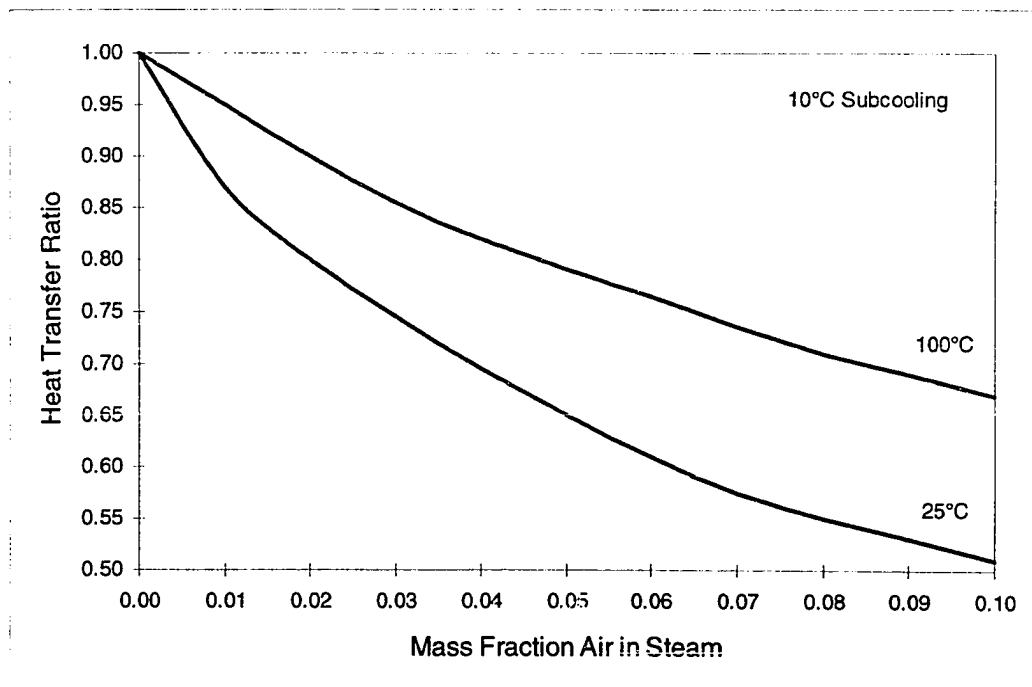
Figure 2.6. Effect of non-condensable gas on heat transfer for condensing steam (Collier, 1972).

Minkowycz and Sparrow (1966) showed that the condensation coefficient played an important role in steam condensation only at low values of α ($\alpha < 0.04$). Through their analytical work on the effect of non-condensables on film-wise condensation they contended that for steam condensation, interfacial resistance had a negligible role and could be neglected. Sparrow et al. (1967) presented additional analytical work showing again that only at very low α did the interfacial resistance become non-negligible.

The atmospheric scientists deal with the non-condensable problem in a different manner. As opposed to the steam problem (low mass fraction of air) the atmospheric droplet growth is faced with the reverse problem, low mass fraction of water vapor. Additionally, the heat of condensation in the droplet is conducted away from the droplet and back into the surroundings. For steam systems, the heat of condensation is

conducted through the droplet and into the cold substrate. In the atmospheric literature, the mass of water vapor diffused per unit time and the amount of heat conducted away per unit time are given by the following Maxwell relationships respectively (Fukuta and Walter 1970)

$$\frac{dm}{dt} = 4\pi r \overline{D}(\rho_\infty - \rho_s) \qquad \frac{dQ}{dt} = 4\pi r k_\infty (T_s - T_\infty) \qquad \text{2.25a, b}$$

The amount of heat released by condensation has to be dissipated by conduction from the droplet, so equating the above equations, and using the Clausius-Clapyron equation, they derived the following equation for change of droplet mass per unit time

$$\frac{dm}{dt} = \frac{4\pi r(S-1)}{\left(\dfrac{i_{fg}^2 M}{k_\infty \overline{RT_\infty^2}} + \dfrac{\overline{R}T_\infty}{D \ Mp_{\infty,s}}\right)} \qquad \text{2.26}$$

This theory for drop growth did not account for the increase in resistance at the liquid-vapor interface due to non-condensables. These authors (Fukuta and Walter) included the resistance of the non-condensable gas (air) on the drop growth process through the introduction of proportionality factors. These correction factors were functions of the condensation and accommodation coefficients and they modified equations 2.25a and b, which yielded the following equations,

$$\frac{dm}{dt} = 4\pi r D \ f_\alpha (\rho_\infty - \rho_s) \qquad \frac{dQ}{dt} = 4\pi r k_\infty \ f_\beta (T_s - T_\infty) \qquad \text{2.27a, b}$$

where,

$$f_\alpha = \frac{r}{r + \left[\left(\dfrac{2\pi}{\overline{R_g T_\infty}}\right)^{0.5} + \left(\dfrac{D}{\alpha}\right)\right]} \qquad f_\beta = \frac{r}{r + \left[\dfrac{k_\infty \sqrt{2\pi M_a \overline{RT_\infty}}}{\beta p_\infty \left(C_v + \overline{R}/2\right)}\right]} \qquad \text{2.28}$$

The factor, f_β, could be taken as equal to unity with negligible error when considering droplet growth under conditions normally found in terrestrial cloud formations.

Though approached differently, both fields of study acknowledged that there was an effect due to the presence of non-condensable gases on droplet growth and heat transfer.

Critical Droplet Radius

Equations for the thermodynamic critical radius for dropwise condensation were given in every one of the studies reviewed for the present work. The critical radius was defined as a droplet that is thermodynamically viable. For droplets smaller than r^*, the droplet would spontaneously evaporate, while droplets that were larger than r^* would continue to grow. Though all of the equations are very similar, the differences can be significant.

McCormick and Westwater (1965) developed the following equation for the critical droplet radius

$$r^* = \frac{2\sigma T_s}{i_{fg}\,\rho_l\,(T_s - T_d)} \qquad\qquad 2.29$$

The temperature difference used in this equation was between the saturation temperature and the temperature at the top of the droplet. Graham and Griffith (1973) gave the following equation for the critical droplet size

$$r^* = \frac{2\sigma T_s}{i_{fg}\,\rho_l\,(T_v - T_w)} \qquad\qquad 2.30$$

In this equation, the temperature difference was between the bulk vapor temperature and the wall temperature. Maa (1983) gave the droplet size as

$$r^* = \frac{2\sigma\overline{T}}{i_{fg}\,\rho_l\left(T_s - T_w\right)}$$
\hfill 2.31

Here the temperature difference was defined as the saturation temperature minus the wall temperature and $\overline{T}$ is the average droplet surface temperature. Cary (1992) gave the critical droplet radius as

$$r^* = \frac{2\sigma T_w}{i_{fg}\,\rho_l\left(T_s - T_w\right)}$$
\hfill 2.32

Cary used the saturation temperature minus the wall temperature for the temperature difference and the wall temperature in the numerator. In the above equations, the values obtained for the critical droplet size were all of the same order of magnitude and approximately equal. Equations 2.30, 31, and 32 resulted in approximately equal values for the critical radius when evaluated at similar conditions. Equation 2.29 yielded an r* that was larger by a factor of about two. Equation 2.32 is probably the best choice to use when evaluating the critical radius. The quantities required for the equation are readily available with no uncertainty about the temperature definitions. In contrast, equations such as 2.31 and 2.29 require an estimate such as the average droplet surface temperature, which would be very difficult to measure or verify. The researcher citing these equations must be cognizant of the differences and definitions used to develop the forms given.

Tanaka (1975a) developed a simple model for the heat transfer coefficient under steady dropwise condensation given by

$$\overline{h} = \frac{5.3k}{R_{max}}\left(\frac{R_{max}}{D}\right)^{0.7}$$
\hfill 2.33

where R_{max} was the maximum droplet radius on the condensing surface just prior to departure, D was the average distance between nucleation sites, and k was the thermal conductivity of the liquid. This relationship was developed for steam condensing systems only. A comparison to atmospheric condensation yielded heat transfer coefficients that were two orders of magnitude too large compared to experimental values (Tao and Besant 1993). Tanaka's model considered only droplets that were hemispherical (90° contact angle) which was a common assumption by many investigators in the literature.

Frost Models

Tao et al. (1993) described experimental work to quantify what they termed as the early stage of frost growth. This period covered the initial nucleation of liquid water embryos on a cold surface, the growth of the droplets through additional condensation, and coalescence with other droplets until the droplet had supercooled to the point that it could nucleate into an ice droplet. They deemed this period as the first stage of frost growth. The time of ice nucleation was defined in their work as transition time one $(t_{tr,1})$. Images were evaluated at the transition of the water droplets to ice and the average particle radius, R, and a surface area fraction of droplets, ε, were determined from

$$R = \sqrt{\sum_{i=1}^{N} \frac{A_i}{(\pi N)}} \qquad\qquad 2.34$$

and

$$\varepsilon_A = \frac{A_i}{A_t} = \pi \frac{R^2}{l^2} \qquad\qquad 2.35$$

where A_i was the contact surface area of the ith droplet, A_t was the total area of the image and l was a characteristic length of the droplet. Their experimental work was conducted with a constant ambient temperature of 20° C, Reynolds numbers of 2500 - 5000, and cold plate temperatures of -20 to -5° C. These conditions were not typical of those found in heat pump systems and as such, the results of their work may not extend to these systems. They modeled the frost growth process from the first transition point, $t_{tr,1}$, forward in time. Tao developed a model for frost growth from this point called the unit cell method. This model depended upon a distribution of frozen water droplet sizes on a cold surface as the origin of the subsequent frost matrix. Because there was no experimental or analytical data on what this distribution looked like, they assumed a distribution for their frost growth model.

Summary

A review of the available literature that addressed the initial stages of water droplet growth and coalescence on a cold surface has been completed. Additionally, references on the effect of hydrophobic coatings as applied to cold surfaces on the resulting dropsize distributions were consulted. The following conclusions were drawn as a result of this review:

1. Drop size distributions have been modeled and experimentally confirmed for many steam condensing systems/configurations. No references were found for atmospheric vapor condensing on a cold surface and the resulting drop size distribution under icing conditions.

2. The bulk of hydrophobic coatings work has been concerned with the reduction of the adhesion strength of ice to a substrate. No references were found regarding

the ability of a hydrophobic surface to delay or prevent the onset of ice or frost growth on a cold surface.

3. Several studies have been done on the effectiveness of hydrophobic coatings on the promotion of dropwise condensation for steam condensing systems. No references were found for the analogous situation when condensing atmospheric vapor onto a cold surface.

4. The associated heat transfer information for steam condensing systems is also well documented. Again, no references were found for atmospheric vapor condensing systems. The correlations for heat transfer properties do not extend to these type condensing systems.

5. The single study concerning this early stage of condensation and ice growth was performed under much different conditions than those found in typical heat pump applications.

6. Existing models for the drop size distributions all assume a hemispherical drop and do not allow for the higher contact angles resulting from the application of a hydrophobic coating to the cold surface.

7. Early stage droplet growth work has been concentrated on steam or atmospheric cloud systems. Models for either of these systems are not directly applicable to the condensation of water vapor onto a cold solid surface.

The foregoing items have provided the impetus for the current work. The succeeding chapters will detail the modeling, experimental work, and discussion of the results of this investigation.

CHAPTER III

EXPERIMENTAL SETUP AND PROCEDURES

To study the early stages of water vapor condensation and freezing, a benchtop apparatus was constructed at the Texas A&M University Energy Systems Laboratory. This benchtop psychrometric facility permitted control of the air temperature, flow, and moisture content entering a test section containing the cold surface. The entire system consisted of insulated ductwork, primary and secondary cooling heat exchangers, a reheat section, humidifying section, a dual inlet blower, and a clear test section (Figure 3.1). After exiting the blower, the air was cooled and dehumidified at the primary cooling heat exchanger. A secondary heat exchanger provided additional cooling and dehumidification if required. The air then entered the reheat section which provided final control of the air psychrometric conditions before entering the test section. Saturated steam at atmospheric pressure was added after the primary heat exchanger if additional moisture was needed in the air stream. The system was able to control air conditions in the temperature range of -5° C to 50° C (± 0.5°C) and 30 to 90% (± 3% RH) relative humidity. Typical instrumentation (thermocouples, heat flux gage, etc.) was used to measure various extensive properties during a test and will be further described in detail. A video microscopy system coupled to a digital image capture system provided microscopic imaging and analysis of the droplets during the condensation and freezing process. This was a closed loop facility and because of its small size, relative to full sized psychrometric facilities, steady state conditions were reached in a very short time (typically 15 minutes after a step change in setpoints).

The closed loop was comprised of five basic elements;

1.   Cooling Section

2.　Humidification Section

3　Reheat Section

4.　Test Section

5.　Instrumentation

Each of these elements is described more fully below.

Cooling Section

　　Figure 3.1 shows a schematic of the test loop which was constructed to provide controlled conditions during the condensation studies. The ductwork was constructed of 12.7 mm thick insulating board with a rectangular cross-sectional area of 0.013 m^2 and converging and diverging sections as needed at the heat exchangers and blower. All duct seams were joined with hot-melt glue and then taped with metalized tape to minimize air infiltration.
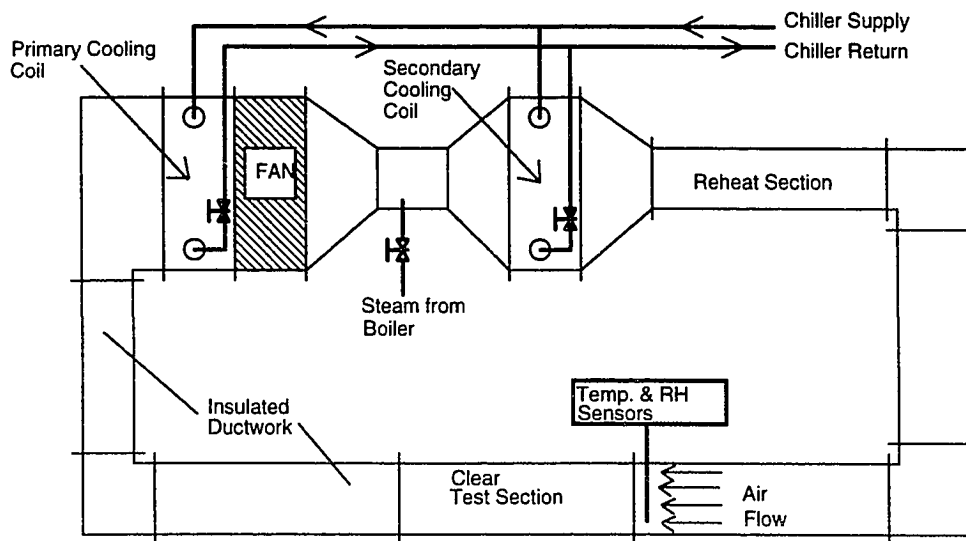
Figure 3.1. Schematic of closed-loop test apparatus.

Turning vanes were constructed and installed to reduce turbulence in the 90° elbows. A dual inlet, 120 Volt centrifugal blower provided air flow for the test loop. The fan could provide velocities in the range of 0.5 to 2.5 m/s which allowed Reynold's numbers in the range of 200 to 9000 at the test section. These values of Re were calculated for external flow over a flat plate and are well within the laminar flow regime. Air velocities were controlled at the test section through the use of multi-hole orifices and a slide damper installed at the bypass section. Early tests had shown that at low air velocities, heat transfer through the cooling heat exchangers was inadequate to maintain control of air temperatures. The bypass section was added parallel to the test section so that adequate velocities could be maintained across the cooling heat exchangers even at very low velocities in the test section. Closing the bypass damper forced more air flow through the test section and test section annulus. The primary heat exchanger was an automotive air-conditioning system evaporator and had a face area of approximately 0.06 m², 4 rows, and 700 fins per meter (fpm). The secondary heat exchanger was constructed from a drinking fountain condensing coil and had a face area of approximately 0.05 m², 2 rows, and 680 fpm.

A chiller supplied glycol-water solution to the primary cooling heat exchanger and to the secondary cooling/dehumidification heat exchanger. The chiller was capable of supplying solution temperatures as low as -15°C. At normal ambient operating temperatures, the complete cooling system was able to maintain a 10°C approach between supply chilled solution temperature and circulating loop air temperature.

Humidification System

Humidity control was achieved by using a combination of the cooling coils, reheater, and moisture addition as required. Depending on ambient conditions, nominal

relative humidities of 50 - 55% were quite readily maintained. If higher humidity was required, saturated steam at just over atmospheric pressure was injected after the primary cooling coil. The steam was supplied from a boiler constructed from a recycled hot chocolate maker. The steam "injector nozzle" consisted of a small gate valve and a 9 mm diameter copper tube with a number of 1.5 mm holes. The steam flow was controlled via the gate valve and by adjusting the amount of current drawn by the boiler's immersion heater element. With this system, relative humidity in the closed duct system could be controlled ($\pm$ 3% RH) up to a level of 90%.

Reheat Section

A 500 Watt resistance heater located downstream from the secondary cooling heat exchanger was used as the final control element. The heater was regulated by a Red Lion Model TCU solid state controller. Feedback to the controller was from an averaging thermocouple grid (Type T, copper-constantan) located before the test section. This arrangement allowed air conditions to be controlled and varied over a range of -5° C to 35° C ($\pm$ 0.5° C).

Test Section

An isometric schematic of the clear 15mm x 60mm Plexiglas® test section (900 mm^2 cross section area, $\pm$ 4 mm^2) is shown in Figure 3.2. The test section was constructed to allow non-invasive viewing of the metal specimen during the condensation process.
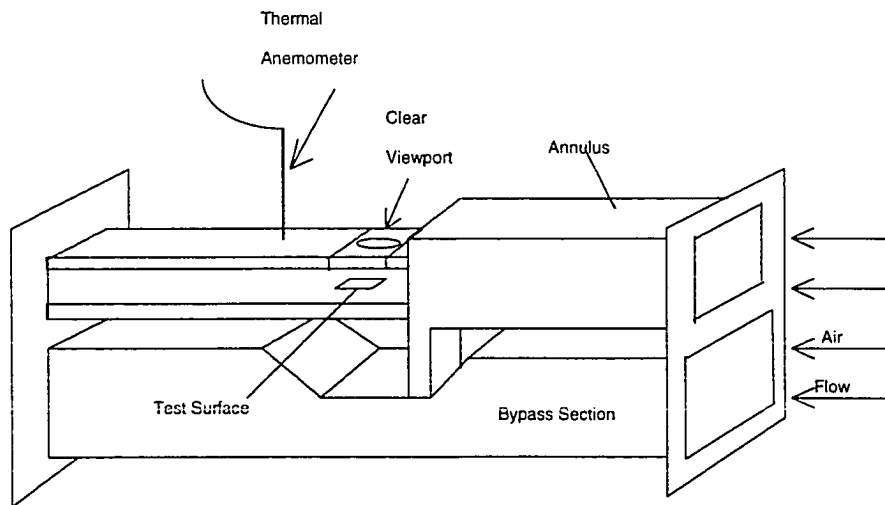
Figure 3.2. Isometric of test section with bypass duct.

The test section was enclosed by an annulus that ensured a uniform temperature profile entered the test section. Figure 3.3 is a plot of the temperature difference profile taken through the test section at the conditions noted. The greatest deviation from the average temperature was within the precision limits for the thermocouple used for the traverse. A cross-section of the test section and annulus is shown in Figure 3.4. Air velocity through the test section was controlled by orifices placed at the exit of the section. The orifices were 15mm x 60mm Plexiglas pieces with one to seven evenly spaced 6.35mm diameter holes.
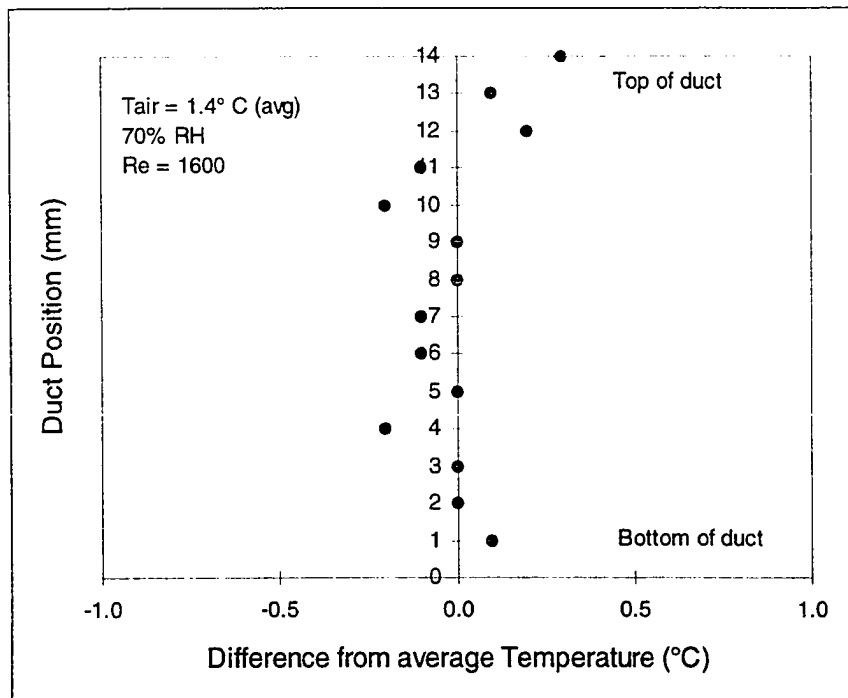
Figure 3.3. Temperature deviation through the vertical cross-section of the test duct.
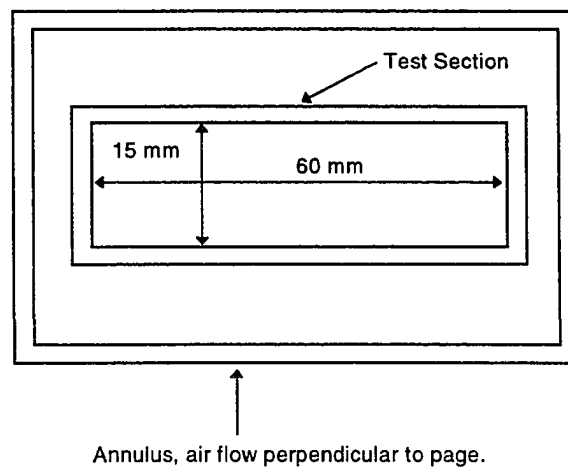
Figure 3.4. Cross section of Plexiglas annulus and test duct.

The combination of an orifice and slide damper setting determined the velocity in the test section. A flow conditioner consisting of a bundle of thinwall, hollow plastic tubes was placed in the entrance to the test section. The placement of the flow conditioner followed ASME Standard MFC-3M-1989. The tubes were 30 mm in length and approximately 3 mm in diameter. Air flow velocity was measured at the centerline of the test duct using a TSI Inc., model #1051-1-D hot wire anemometer with platinum wire probe #1210-20. Typical laminar flow profiles were obtained with this system. A plot of the profile for an average velocity of 0.25 meters per second (mps) is shown in Figure 3.5. Figure 3.6 shows the test section as installed.
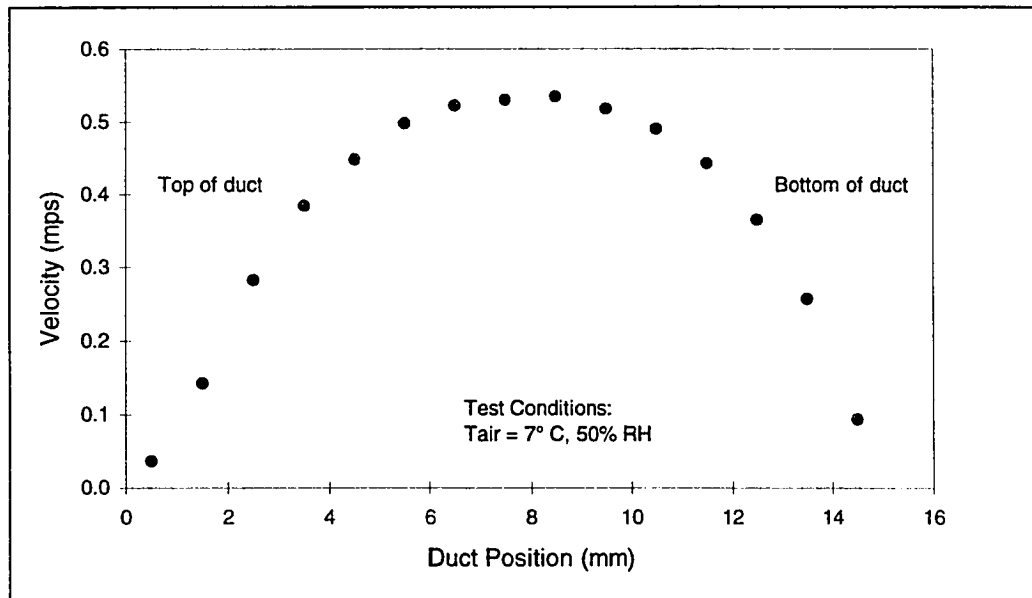
Figure 3.5. Velocity profile through test section, bottom to top of duct.
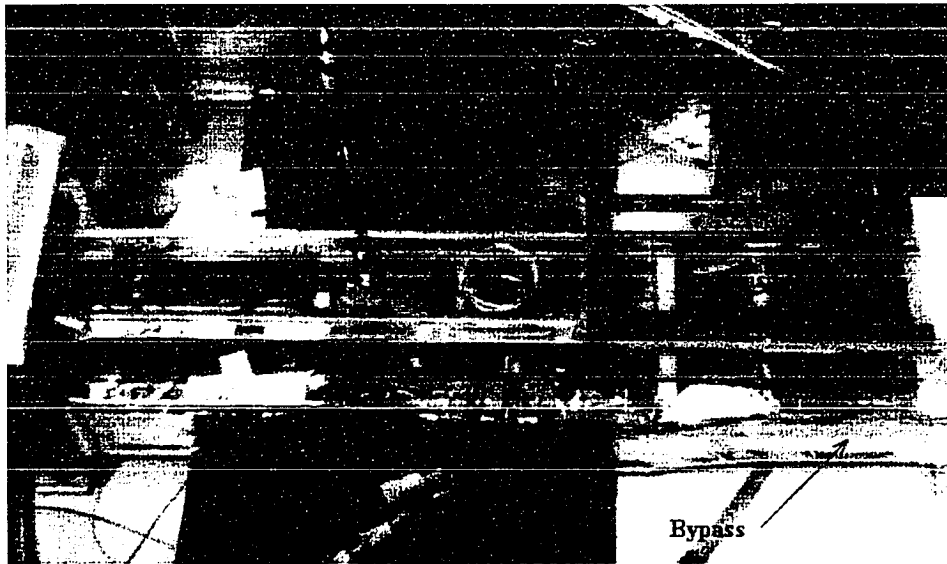
Figure 3.6. View of clear test section.

A test platform (see Figure 3.7) was fabricated to provide a consistent surface to which test specimens could be mounted and tested. This figure shows a vertical orientation for the test platform. However, for all tests done in this study the test platform was mounted in a horizontal orientation. The main body of the platform was a copper channel (approximately 40 mm x 40 mm x 25mm) with inlet and outlet connections to permit circulation of chilled ethylene-glycol and water solution. This formed the heat sink for the thermoelectric cooling element (TEC). A receiving socket was constructed on the bottom of the test duct section to accept the heat sink platform. The socket was positioned such that a 30 mm x 30 mm test surface could be mounted centered and flush with the inside bottom of the Plexiglass test section duct.
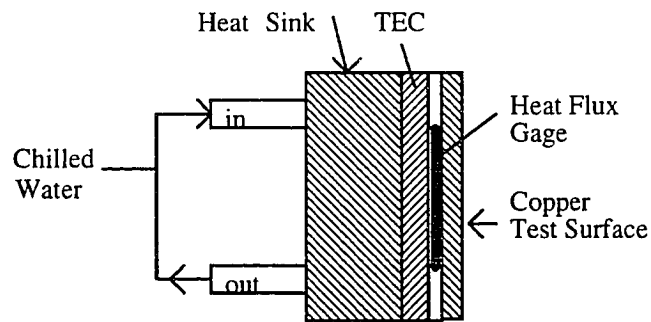
Figure 3.7. Surface testing platform.

A thin-film heat flux gauge (RDF model #27070-2) was mounted to the surface of a thermoelectric heating and cooling module (Melcor model #CP.1.4-71-06L) and below the copper test specimen. The TEC was capable of cooling the test surface (30mm x 30mm copper) to -20°C and heating up to 120°C.

The copper samples were cut from sheet stock of approximately 0.7 mm thickness and milled to a finish dimension of 30.0 x 30.0 mm. From early tests, it was found that the surface had to be highly reflective to provide reproducible droplet images. For this reason, the copper samples were buffed and successively polished to a "mirror smooth" finish of about 0.12 μm. The residue from the polishing operation was cleaned off of the surface with an initial wash of toluene, followed by a final rinse of methyl alcohol. No further surface polishing was done for the duration of tests on a given sample.

After the uncoated tests were finished, the copper surface was sprayed in situ with a siliconized polymer. These silicone coatings are commonly used on printed circuit boards to provide moisture and dielectric protection. The exact formulation is not known due to the proprietary nature of the product. After spraying, the surface was heated to approximately 60.0° C to aid in curing the coating. The TEC was used to heat the plate. This method was preferred because it minimized handling and possible repositioning of the plate with its heat flux gauge.

One other coating technology was also tested. Dr. Richard Crooks of the Texas A&M Chemistry Department, had developed a class of long-chain polymers that form a molecular bond with Au and Cu surfaces. The coating was durable up to 100°C and was of molecular thickness. The coating produced contact angles for water at room temperature of approximately 110° versus 100° for the silicone coating and about 85 - 90° for the uncoated copper sample.

To view the microscopic stages of the condensation process, a stereo dissecting microscope was mounted as shown in Figure 3.8. Attached to the eyepiece of the microscope was a high resolution charge coupled device (CCD) camera (COHU model 101). The combination provided magnifications of 100 to 280x with the ability to resolve liquid droplets as small as five μm in diameter ($\pm$2 μm). The images from the microscope system were either recorded on videotape or by a digital image capture board (Data Translation model #EZ) installed in a x486 based IBM compatible micro-computer. These images were then analyzed with imaging software (Jandel Scientific - Mocha) for droplet sizes and drop distributions. All pictures for this study were taken using this system.

During a test, data were recorded automatically by a micro-computer based data acquisition system. Data included; surface temperature, air temperature, heat flux through the test surface, air velocity, and relative humidity. Variables controlled during experiments included: hydrophobic and non-hydrophobic surface treatment on test specimens, surface temperatures from -15°C to 60°C ($\pm$0.5°C), air temperatures from 0°C to 35°C ($\pm$0.5°C), relative humidities from 20% to 90% ($\pm$3%), and air flow velocities of 0.5 to 1.5 m/s ($\pm$0.05 m/s). This flow range ensured laminar flow with Reynolds numbers from 650 to 2000 over the test surface.
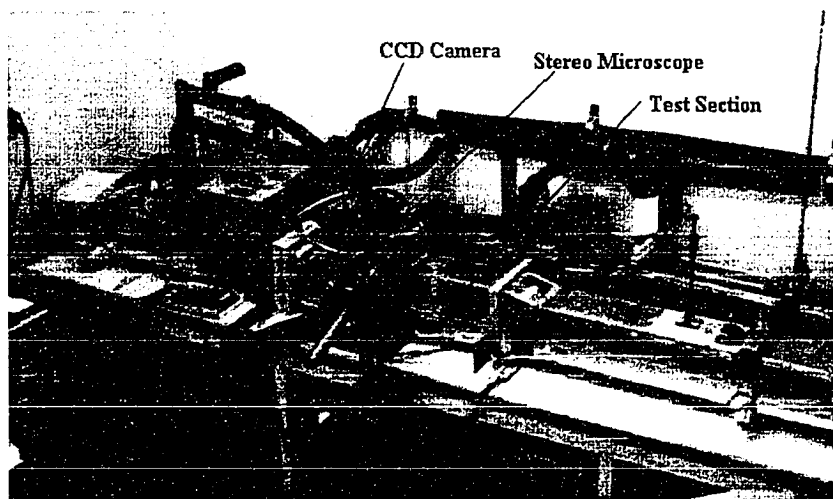
Figure 3.8. Digital photograph of the experimental apparatus.

Test Procedure

A typical experimental test run consisted of the following steps and procedures.

1. The chiller was set to supply glycol solution to the cooling heat exchangers that would maintain the desired air supply temperature to the test section. For example, for a desired air temperature of 7°C the chiller supply temperature would be set to approximately -10°C.

2. The blower would be turned on.

3. The controller would be set to maintain the desired supply air temperature to the test section.

4. The TEC heat sink chiller would be turned on and set to maintain a glycol solution supply temperature of approximately 10°C.

5. As the air temperature entering the test section approached the setpoint, the bypass damper would be adjusted to provide the desired air velocity through the test section.

6.   The Strawberry Tree data logging system was set to begin recording surface temperature, air temperature, surface heat flux, air velocity, and relative humidity.

7.   The TEC was connected to the DC current source and set to maintain the desired test specimen surface temperature (typically -10°C) for the duration of the test.

8.   Data scans were taken at one second intervals until the test was terminated. Tests were terminated when the liquid droplets in the view area of the microscope began to nucleate to ice.

9.   The data were stored to disk in a comma delimited file format that could be used for subsequent data reduction and analysis.

Calibration

The TSI anemometer was calibrated using a low velocity wind tunnel designed specifically for calibration of TSI hot-wire anemometers. Flow was varied from 0.15 - 2.0 mps and velocity was read as inches of differential pressure. The data were fit to a curve using a least squares regression. The RDF heat flux gauge had been calibrated at the factory and was shipped with it's calibration information. The Vaisala relative humidity sensor was calibrated against saturated salt solutions of lithium chloride and sodium chloride (11 and 75% relative humidity respectively). The sensor was within its stated accuracy of 2% of reading at both levels of relative humidity. All thermocouples used in this work were constructed from type T (copper-constantan) thermocouple wire. The averaging probe for the air side temperature measurements consisted of five constantan junctions soldered onto a 12 gauge copper wire. The surface temperature was obtained using the single wire method (ASTM, 1972). Using a 0.5mm graphite rod as a welding rod, a 44 gauge constantan wire was welded into the top surface of the copper plate to be tested. The thermocouple circuit was completed by soldering a copper wire to

the back of the test plate. This type of thermocouple circuit provides an average surface temperature for the entire plate versus using the more typical single point type thermocouple which provides very localized temperature only. All thermocouples were calibrated at the ice point using an insulated flask filled with a mixture of distilled water and chipped ice (ANSI/ASME PTC 19.3-1985). This provided any required offset information for the data logger software. The type T thermocouples are very linear in the temperature ranges used in this study, therefore no slope corrections were required beyond the single point calibration.

Image Analysis

Analysis of the digitally captured images was a major effort for this study. The biological sciences have been using these techniques for several years and most software is adapted to their requirements. Several visits were made to the Microscopy Center at Texas A&M University to study some of these methods and to do some exploratory imaging. These visits helped in the development of the imaging techniques used in this study.

A primary result of the early imaging efforts was that a highly polished condensing surface was required to be able to obtain reasonable images of the droplets that were growing on the surface. This has to do with the "noise" in the digital image. A typical rough metal surface reflects light in all directions and the addition of water to the surface only adds to the defraction of the incident light. This leads to a very "noisy" signal at the focal plane of the CCD camera and the resulting digitized image is very difficult to analyze. Additionally, the droplets reflect, as intense spots of light, the lights used to illuminate the surface. Upon determining this fact, it became apparent why researchers doing any imaging with their condensation work use highly polished surfaces. To help

eliminate the reflected spots of light from the droplets, an indirect lighting technique was used. This setup is shown schematically in Figure 3.9. Here, the fiberoptic lightpipe is aligned almost horizontally above the surface with the end of the pipe located above the area of interest. This technique brightly illuminated the polished metal surface and caused the droplets to appear as black objects on a white background. A typical image with this illumination is shown in Figure 3.10.
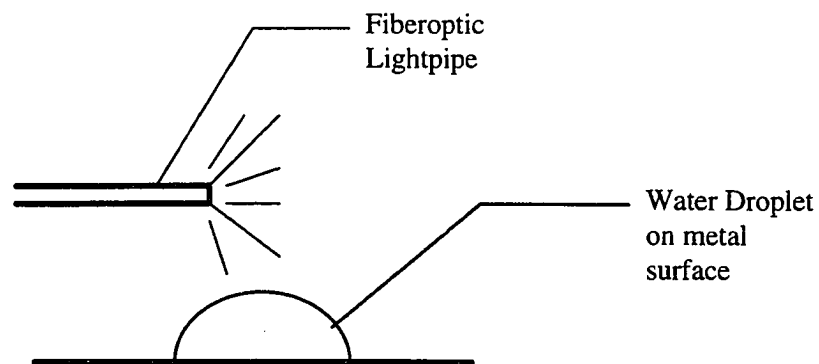
Figure 3.9. Indirect lighting on condensing droplet.
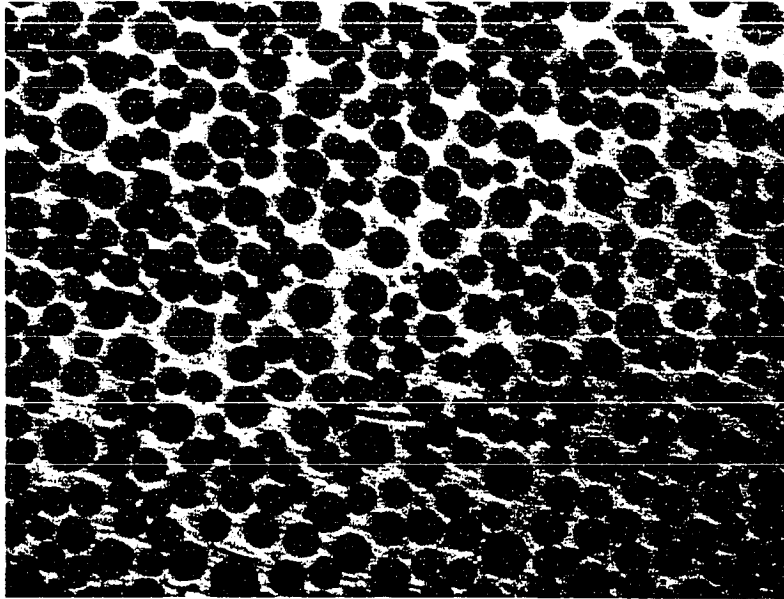
Figure 3.10. Example of indirect lighting on polished metal surface with condensing
water droplets.

The image shown in Figure 3.10 was at a magnification of approximately 100x. Small
white dots were visible at the center of each of the liquid droplets. This was the only
reflection from the illuminating light. Interestingly, when the water droplets nucleated to
ice, the index of light refraction changed and the white dot disappeared. This gave good
visual feedback as to when the nucleation to ice had started in the field of view.

All images captured with the digital imaging system were calibrated by using a
precision microscope calibration stage. This stage had two millimeter graduations
divided into 100 micron sections and one section of ten micron divisions. Figure 3.11 is
a digital image of the stage used for these calibrations.
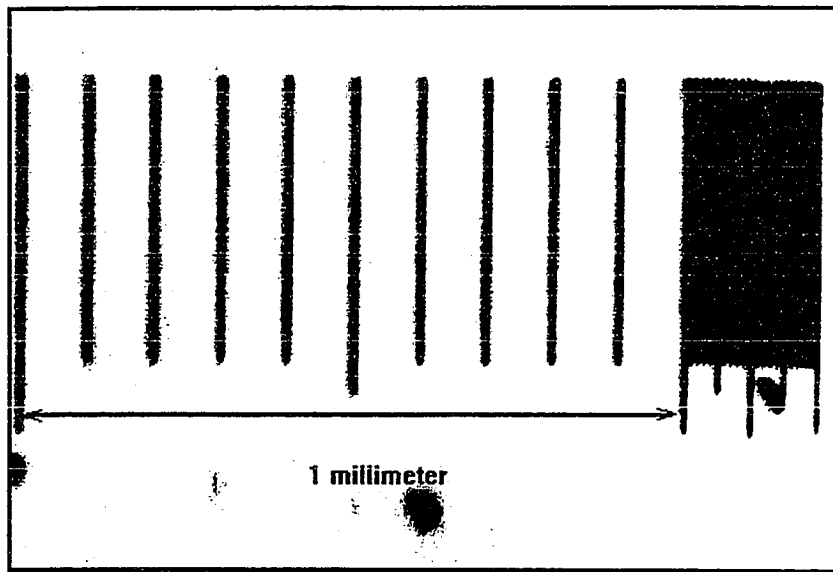
Figure 3.11. Microscope stage for image calibration.

If one has a "clean" image to work with, it would be a straight-forward process to analyze the digital image. A series of pixel operations (erosion and dilation) allows the separation of touching objects which can then be sized and counted. The human eye can quite easily discern the individual droplets in Figure 3.10. However, it would be a very daunting task manually to size and count all of the droplets in such an image. Unfortunately, the images are "dirty" enough that an extraordinary amount of hand labor was required to properly render the images before the droplets could be analyzed automatically. The process consisted of using the overlays in the software to delineate each droplet separately. Figure 3.12 shows the first step in such a process.
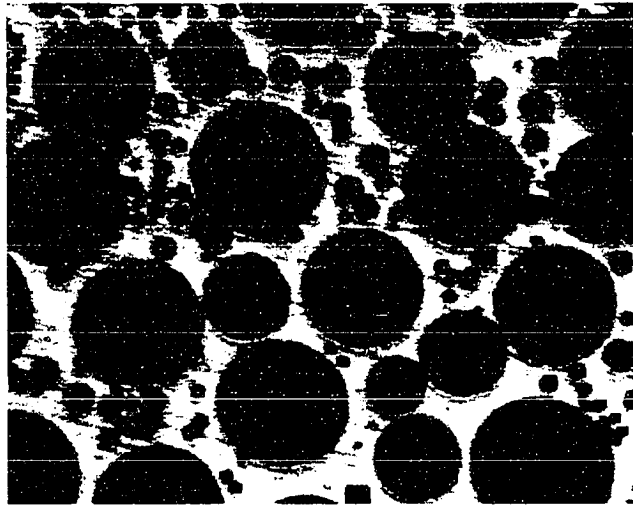
Figure 3.12. Droplets that have been separated and identified with an overlay.

This image started out similar to the image of Figure 3.10. Each droplet in this image was outlined by hand, then automatically filled-in with a distinctive overlay color. The droplets in the above image would show as red droplets in a color picture. Though painstaking, the hand work ensured that no droplets were touching each other. This was important because if just the corners of two pixels were touching, the sizing and counting software assumed that the two pixels were part of the same image. After the droplets were separated and overlaid, the measurement analysis of the image could begin. The software counted all of the separated objects and calculated a feret diameter for each object. The feret diameter is a fictitious diameter defined as the cross-sectional area of a two-dimensional object divided by the length of its perimeter. This procedure calculated the diameter of a perfect circle that had an area equal to the object being measured. Though not an actual diameter measurement, the droplets for all imaging were very close to circular in plan view. Upon completing the count and sizing for a given image, the software would write a comma-delimited file that could then be imported into other programs as needed for additional data reduction.

Several images were evaluated a number of times as a check of the repeatability of the outlining process. Sets of data taken this way were compared and no measurable differences were noted. The accuracy of the process was somewhat subjective. The droplet images did not have sharp borders which would have guided the outlining process. Because of this difficulty, images of the early stages of the condensation process were particularly difficult to reduce. As a general guide, droplets that were less than about five microns in diameter were not outlined. Droplets larger than that diameter presented an image that could be outlined successfully. With the imaging quality and the subjective nature of the droplet outlining process, an uncertainty of approximately ± 2 microns was assigned to the diameter dimensions taken from the digital images.

Experimental Uncertainty

Table 3.1 lists the uncertainties associated with the dependent variables used in this study.

Table 3.1. Experimental uncertainties in dependent variables.

Dependent Variable	Uncertainty ($\pm$)
Nusselt Number	5% of value
Reynolds Number	5% of value
h - average heat transfer coefficient	2 (W/m^2°C)
Nucleation Time	15 seconds
Droplet size	2 μm
Grashoff Number	5% of value
Droplet Surface Mass Density	10% of value

CHAPTER IV

EXPERIMENTAL RESULTS AND DISCUSSION

This chapter presents the results of experimental work performed in support of the present research. When possible, the results are compared with other studies. However, as discussed in Chapter II, no previous investigations were identified that are directly comparable.

Experiment Design

To facilitate statistical analysis of the experimental results and provide a limit on the number of experiments to perform, a 2^4 factorial design was chosen. This design indicated four factors at two levels. The factors and levels chosen for control were:

1. Bulk air temperature (1.5° C and 7.0° C)

2. Bulk air moisture content (50% RH and 80% RH)

3. Bulk air velocity (0.3 m/s and 0.8 m/s)

4. Surface treatment (coated and uncoated).

This design lent itself well to an analysis of variance (ANOVA) and greatly reduced the number of one-at-a-time type experiments that would normally would have been required. Table 4.1 shows the complete experiment matrix. The test conditions were chosen to represent the range of values typically encountered during the heat pump heating cycle. All tests were conducted on a flat, polished copper plate mounted horizontally in a rectangular duct. Refer to Chapter III for a complete description of the experimental apparatus and of the types of surface treatments used in this study.

Table 4.1. Factorial experiment design, 4 factor study.

RUN	Tair (C)	RH (%)	Avg. Velocity (m/s)	Coating (U, C)*
1	1.5	50	0.3	U
2	7.0	50	0.3	U
3	1.5	80	0.3	U
4	7.0	80	0.3	U
5	1.5	50	0.8	U
6	7.0	50	0.8	U
7	1.5	80	0.8	U
8	7.0	80	0.8	U
9	1.5	50	0.3	C
10	7.0	50	0.3	C
11	1.5	80	0.3	C
12	7.0	80	0.3	C
13	1.5	50	0.8	C
14	7.0	50	0.8	C
15	1.5	80	0.8	C
16	7.0	80	0.8	C

*Uncoated, Coated

Baseline Experiments

Over 80 experimental runs (in addition to the factorial experimental runs) were conducted with the horizontal plate in the heating mode to compare with published heat transfer correlations and provide baseline heat transfer characteristics for the flat plate/duct system. These experiments provided baseline operational characteristics for the system and, through the comparisons with the published correlations, established confidence in the results for a given set of experimental data.

The plate was heated to temperatures above the surrounding air temperature and data taken for average surface heat flux, average surface temperature, and average air velocity. Surface temperatures were varied from 10 to 60° C and the air velocity was

varied from 0.3 to 0.8 m/s. It should be noted that all fluid properties were evaluated at the film temperature

$$T_f = (T_g + T_w)/2 \qquad\qquad 4.1$$

and the length of the plate was chosen as the characteristic length (L). The Reynolds number was calculated for external flow over a flat plate. The average Nusselt number was determined from the experimental heat transfer data. The average heat flux (Q) to the surface was divided by the temperature difference (T_g - T_w) to directly yield the heat transfer coefficient $\bar{h}$ (W/m^2 °C) for a given experimental data set.

Figure 4.1 shows the results of 87 test runs in terms of the Nusselt (Nu) number versus the Reynolds number. Uncertainty bars were included in this figure to show the magnitude of error in the experimental Nusselt number. For comparison, an analytical expression relating the Nusselt number to the Reynolds number is also shown (Incropera and DeWitt, 1985). This equation predicted the average Nusselt number for fully developed laminar flow over a horizontal, heated plate of length L. The equation was developed for a plate with uniform heat flux rather than a uniform temperature at the surface. The equation used was

$$Nu = 0.906\ Re^{0.5}\ Pr^{0.33} \qquad\qquad 4.2$$
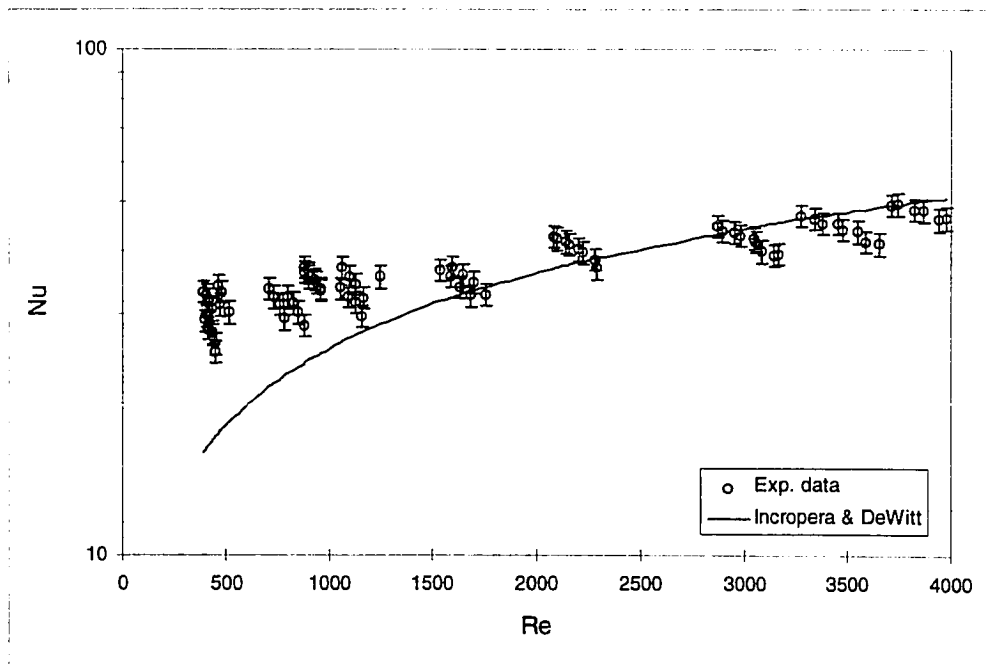
Figure 4.1. Heated plate heat transfer data, copper test surface.

There was very good agreement (less than 20% deviation) between the analytical

equation and the experimental results for Reynolds (Re) numbers of approximately 1200

and above. At lower Re, the difference between the analytical equation and experimental

data began to diverge quite rapidly. As stated in Incropera and DeWitt (1985) though,

deviations of 25% or more could be expected when comparing a given equation to

experimental data.

A check of the Rayleigh number (a product of the Grashof and Prandtl numbers)

for these experiments showed values from 34,000 to 110,000 which were below the 10^9

value typically accepted as applicable for free convection effects. Another test (Incropera

and DeWitt, 1985) for the combined effects of forced and free convection was the

evaluation of the quotient, Gr/Re^2. If Gr/Re^2 was much less than one, then free

convection effects could be neglected. If Gr/Re^2 was much greater than one, then forced

convection was negligible. But if Gr/Re^2 was approximately equal to one then the effects of both forced and free convection were present. For the heated plate experiments, the quotient Gr/Re^2 varied from 0.966 to 0.007 for Re of 400 to 4900, respectively. Using the above inequalities as a guide, it seemed apparent that combined free and forced convective heat transfer mechanisms coexisted. The Gr/Re^2 remained approximately equal to one (relatively speaking) for Re in the range of 400 to 1000. As seen in Figure 4.1, the forced convection *only* correlation began to underpredict Nu at Re of approximately 1000 to 1200.

Churchill (1977), presented a general correlation for combined free and forced convection as

$$Nu = Nu_F^n + Nu_N^n \qquad\qquad 4.3$$

where the subscripts F and N represented forced and natural (free) convection, respectively. The power n, was usually determined from experimental data. When $n = 3$, the value of equation 4.3 matched the analytical correlation values given by equation 4.2. At lower values of n, equation 4.2 allowed more contribution from the free convective component. Equation 4.3 was rewritten in a form recommended by Churchill to allow direct evaluation of Nu and is given by

$$Nu = Nu_F \left(1 + \left(\frac{Nu_N}{Nu_F} \right)^n \right)^{1/n} \qquad\qquad 4.4$$

Nu_F was given by equation 4.2 and Nu_N for a horizontal flat plate was given by (Sucec, 1985) as

$$Nu_N = 0.662 \, Ra^{.25} \qquad\qquad 4.5$$

Equation 4.4 was used with the experimental data to evaluate the power n as approximately 1.2. Equation 4.4 thus becomes

$$Nu = Nu_F \left(1 + \left(\frac{Nu_N}{Nu_F} \right)^{1.2} \right)^{.83}$$
<div align="right">4.6</div>

This equation with ±25% uncertainty bands are shown in Figure 4.2. Equation 4.6 did seem to describe the experimental data. However, a more accurate method for use in determining the effect of condensation would be to correlate the experimental data directly for these particular tests. A common form for these type correlations was given as (Incropera and DeWitt, 1985)

$$Nu = C \, Re^a \, Pr^b$$
<div align="right">4.7</div>

where the constant C and the exponents of a and b are determined from the experimental curve fit. Using this form and the experimental values for Re and Pr the following correlating equation was determined

$$Nu = 10 Re^{0.2} \, Pr^{0.33}$$
<div align="right">4.8</div>

This equation has a multiple r (correlation coefficient) of 0.89 as calculated from the regression of the experimental data.
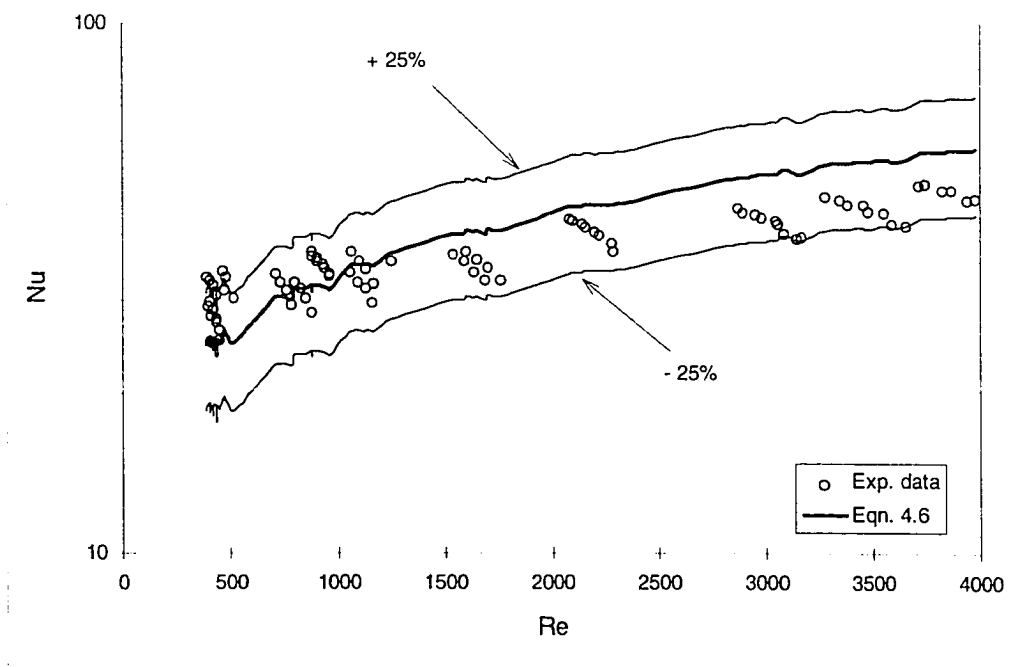
Figure 4.2.   Correlated experimental heat transfer data with free convection effects, heated copper plate.

The form of equation 4.8 compares well with the analytical solution given in equation 4.2. A graph of equation 4.8 with the experimental data is shown in Figure 4.3. Though a good statistical fit, the correlation given by equation 4.8 still did not address the problem of the vertical scatter in the data. The free convective checks indicated that free convection effects were present, especially at $Re < 750$, but the combined effects correlation given by equation 4.6 also didn't adequately address the scatter in the data
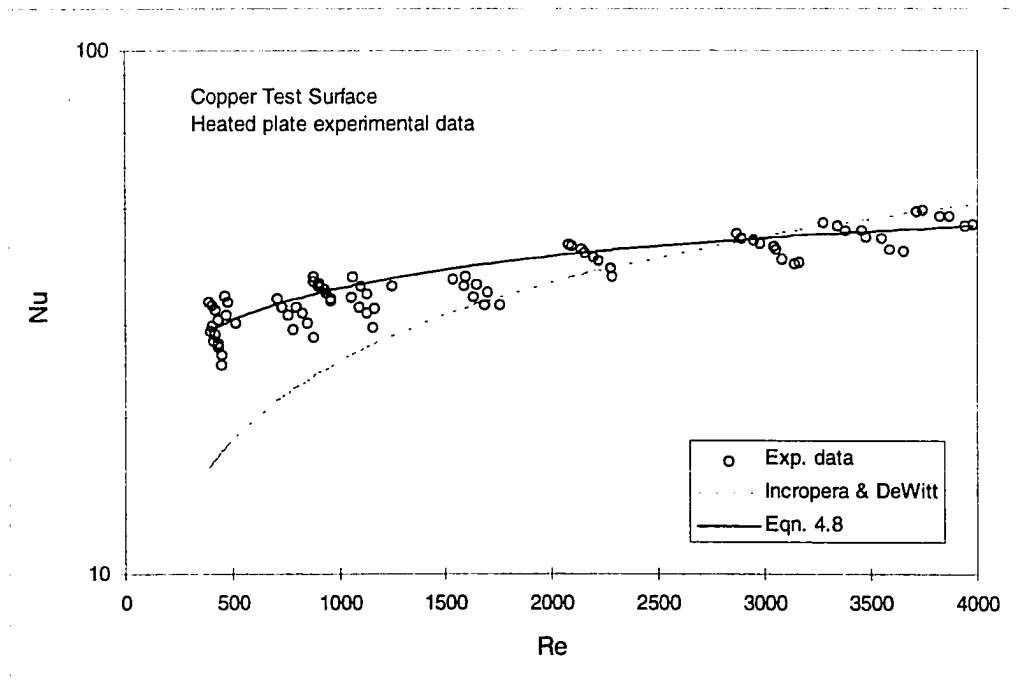
Figure 4.3. Correlated heat transfer data using equation 4.8 vs. equation 4.2.

Another correlating equation was available if free convective effects and large temperature differences were present (Bird, Stewart, and Lightfoot, 1960). The Grashof number could be added to the set of nondimensional groups as given in equation 4.7 to address the free convective effects. Since the fluid properties were all evaluated at the film temperature as given in equation 4.1, significant errors could result when large temperature differences were generated between the bulk fluid and the surface. A ratio of the viscosity of the air evaluated at the fluid temperature and at the surface temperature could also be added to equation 4.7. The resulting equation was given by

$$Nu = C\,Re^{a}\,Gr^{b}\,Pr^{c}\,(\nu_g/\nu_w)^{d} \qquad\qquad 4.9$$

Using this form, a correlation of the experimental data gave the following equation for the average Nusselt number as

$$Nu = 937 \, \text{Re}^{0.2} \, \text{Gr}^{-0.44} \, \text{Pr}^{0.33} \left(v_g / v_w \right)^{0.51} \qquad\qquad 4.10$$

From a statistical view point, either equation 4.8 or 4.10 could be used with the data for the heated plate experiments since both have similar correlation results. However, the form of equation 4.10 takes into account variations in the data due to free convective effects *and* temperature on fluid properties. Residuals for the heated plate experiments were calculated by subtracting the estimated *Nu* (given by the correlating equations) from the measured *Nu*. The residuals for the data as correlated by equation 4.10 are shown in Figure 4.4. This figure shows that the correlation given by equation 4.8 had considerably more spread about the zero line when compared to the residuals for equation 4.10. The residuals for equation 4.10 were also more normally distributed. Distinct vertical, spaced, groupings were identifiable in the residuals for equation 4.8. This further justified the inclusion of the Grashof number and the viscosity ratio as descriptive groups in the correlation of equation 4.10. With the heat transfer correlation as given in equation 4.10 for the dry heated plate, comparison could now be made to experiments with condensation occurring on the flat plate.
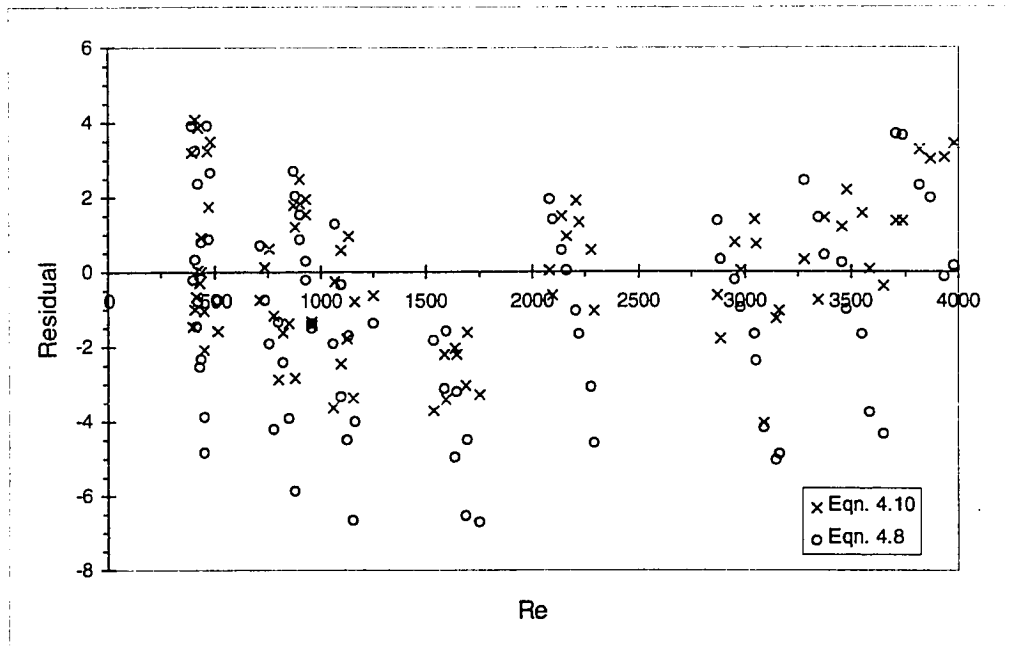
Figure 4.4. Heated plate experimental data residuals for equations 4.8 and 4.10.

Condensation Experiments

Over 80 sets of data were taken under the conditions as outlined in the experimental

plan in Table 4.1. Several intermediate points were also taken to complete the statistical

picture. This "lumped" data had all points included. As described in Chapter III

concerning the test surface, three different surfaces were tested. These were an uncoated

highly polished copper plate, the same plate coated with a siliconized polymer and

another polished copper plate coated with a sulfur based polymer. These raw heat

transfer data are shown in Figure 4.5. There were three rather distinct groupings for the

data and this was an consequence of the two level factorial experiment design with a

fewer number of data points at Re of approximately 1100. Using two levels of air

velocity translated into Re of approximately 600 and 1500. As with the heated plate

experiments, a rather large vertical spread was also evident in these data. For reference,

the previous correlation for the heated plate experiments given by equation 4.2 and the correlation given by equation 4.8 are also shown in Figure 4.5. Comparing the wetted plate Nusselt numbers to these correlations, an increase in the heat transfer for the horizontal plate with coincident condensation was evident. This increase was approximately 30% over the dry heated plate experiments. This is discussed further in following sections.
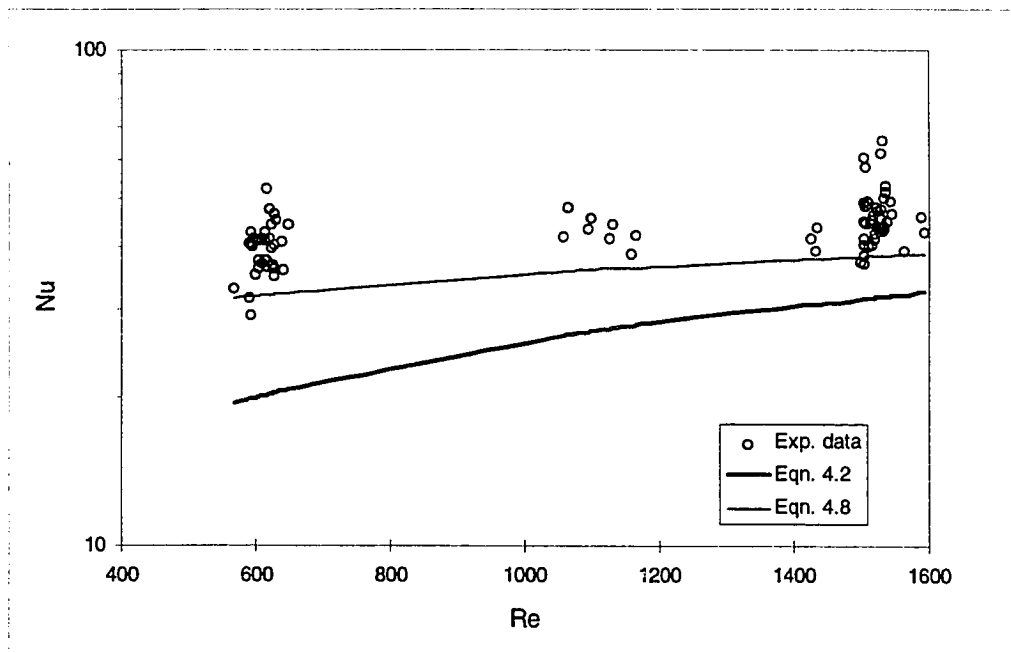
Figure 4.5. Heat transfer data for condensation experiments with comparison of dry, heated plate correlations.

From the above developments concerning free convection effects and the effect of temperature differences on the fluid properties, the functional form given in equation 4.7 should have been applicable to these data as well. A step-wise linear regression of the data with equation 4.7 gave the following correlation for the wetted plate data

$$Nu = 246\,\mathrm{Re}^{0.16}\,\mathrm{Gr}^{-0.24}\,\mathrm{Pr}^{0.33} \qquad\qquad 4.11$$

The form of the correlation did not include the viscosity ratio as in equation 4.10 because

the evaluation of the viscosity ratio for the condensation data showed an almost constant

value of 0.94 for all of the data points. Conversely, this ratio varied from 1.04 to 1.17 for

the heated plate data. Thus, the small temperature differences used in the condensation

experiments did not result in a large change in the air viscosity at the plate surface

compared to the ambient air. As with the heated plate experiment, the residuals for the

experimental Nu minus Nu from equation 4.11 are shown in Figure 4.6.
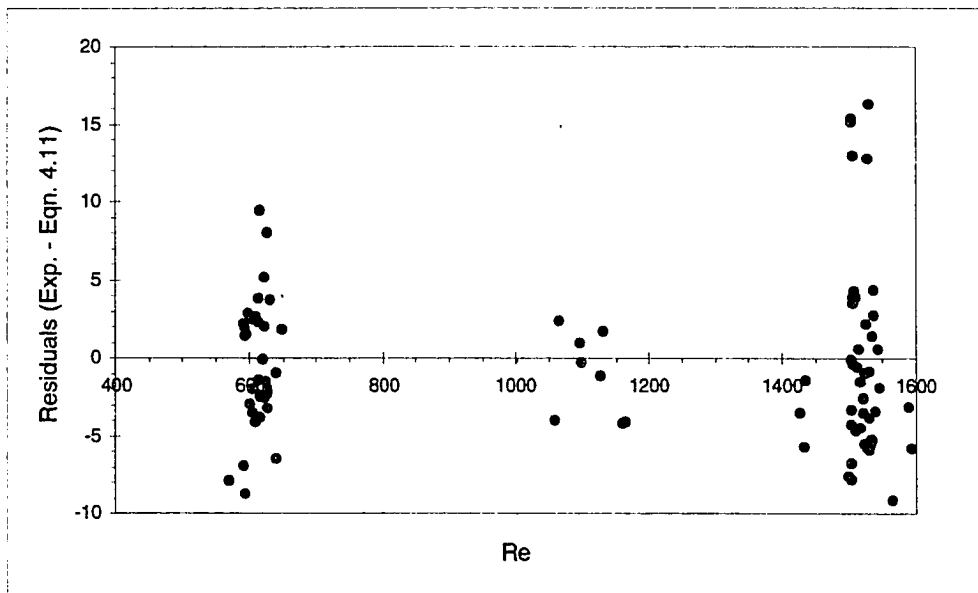
Figure 4.6. Residuals of experimental Nusselt minus Nusselt from equation 4.11.

Here, the residuals still had considerable vertical spread relative to the dry plate

data. This is to be expected due to the uncontrollable surface conditions that occur on the

plate as the condensation process progresses. The condensation activity contributed to

the overall heat transfer in the system through the addition of the heat of condensation and the increased convective heat transfer due to effective surface roughening. Though initially dry, microscopic droplets began to form and continued to grow and coalesce with each other as the surface temperature of the plate dropped below the dew point of the air-water vapor mixture flowing over it. Approximately 10 seconds into a typical condensation test, these droplets became visible to the unaided eye. At this point they were hemispherical in shape and approximately ten microns in diameter which meant they extended from the surface approximately five microns. This essentially roughened the surface thereby increasing heat transfer. Correlations have been developed (Sucec, 1985) that account for the addition of roughness elements in round duct and they are of the form

$$\frac{Nu}{Nu_{smooth}} = \left(\frac{f}{f_{smooth}} \right)^n \qquad 4.12$$

where the exponent n is usually taken as 0.57 for a Prandtl value of 0.71 (air). This equation expresses the ratio of the rough Nu to the Nu for a smooth duct as a ratio of the friction factors for rough and smooth raised to n. From this type equation, it is seen that any increase in the surface roughness leads to an increase in the Nusselt number, which results in an increase in heat transfer.

The increase in heat transfer for the plate undergoing condensation can be estimated by evaluating the difference of equation 4.11 and 4.10 at similar Re. The results are shown in Figure 4.7.
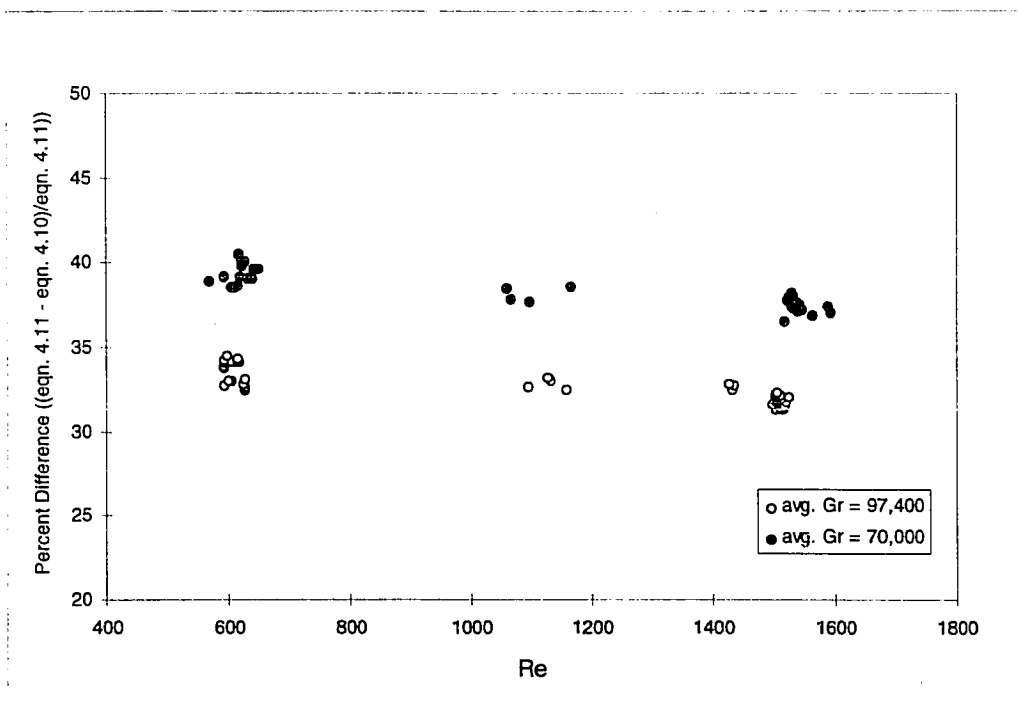
Figure 4.7. Enhancement of heat transfer with simultaneous condensation.

The percent differences varied from a low average of approximately 33% to a high average of 38%. The two level factorial statistical design resulted in two levels of Grashof numbers of approximately 70,000 and 97,000. Depending on the value of Gr there was between a 33 to 38% increase in overall average heat transfer for a plate undergoing condensation versus similar conditions on a dry plate. At higher Grashof numbers, the effect of free convection heat transfer was more pronounced, and this resulted in lower overall heat transfer (Figure 4.7). As the Grashof number decreased, the experimental correlations (equations 4.10 and 11) showed a greater difference which indicated greater influence of forced convection. Though not a startling revelation, the results of these tests are complimentary to other studies found in the literature concerning heat transfer during condensation. Studies done on dehumidifying equipment showed

increases of from 10 to 70% in sensible heat transfer for Re of 400 to 4000 (ASHRAE, 1993).

As stated above, for simultaneous heat and mass transfer processes, there was a sensible component as well as the heat of condensation occurring. The following section describes the development of the mass transfer relations for these experiments.

Mass Transfer

With appropriate assumptions (Bird, Stewart, and Lightfoot, 1960) it can be shown that the same functional form is applicable to local and average heat transfer Nusselt numbers as well as the local and average mass transfer Nusselt numbers. This similarity in form allows the direct evaluation of mass transfer correlations from the heat transfer correlations under similar boundary conditions. Thus, the functional form for the heat transfer Nusselt number given in equation 4.7 allows one to state the following form for the mass transfer Nusselt number as

$$Nu_m = Sherwood = C\,Re^a\,Sc^{\,b} \qquad\qquad 4.13$$

where C, a, and b are the same value determined from the correlation of the heat transfer data. The important assumptions that allow this analogy are;

1) constant physical properties for the fluid

2) low mass transfer rates

3) no chemical reactions in the fluid

4) no viscous dissipation

5) no emission or absorption of radiant energy, and

6) no pressure, thermal or forced diffusion.

At the conditions used for the current work, assumptions 1 and 2 are met, and the remaining assumptions may be neglected (Bird, et al., 1960). The analogy may also be

used to relate the two convective heat and mass transfer terms to obtain the Lewis relationship (Incropera and DeWitt, 1985).

$$\frac{Nu}{\Pr^{0.33}} = \frac{Sh}{Sc^{0.33}} \qquad\qquad 4.14$$

Substituting the definitions into equation 4.14 yields

$$\frac{hL}{k\,\Pr^{0.33}} = \frac{h_m L}{\mathcal{D}\,Sc^{0.33}} \qquad\qquad 4.15$$

Simplifying 4.15 leads to

$$\frac{h}{h_m} = \frac{k}{\mathcal{D}\,Le^{0.33}} = \rho c_p Le^{0.67} \qquad\qquad 4.16$$

Equation 4.16 is known as the Lewis analogy for heat and mass transfer and this relationship has been found to hold for most air/water vapor mixtures (Incropera and DeWitt, 1985). In the heat transfer section above, a correlation was developed describing the overall average heat transfer and was given by equation 4.11 as

$$Nu = 246\,\mathrm{Re}^{0.16}\,\mathrm{Gr}^{-0.24}\,\Pr^{0.33} \qquad\qquad 4.11$$

Using the above analogy, the Sherwood number for these experiments could be described by

$$Sh = 246\,\mathrm{Re}^{0.16}\,\mathrm{Gr}^{-0.24}Sc^{0.33} \qquad\qquad 4.17$$

Statistical Analysis

One of the primary goals of this research was to ascertain the efficacy of hydrophobic coatings to delay or mitigate the growth of ice and frost on a cold heat

exchanger surface. A convenient means to quantify the delaying effect of a given treatment presented itself through the nucleation time. This was the time at which the supercooled liquid water droplets on the surface would begin to nucleate to ice. These ice "embryos" have been shown to be the initial building blocks for the subsequent growth of frost [Tao, Besant, and Mao, 1993].

The experimental design as given in Figure 4.1 was used to generate the data for use in an analysis of variance (ANOVA). ANOVA methods are useful when multiple comparisons between experimental variables are desired. This method was chosen because of the multi-factor nature of this study. The 2^k factorial experimental design required 16 tests and multiple random data were also taken as replications. The four main factors: surface treatment, air velocity, air temperature, and air moisture content were varied at the levels as shown in Table 4.1. This experiment design method reduces considerably the number of experiments over the classical method of varying one variable at a time while holding all others constant.

The ANOVA was performed to quantify the effect of the different factors on the length of time that droplets of water required before nucleating to ice. As droplets of water grew and coalesced, they became supercooled and at some point during the test would nucleate from the liquid to the solid phase. During an experiment, data and droplet images were recorded until the liquid droplets in the microscope field of view began to nucleate to ice. At that point the data stream was terminated. That point in the run was then identified as the nucleation time for those experimental conditions.

It should be noted that water droplet nucleation did not occur on a repeatable basis. Numerous runs at the same conditions would yield a wide range of ice nucleation times. This phenomena has been extensively studied [Dorsey, 1948]. Dorsey's study covered a 12 year series of freezing and thawing of numerous water samples under different cooling

rates. He found that only after extreme measures to ensure elimination of contaminants and after thousands of freeze-thaw cycles could an individual water sample freezing time be determined with any accuracy. This behavior was found to be true in these tests. The stochastic nature of the nucleation event was another indicator for use of a statistical method to properly determine system effects.

The data were subjected to the multi-factor ANOVA and the resulting statistics are shown in Table 4.2. The Reynolds number was used as a substitute for velocity in these analyses. At the 95% confidence level, the factors T_g, Surface Treatment, and RH were important influences on the nucleation time ($p < 0.05$). The Re did not have a statistically significant effect on nucleation time. Several of the interactions were statistically significant. The interactions T_g - Surface Treatment, T_g - RH, Surface Treatment - RH, and RH - Re all had significance levels less than the critical p value of 0.05. These effects are most easily presented in graphical form. Nonsignificant interactions are indicated when the lines in the interaction plot are nearly parallel [Hinkle, et al., 1994]. Significant interactions on the other hand are indicated by non-parallel lines (ordinal interaction) or lines that intersect in the plot (disordinal interaction). Figure 4.8 shows the interaction for the factors T_g and Surface Treatment versus the response variable, nucleation time. It shows that depending on the temperature of the air for a given surface treatment there can be significant differences in the mean nucleation time. This was especially true at the lower air temperature of 1.5° C. The change in nucleation time was not as variable for the 7° C air temperature. Another way to interpret this plot is that for an air temperature of 1.5° C and a sulfur based molecular surface coating, one could expect the droplets on the -10° C surface to nucleate to ice about 17 minutes after the beginning of the condensation process. Conversely, if the surface is untreated, mean nucleation time would be at about 8.5 minutes. For all surface treatments, an air

temperature of 7° C resulted in a rather uniform nucleation time of approximately 6 minutes.

Table 4.2. Analysis of variance for droplet nucleation time - Type III sums of squares.

Source of variation	Sum of Squares	d.f.	Mean Square	F-ratio	Sig. level (p)
Main Factors					
A: T_g	666.59	1	666.59	119.96	0.0000
B: Surface Treatment	272.79	2	136.39	24.56	0.0000
C: RH	406.34	1	406.34	73.13	0.0000
D: Re	10.53	1	10.53	1.89	0.1731
Interactions					
AB	172.18	2	86.09	15.49	0.0000
AC	117.99	1	117.99	21.23	0.0000
AD	0.494	1	0.494	0.089	0.7697
BC	114.04	2	57.02	10.26	0.0001
BD	10.03	2	5.02	0.903	0.4102
CD	58.71	1	58.71	10.56	0.0018
ABC	25.99	2	12.99	2.34	0.1042
ABD	24.14	2	12.07	2.17	0.1219
ACD	3.33	1	3.33	0.60	0.4495
BCD	34.23	2	17.11	3.08	0.0525
ABCD	14.61	2	7.31	1.31	0.2753
Residual	372.29	67	5.56		
Total (Corrected)	2205.39	90			
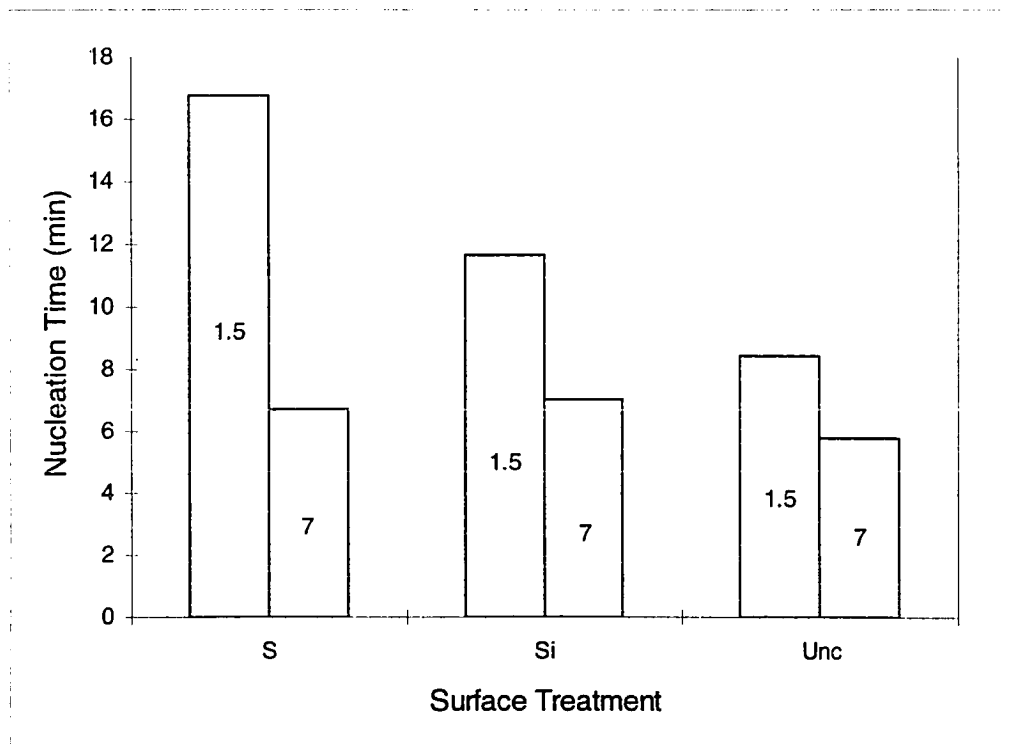
Figure 4.8. Interaction plot for surface treatment and air temperature on nucleation time.

A more dramatic ordinal interaction plot is shown in Figure 4.9. This interaction plot shows the effect on nucleation time of the interaction between surface treatment and level of relative humidity. It is clear that for "low" relative humidity of 55%, a given surface treatment would allow nucleation to ice at much longer and more varied times than at the "high" level of relative humidity. At 55% relative humidity the three surface treatments yielded mean nucleation times of 15.8, 11.0, and 8.0 minutes for sulfur, silicone, and uncoated respectively. At an 85% RH level these same surfaces had nucleation times of 7.7, 7.6, and 6.0 minutes.

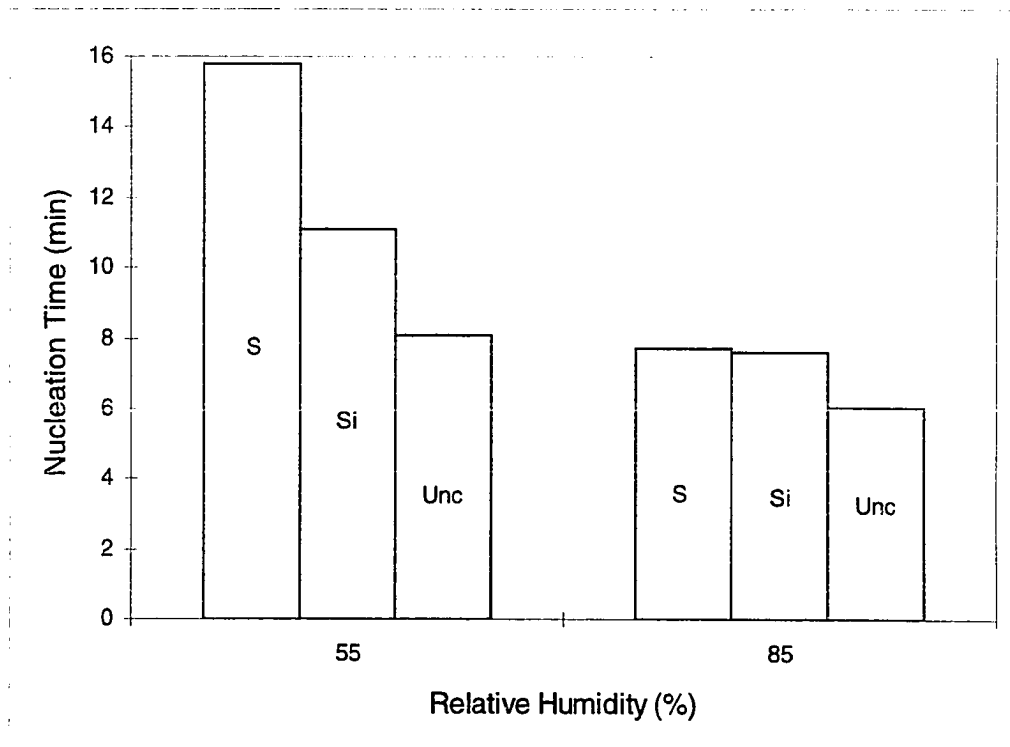Figure 4.9. Interaction plot for surface treatment and level of relative humidity on nucleation time.

The interaction for relative humidity and Re shows that only at the higher level of RH was there a significant change on the nucleation time with a change in Re. At 55% RH, the nucleation time variation with the Re number was approximately constant at 11.8 minutes. This interaction plot is shown in Figure 4.10.
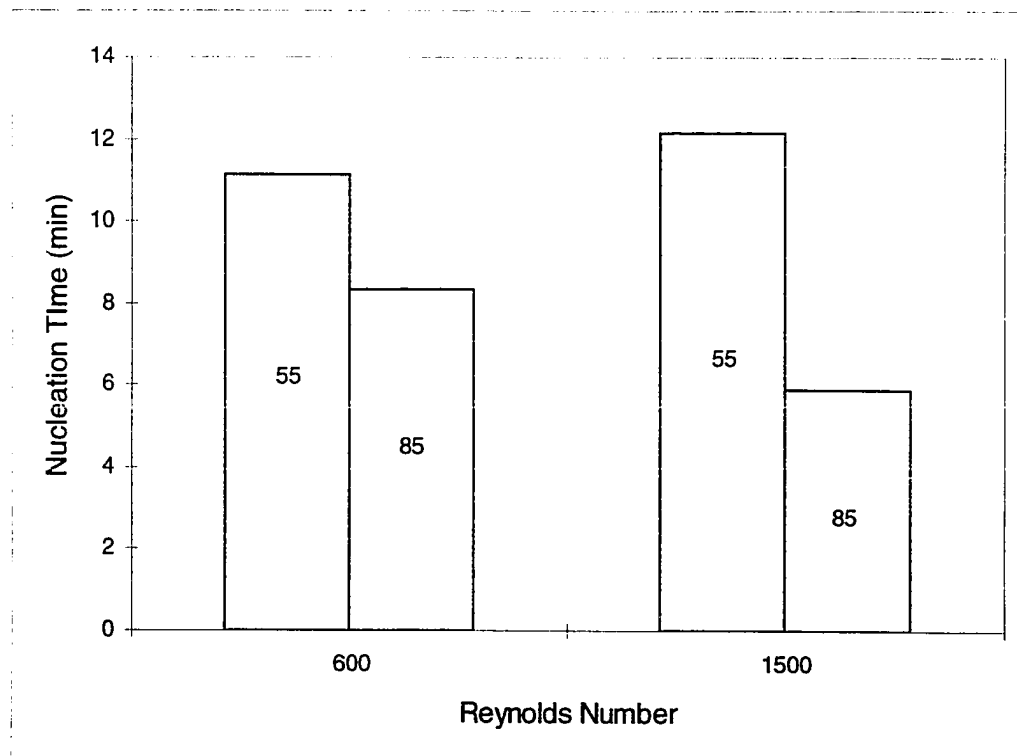
Figure 4.10. Interaction plot for Re and level of relative humidity on nucleation time.

Another strong ordinal interaction is shown in Figure 4.11. This interaction was between the air temperature and level of relative humidity. Here, there was a dramatic change in the mean nucleation time for a change for low to high relative humidity while at a low air temperature of 1.5°C. This combination had nucleation times varying from 15.8 minutes to 8.7 minutes. For air temperatures of 7.0°C, the variation in nucleation times varied from 7.5 to 5.5 minutes for a change of 55 to 85% RH.
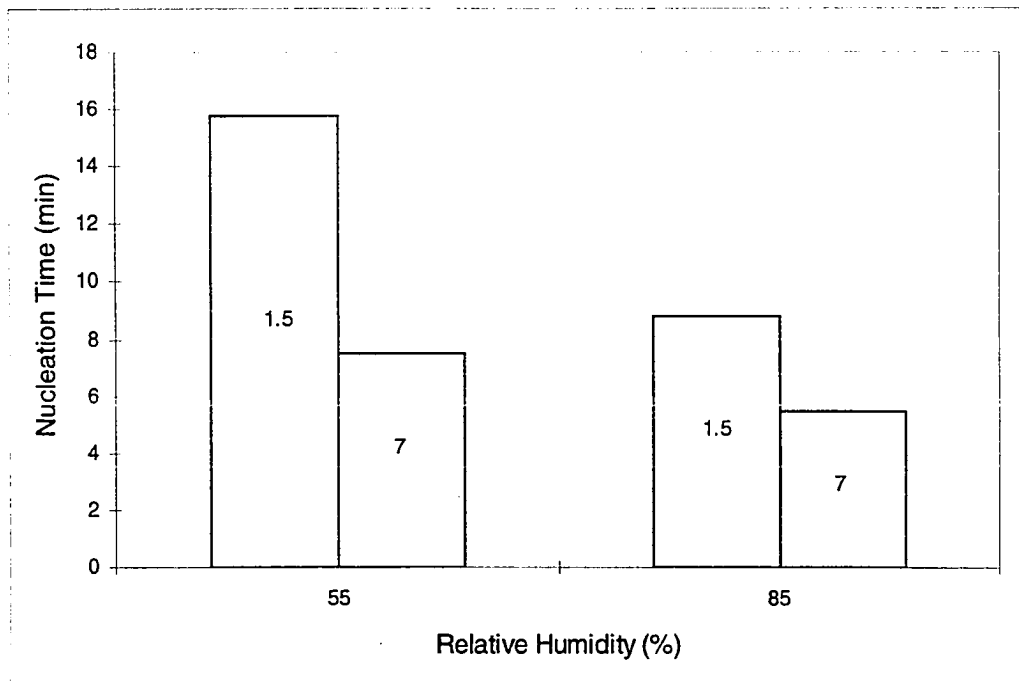
Figure 4.11. Interaction plot for RH and level of air temperature on nucleation time.

An example of a nonsignificant interaction (significance level > 0.05) is shown in Figure 4.12. This interaction shows the effect on nucleation time for the three surface treatments at different levels of the Re number. The sulfur and silicone coatings showed very little change in mean nucleation time with a change in Re. The change shown for the uncoated surface did show an effect due to the change in Re, but the change from 7.9 to 6.3 minutes was not statistically significant.
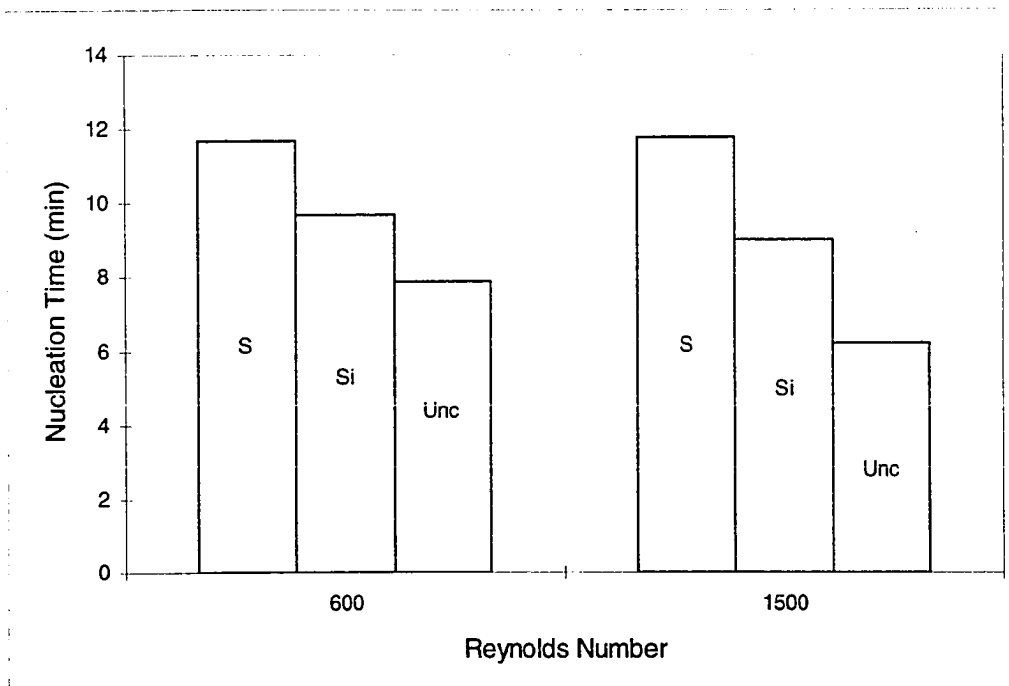
Figure 4.12. Interaction plot for Re and level of surface treatment on nucleation time.

The importance of the three factors T_g, Surface Treatment, and Relative Humidity, was reflected in the interaction plots and indicated that any model used to predict the nucleation time should include them. Even though the Re was not significant as a main effect, it did become important when combined with a given humidity level.

Means plots for these factors are shown in Figures 4.13 to 15. The fact that the 95% confidence intervals about the mean nucleation times did overlap for the factors Air Temperature, Surface Treatment or Relative Humidity indicated the statistical significance of their importance on this response.
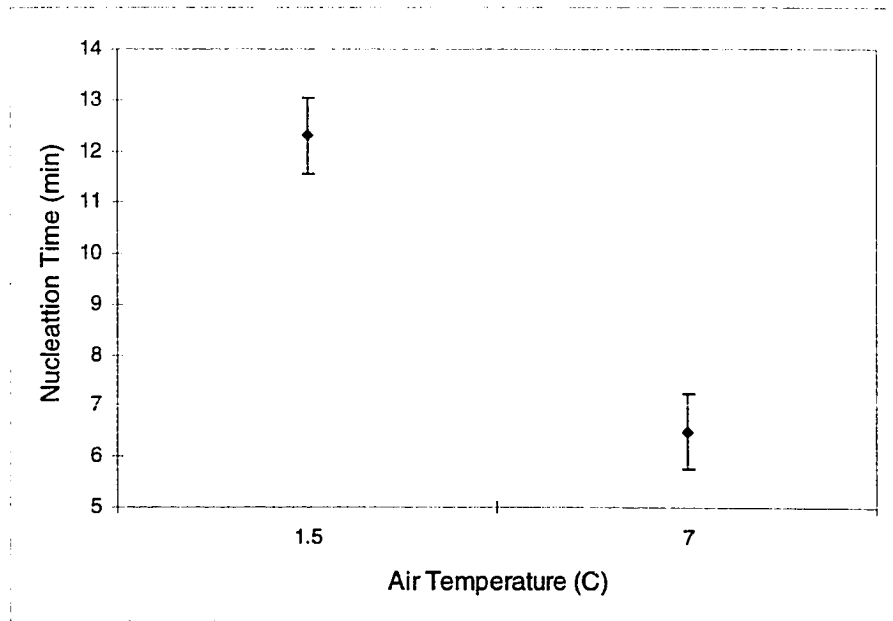
Figure 4.13. Means plot for factor air temperature on nucleation time.

Figure 4.14. Means plot for factor surface treatment on nucleation time.
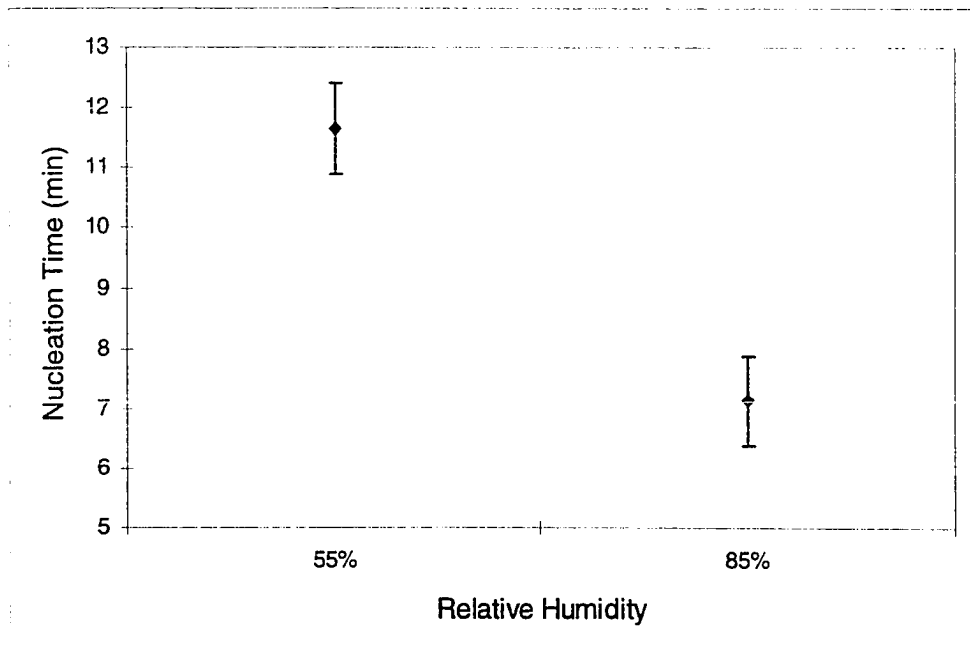
Figure 4.15. Means plot for factor relative humidity on nucleation time.

The means plot for the factor Re shows that the nucleation time for these tests did not have a strong dependence on the velocity of the air over the surface. This fact was shown in Figure 4.16 by the overlapping of the 95% confidence limits about the mean.
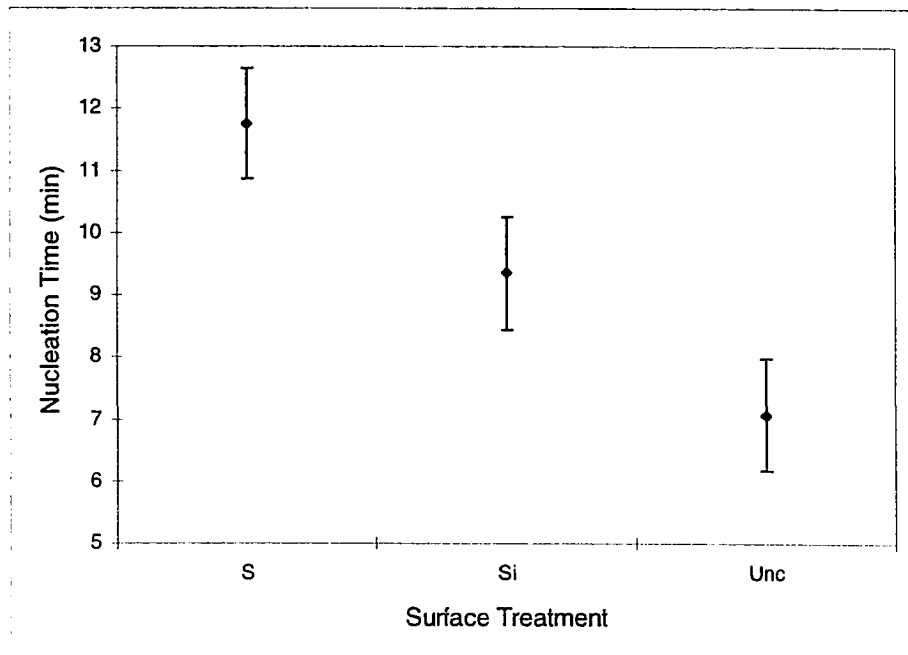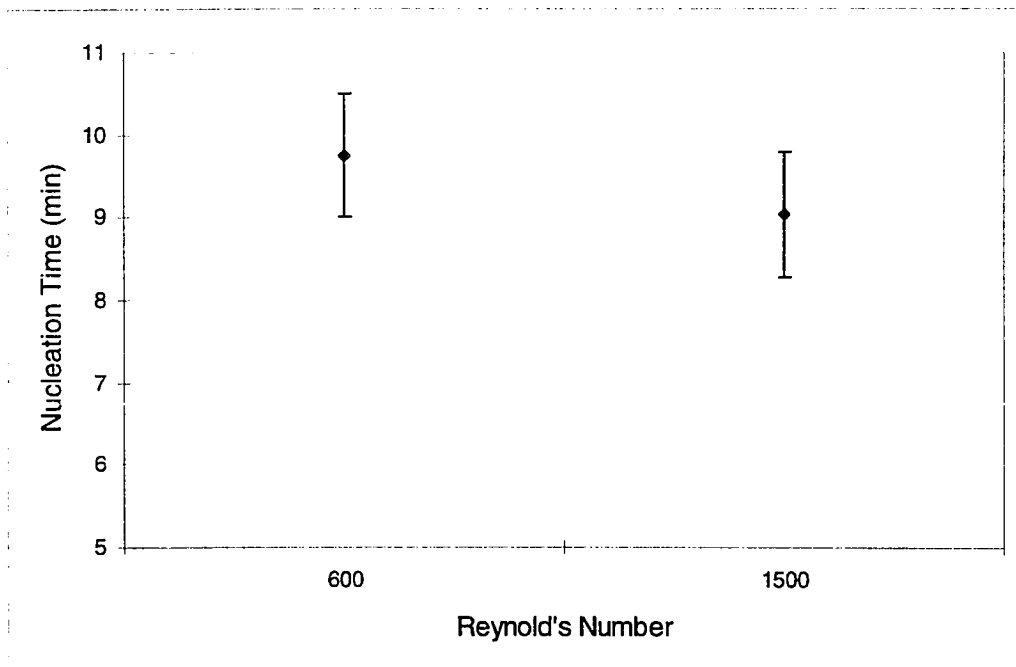
Figure 4.16. Means plot for factor Reynold's number on nucleation time.

The results of the statistical analysis on the effect of the identified factors on the

nucleation time can be summarized as follows; Air temperature, air relative humidity,

and surface treatment were all important influences on the nucleation time. The Re only

became significant when the air relative humidity was at a high level. As expected, there

were strong interactions between the statistically significant main factors. The Reynolds

number however, still did not exert a strong influence on the nucleation time. There were

several possible reasons for this lack of Reynolds number effect on nucleation time.

Under the conditions of the current work, flow was kept entirely laminar. The boundary

layer thickness for this type of flow regime was of the same order of magnitude or greater

than the radial (height) dimension of the condensing droplets. It is well known (Incropera

and DeWitt, 1985) that the conditions inside this boundary layer, temperature, flow, heat

flux, etc., are much different than in the free-stream. Thus, a condensing droplet does not

experience in a direct manner, the velocity gradient or the temperature gradient caused by the forced fluid (air) flow. The thick boundary layer could also cause a reduction in the interfacial mass transfer process. Additionally, there are three primary resistances to heat flow through a condensing droplet, and these resistances were given in terms of temperature differences by equations 2.18a, b, and c. An additional resistance has been suggested to account for the increased resistance to heat flow that a large drop imposes on a condensing surface (Mikic, 1968). The combination of the relatively thick and inactive boundary layer with the interfacial heat transfer resistances served to reduce the effects of the fluid velocity on the droplet.

It is apparent from these results that treating the surface of a metal plate with a hydrophobic coating did delay the time at which supercooled water nucleated to ice. These results are only applicable in the ranges used for this study, but the inference is that the use of coatings on other surfaces under similar conditions would have similar effects on the nucleation time.

Dropsize Distributions

As discussed by Tanaka (1975a), information on the distribution of droplet sizes is lacking compared to the available information concerning heat and mass transfer data for dropwise condensation. At the inception of this study it was hoped that the existing correlations for dropsize distributions in the steam literature would simply "port over" to the conditions of atmospheric condensation of humid air onto a cold surface. Unfortunately, the processes are so different that this was not possible. The same was true for heat or mass transfer correlations from the steam literature. These correlations yielded estimates for the heat and mass transfer coefficients that were orders of magnitude too large when evaluated at the conditions of this study. It was also found that many of

the published correlations for dropsize distributions required prior knowledge for the type of droplets on a given surface. This was most often expressed as a "characteristic radius " or one that was an average of the maximum size of droplets found on a given surface at prescribed operating conditions.

As stated earlier, dropsize distribution information is useful when determining the total heat flux for a condensation process. Equation 2.3 gave an expression for the overall heat transfer coefficient which requires knowledge about the dropsize distribution. Tao (1992) developed a "unit cell" model for frost growth, but had to assume the initial frozen embryo distribution.

Figures 2.3, 4, and 5 (Chapter II) all showed steady-state dropsize distribution curves for various conditions of steam condensation. Direct comparison was difficult because the heat fluxes for steam condensation were orders of magnitude larger than those of this study. Figure 4.17 shows the raw droplet image for one of the dropwise condensation experimental runs for this work. The conditions for this distribution were

$T_g = 1.2°$ C,

$T_w = -10.0°$ C, RH = 65%, Re $\approx$ 1500, and an uncoated copper surface.

This image was analyzed as described in Chapter III to determine the distribution of droplet sizes and the total mass of liquid water condensed onto the surface during the test. The resulting graph of the terminal dropsize distribution is shown in Figure 4.18. The abscissa is presented in binned increment units of 5.0 microns with the center of each bin (or interval) at 2.5, 7.5, ...27.5 microns etc..
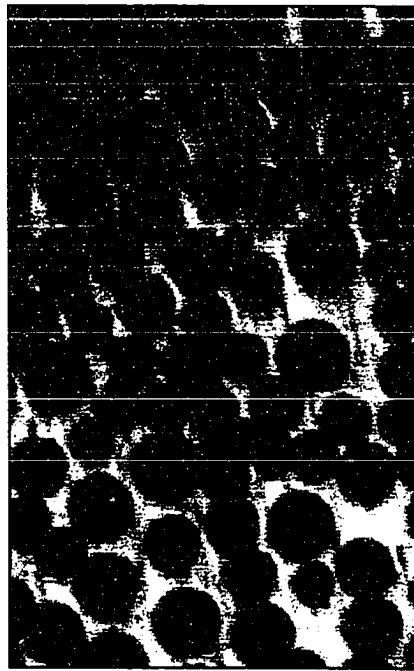
Figure 4.17. Terminal dropsize image on uncoated, polished copper surface (run D1114011).
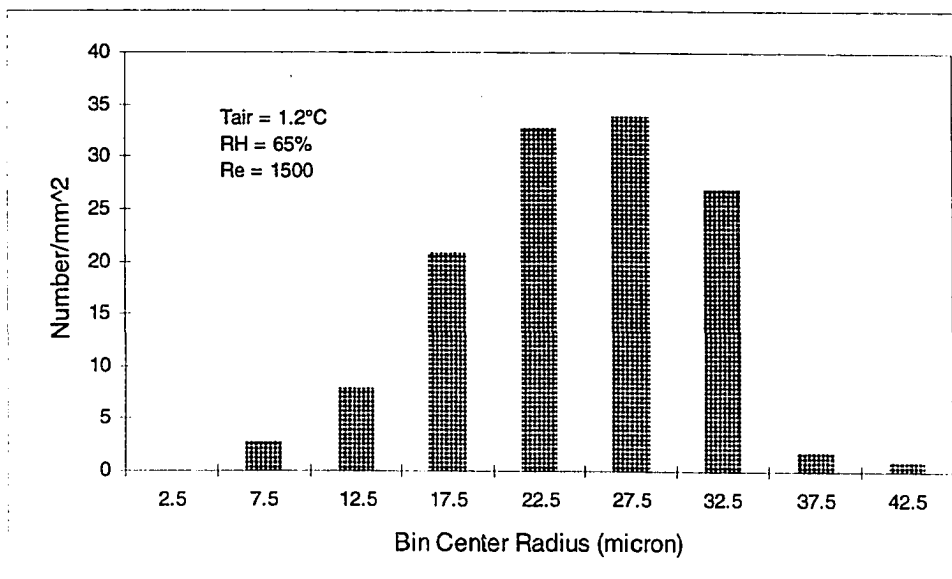
Figure 4.18. Dropsize distribution for image shown in Figure 4.17.

The maximum number of droplets per mm^2 occurred at the bin size of 27.5 microns ($\pm$ 2.5 micron). That is, for droplets in the radius range of 25 - 30 μm one could expect to find about 35 droplets per square millimeter. This image and the distribution data represented a snapshot in a continuous condensation process. This image was the last in a series of images that were taken during one of the experimental runs. The complete series consisted of eight images, one taken every minute until the droplets in the field of view for this section began to nucleate to ice. The first minute image was not included because it was an extremely poor image and could not be analyzed with the imaging software. This series is shown in Figure 4.19. The images were taken at a magnification of approximately 150x.
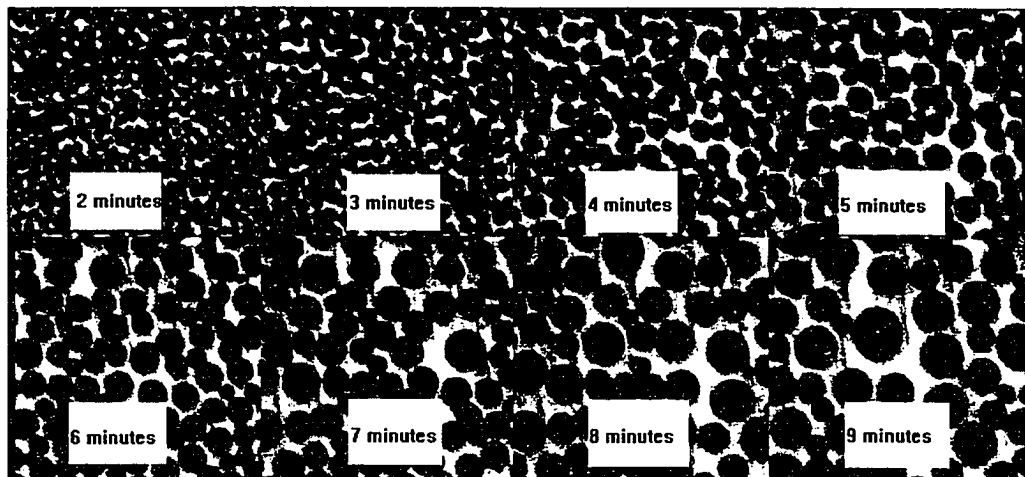
Figure 4.19. Time series for condensation on polished uncoated copper plate (run D111401, T_g = 1.2° C, T_w = -10.0° C, RH = 65%, Re ≈ 1500).

The growth of the dropsize distribution for the droplets is evident in this series of images. Figure 4.20 is a log-log plot of the time series dropsize distribution for the images shown in Figure 4.19. The continuous lines were added as a guide to the eye to differentiate the

time steps. The information for the 9 minute series is the same as the bar graph shown in Figure 4.18. For this particular series, note the decreasing peaks for each succeeding time step and the broadening of the distribution of sizes. In addition, a sense of scale for Figure 4.19 is obtained from Figure 4.20. The peaks of each time series correspond to the mean cluster, or droplet, size for that time series. Thus, for the two minute image shown in Figure 4.19, the droplet sizes ranged from 2.5 to 12.5 μm in radius and had a mean size of approximately 7.0 μm.
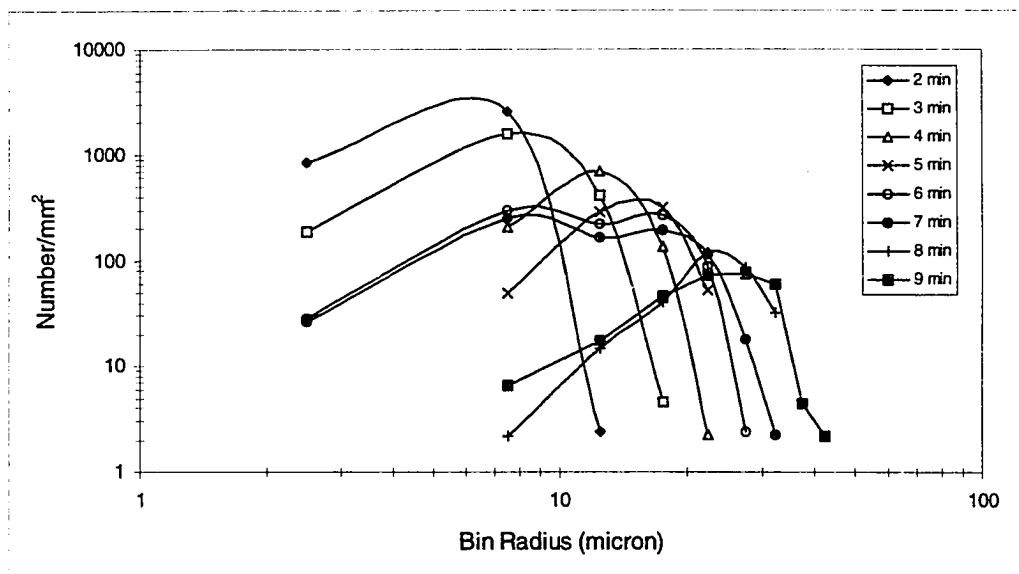
Figure 4.20. Time series of dropsize distributions for condensation on copper plate at $T_g = 1.6°$ C, RH = 65%, and Re $\approx$ 1500.

The broadening of the size distribution was the simple result of the droplets growing through direct condensation and by coalescing with other droplets. At the 6th and 7th minutes, a slight dip was noticed at the 12.5 bin radius size. This was the result of larger droplets coalescing and smaller droplets renucleating in the bare areas that were exposed.

For comparison, Figure 4.21 shows the terminal dropsize distribution on uncoated copper at an air temperature of 1.5° C, RH = 85%, and Re ≈ 1600.
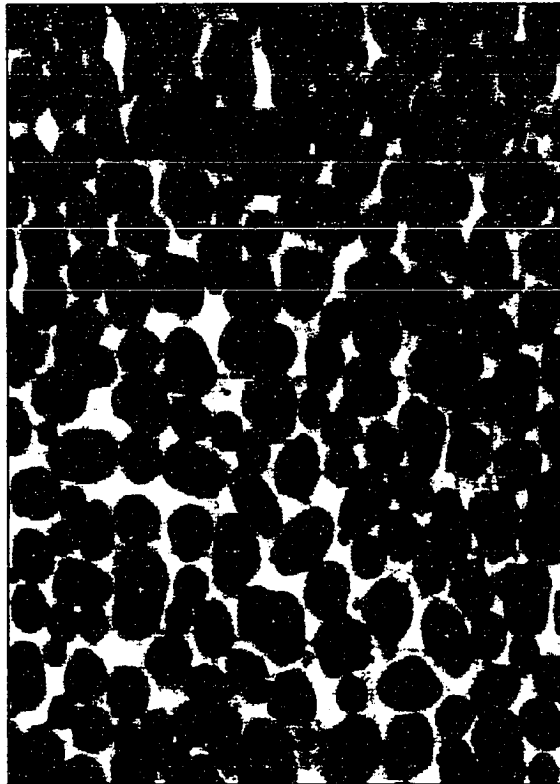
Figure 4.21. Terminal dropsize distribution on uncoated, polished copper plate (run T102810D, T_g = 1.5° C, RH = 85%, and Re ≈ 1600).

This image had considerably more irregularly shaped droplets, and the droplets were larger. The droplet series for this experimental run only went for approximately four minutes before ice nucleation began versus approximately nine minutes for the images shown previously in Figure 4.17. The primary difference between the two series was the level of moisture in the bulk air stream. Also, this surface had just been cleaned and did not have any organic residue or build-up of oxide. The difference in humidity ratios

(ΔW) which was the driving potential for mass transfer was much larger for the run

shown in Figure 4.21. The importance of the level of moisture to the condensing surface

was shown through the statistical treatment presented earlier. The complete four image

time series terminating in the image in Figure 4.21 is shown in Figure 4.22.
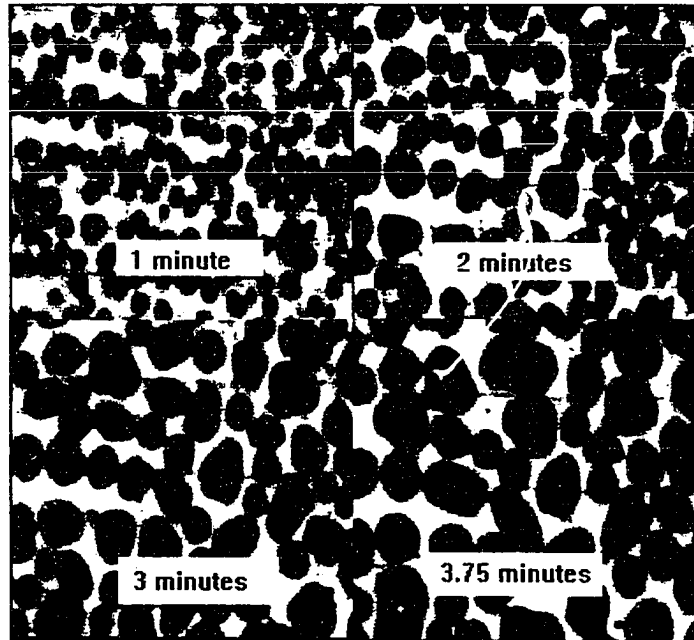
Figure 4.22. Time series for condensation on polished uncoated copper plate (run
T102810D, $T_g = 1.5°$ C, RH $= 85\%$, and Re ≈ 1600).

Figure 4.23 is a log-log plot of the time series droplet surface density for the images

shown in Figure 4.22. As in Figure 4.20, the continuous curves were added as a guide to

delineate the series. As in the previous time series, there was a general broadening of the

distributions and a shift in the peak radius for each succeeding time step. Considering the

droplet surface density it is seen that the second series had, in general, fewer droplets per

each time step but the droplets were larger. Referring back to the statistical data, it was

found that the experimental runs at higher relative humidities, in general, generated

higher mass fluxes to the surface and had much shorter times to the ice nucleation point..
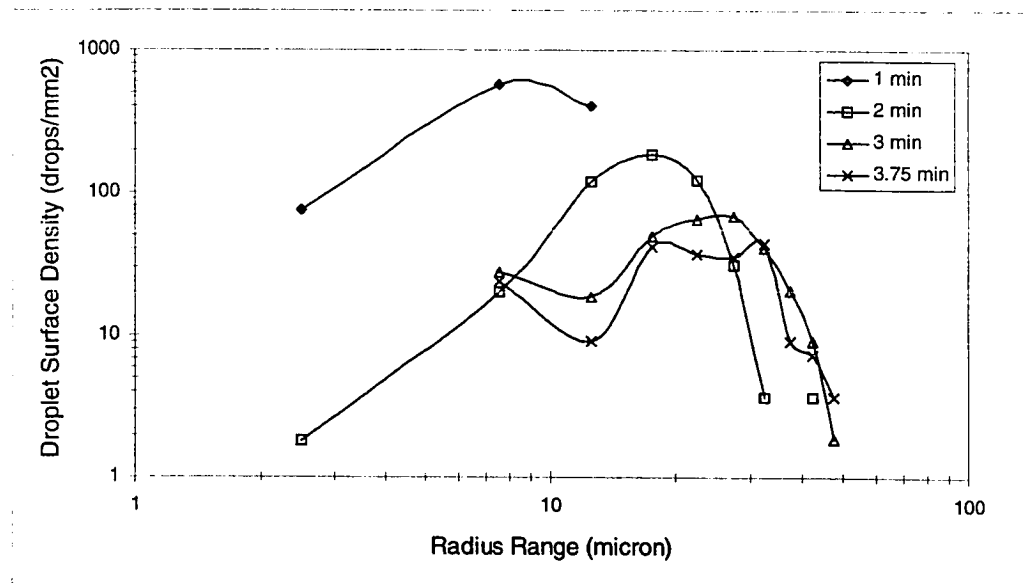
Figure 4.23. Time series of dropsize distributions for condensation on polished uncoated
copper plate (T_g = 1.2° C, RH = 85%, and Re ≈ 1500).

The data taken on the polished, coated copper plates were usually much different than the

data for uncoated runs in both heat transfer and droplets. Figure 4.24 shows the time

series of images for condensation on a polished copper plate coated with the silicone

conformal polymer. Note the rapid growth of the droplets between frames compared to

the images in Figure 4.19. The rapid growth rate ensured an image of adequate quality at

the first minute. The resolving power of the optical system allowed resolution of droplets

down to approximately five micron in diameter. So, the growth of droplets under the

conditions of that run was such that droplets of five micron and larger were discernible in

the first minute. Conversely, the experimental conditions of image of Figure 4.19 did not

allow adequate imaging until the 2nd minute, and even that image was marginal. Additionally, the dropsizes were much larger in a much shorter time span than for runs at lower temperature and lower relative humidity. Figure 4.25 is a log-log plot of the droplet surface density for the images of Figure 4.24.
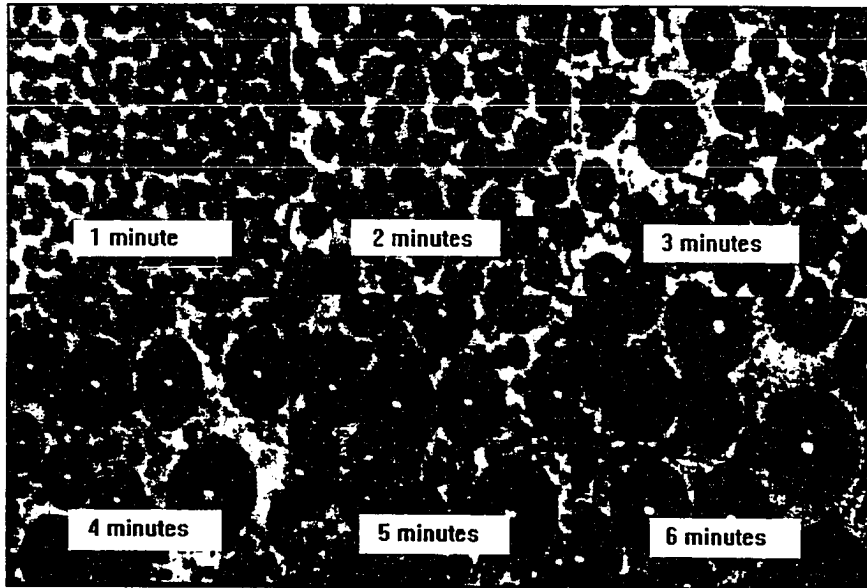
Figure 4.24. Time series for condensation on polished silicone coated copper plate (run D102806, $T_g = 7.0°$ C, RH = 85%, Re $\approx$ 1600).

Compared to the droplet surface density for the images shown in Figure 4.23, this image shows a much larger range of droplet sizes and distribution. For droplet radii larger than approximately 30 microns, all of the series began to merge and interpretation became difficult.
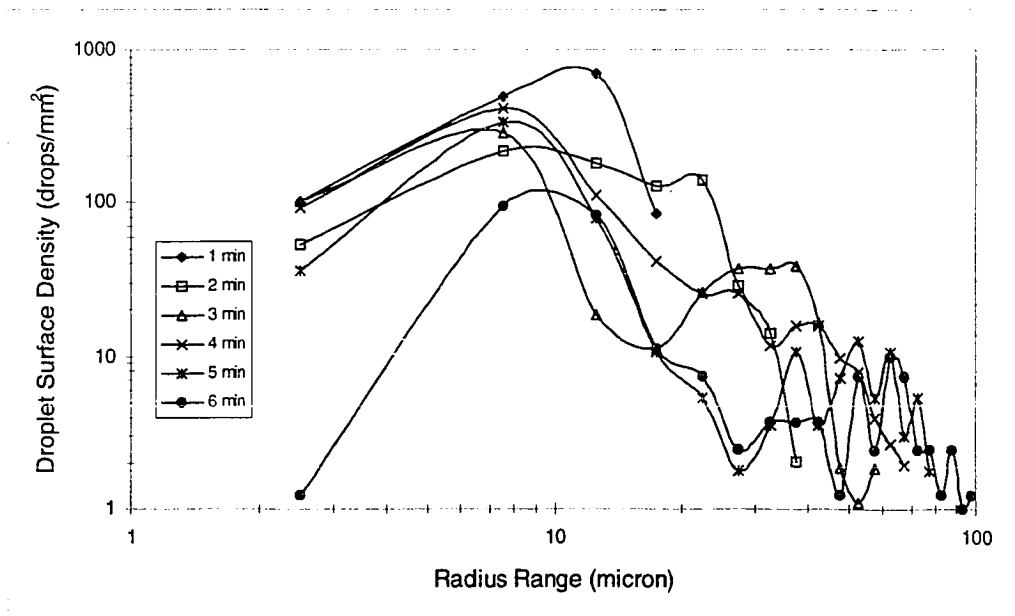
Figure 4.25. Time series of dropsize distributions for condensation on polished, silicone coated copper plate at $T_g = 7.0°$ C, RH = 85%, and Re $\approx$ 1500.

It became clear that the data had to be presented in a different manner to allow interpretation and understanding. The form chosen had to convey image information to the viewer in a concise fashion with little or no loss in meaning. This is always a delicate balance, but the following form seemed to meet both requirements. It was noted when graphing the distributions that besides the overall trend of "broadening and flattening", there was another rather striking feature of these data. If one plots the locus of points corresponding to the mean cluster size (Family and Meakin, 1988) at which the maximum mass of condensate is concentrated, a straight line fits the results through the peaks of the droplet surface density curves. This technique is demonstrated with the data that was shown in Figure 4.20.

The data for that series were reduced to determine at what mean cluster size the maximum droplet volume occurred. The corresponding droplet surface density was then identified. The resulting plots are shown in Figure 4.26.
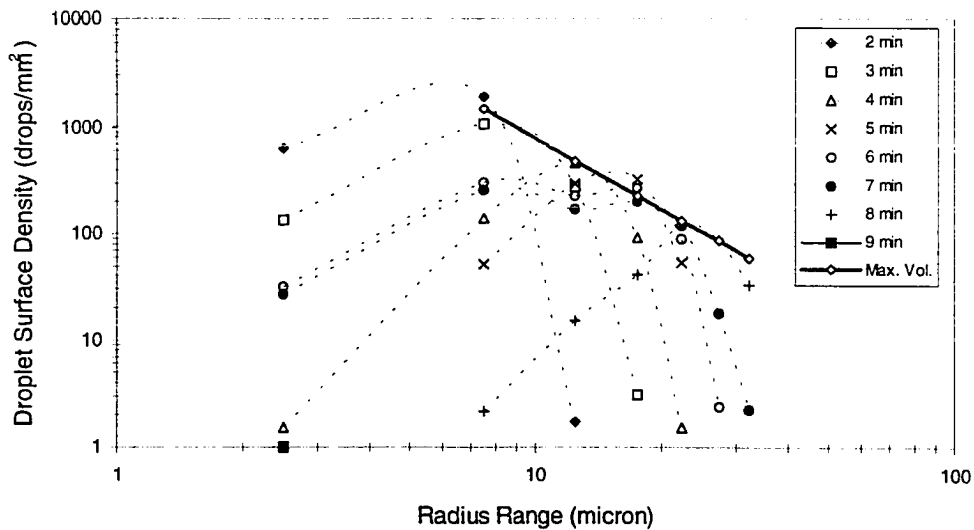
Figure 4.26. Time series data for D111401 with maximum volume locus (T_g = 1.2° C, T_w = -10.0° C, RH = 65%, Re ≈ 1500).

The straight line shown in Figure 4.26 is a linear regression through the data for the maximum surface density points. The regression coefficient for these data was 0.92 which indicated that the straight line was a very good fit for the data. The facility of the technique now became apparent, in that two different time series could be compared directly and the results compared graphically.

Not all of the experiments performed for this study were recorded on one minute intervals. The majority of the data were taken as quasi-steady state condensation runs with only the terminal (start of ice nucleation) image stored for later reduction. Using the

maximum volume method on the time series that were taken, it was found that the terminal distributions were all similar in that the maximum volume occurred at a radius range that was in the "right-end" of the droplet distribution. This is shown for the data of Figure 4.25 as it was for Figure 4.20. Note in Figure 4.27 that the slope of the locus of maximums is very similar to the slope of the regression line in Figure 4.26. Though the slope of the regression lines was similar, the lines were definitely displaced relative to both the radius range and the droplet surface density. Now that the mechanics of the method have been described, Figure 4.28 shows the results for these two time series.
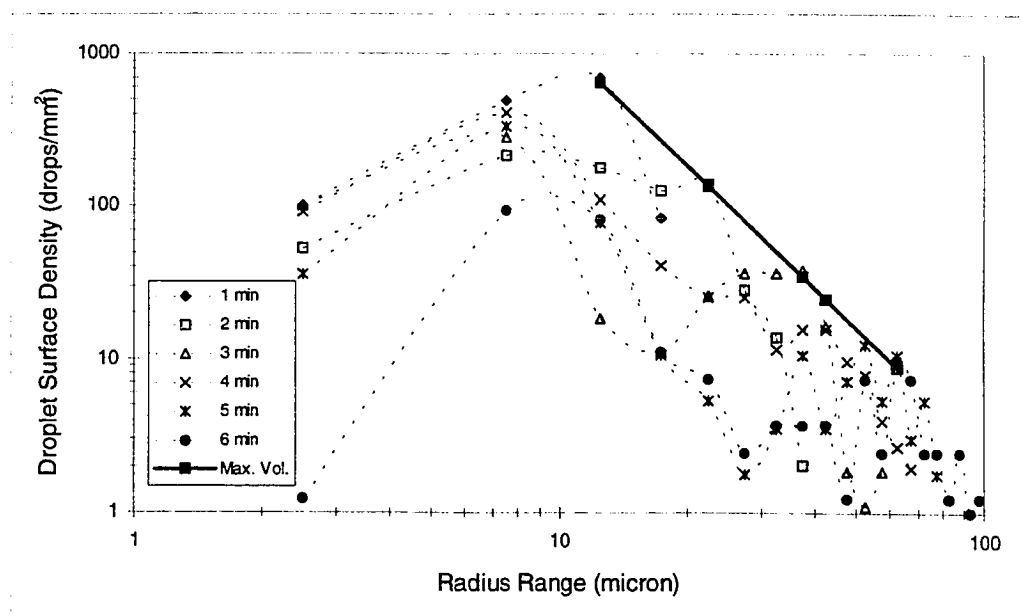
Figure 4.27. Time series data for run D102806 with maximum volume locus (T_g = 7.0°C, RH = 85%, Re ≈ 1600).

There was a difference in slope and offset for the two series. The graph could be interpreted in the following manner; the uncoated copper condensation tests resulted in a more narrow distribution of droplet sizes and terminated at a smaller radius range than

did the coated copper series. Additionally, the uncoated copper radii didn't change as quickly during the condensation process as did the silicone coated copper.
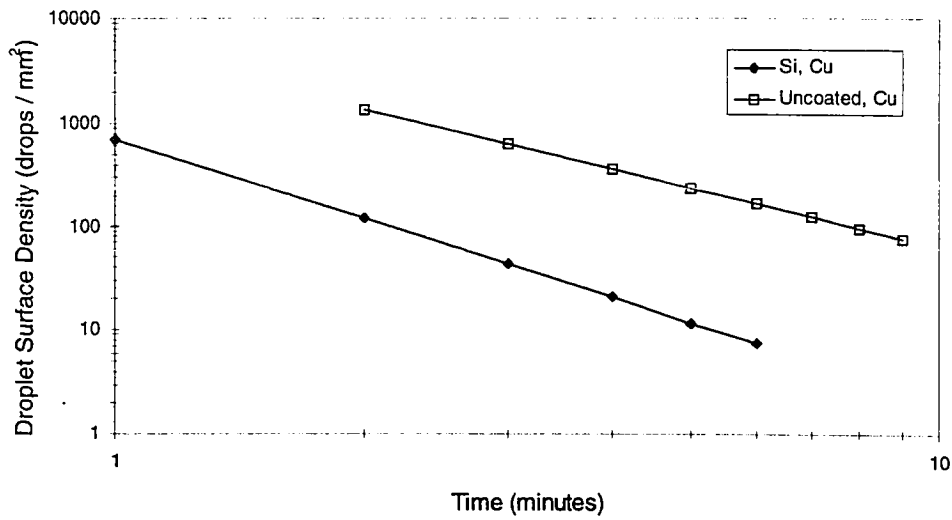
Figure 4.28. Condensation time series data for silicone coated and uncoated copper plate.

CHAPTER V

MODELING OF THE DROPWISE CONDENSATION PROCESS

The condensation of water vapor from an air stream onto a cold surface occurs as a deceptively simple process. Water condensing on a cold beverage can or glass of iced tea in the summer is a familiar process. However, as with most processes in nature, condensation is a very complex interaction involving simultaneous heat and mass transfer. The solid's surface energy and the liquid droplet contact angle are extensive properties that also play important roles in this process. No single comprehensive theory appeared to completely describe this phenomenon. The modeling effort for the present study concentrated on the nucleation, growth and terminal size distribution for droplets undergoing condensation from the surrounding air stream.

Background

Several researchers have developed numerical models to describe the steam condensation process (refer to Chapter II). Some of the models were based on geometry (Gose, et al., 1967), while others included heat transfer effects on the droplet growth (Glicksman and Hunt, 1972). For these models, the primary limitation was usually computing power. It has been well established that the nucleation site density for dropwise steam condensation was on the order of 10^8 sites per square centimeter (Cary, 1992). It was equally well established (Collier, 1972) that the primary benefit to dropwise condensation in steam systems was the tremendous improvement in overall heat transfer, often four to eight times that for filmwise condensation.

Most of the steam modeling efforts have been concerned with determining the effect on heat transfer of the nucleation site density, droplet growth rates, and non-

condensable gases. Dropsize distribution usually was not the subject of attention. Though important, the dropsize distribution information was one of the results of the model that led to heat transfer analysis. For this study, the dropsize distribution was important for two primary reasons. First, the distribution of sizes at the time that the liquid droplets begin to nucleate to ice determined the initial conditions for the subsequent growth of the frost layer. Tao and Besant (1992) have developed a frost model that they termed the "unit cell" method. This model for frost growth on a heat exchanger surface required that the distribution of frozen droplet embryos be known a priori. They noted that this distribution must be assumed because there were no methods available to predict what the distribution should be. Secondly, the mass of liquid water, which ultimately turned to ice, contributed to the total mass of the frost matrix as the frosting process progressed. Again, most researchers have either assumed that this initial liquid mass was negligible or they have had to assume some values based on experimental results.

The model developed for the present work was constructed using the best of the methods from the various researchers as described in Chapter II. The geometric simplicity of the Gose et al., (1967) study was combined with the analytical developments from Umur and Griffith (1965). As noted in the literature review, there were large differences in the value for the condensation coefficient for steam condensation versus "normal" condensation. Normal condensation would be described as the condensation of water vapor from an air stream at atmospheric pressure and at temperatures and moisture levels found in common psychrometric processes. The model construction consisted of two rather distinct parts; building the computer simulation of the physical condensation process, and the analytical portion that described the droplet growth under various conditions. The condensation simulation is described first followed by the model for the

droplet growth and the combination of the two components. Results of the model and effects of various parameters such as contact angle and initial site density are then presented.

Computer Simulation

A program (initially written in QuickBasic®) was written to simulate the nucleation and condensation process on a flat horizontal surface. Droplets were not allowed to grow to a size that would cause them to move from the surface. This is only important when modeling condensation *and* removal of droplets from a surface. For this model, the droplets nucleated to ice well before they could grow to a size large enough to cause movement.

A 700 x 700 grid was used as the active condensation area. This produced an area of 490,000 μm^2 which was approximately the same as the viewing area of the video-microscopy system used in the condensation experiments. This size also minimized edge effects. For small areas, droplets can "lose" volume because the center of the droplet is outside the edge of the viewing area and these droplets have fewer neighbors available to coalesce with. Larger areas minimize this problem.

At the beginning of the program, **n** number of droplets would be randomly deposited onto the grid. The timer in the computer clock provided the seed for the random number generator that provided the x and y coordinates for the center of mass for each droplet site on the grid. The next step consisted of checking sequentially from the first site to all surrounding sites for any droplets that were close enough to coalesce with. If a coalescence occurred, the droplet was grown to its new dimension and the check was started again to make sure that no additional droplets were in contact with the new

droplet. The coalescence criteria was based on the distance between droplet centers. This distance was calculated using the following equation

$$Dist = \left[\left(x_j - x_k\right)^2 + \left(y_j - y_k\right)^2\right]^{\frac{1}{2}}$$ 5.1

$$j = 1, 2, \ldots \mathbf{n}$$

$$k = j + 1, j + 2, \ldots \mathbf{n} + 1$$

If *Dist* was less than $0.95(R_j + R_k)$, then the drops were coalesced and the search for any other coalescences begun again. The factor of 0.95 was chosen to allow the droplets to just slightly "indent" into each other before combining. This mimicked the behavior of microscopic droplets as seen during condensation experiments. Once the droplets were allowed to condense, the new droplet radius was found by

$$R_{new} = \left(R_j^3 + R_k^3\right)^{\frac{1}{3}}$$ 5.2

This was the radius for a new droplet based on a contact angle of 90°. That is, if the droplets were assumed to be hemispheres. Strictly speaking, if the effect of the contact angle on the radius were to be included in the coalescence of the two droplets, equation 5.2 would be modified to:

$$R_{new} = \left[\left(R_j + R_k\right)\left(R_j^2 - R_j R_k + R_k^2\right)\right]^{\frac{1}{3}}$$ 5.3

Equation 5.3 describes the radius of curvature for a newly coalesced droplet. Figure 5.1 shows a droplet with a high contact angle resting on a flat surface. From this figure, it is seen that the contact dimension, $D_{contact}$, can be significantly different than the radius of curvature, R_{new}, for a droplet with a large contact angle. $D_{contact}$ is equal to $2R_c$ at contact angles of 90°.
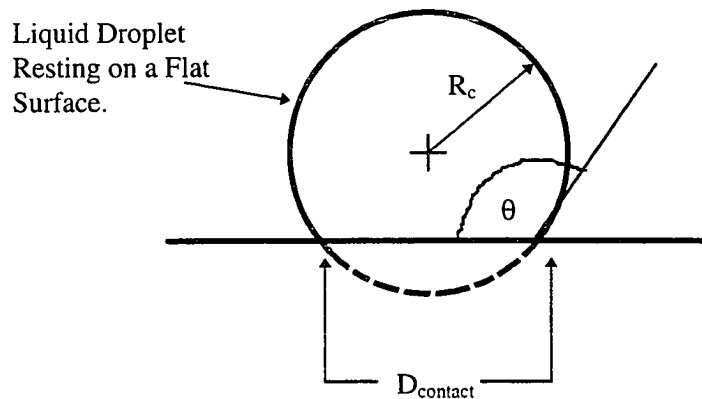
Figure 5.1. Droplet with high contact angle.

However, for contact angles ranging from 80° to 110°, which was the range of interest for this study, the effect of the contact angle on the surface contact dimension only varied by approximately 6%. Conversely, the volume of the droplet changed almost 50% over that same range. For such a small effect on surface contact, the use of equation 5.2 was justified. When the droplets coalesced, the kth droplet radius was set zero, and the search for further coalescences then continued.

From observations of the coalescing process during condensation experiments, it was found that when a smaller droplet combined with a larger droplet, it was always at the expense of the smaller droplet. That is, the smaller droplet was always drawn completely into the larger droplet. This follows from the fact that the internal pressure for smaller diameter droplets is higher than for larger diameter droplets (Cary, 1992). Thus, when the droplets' "skin" ruptures upon contact, the higher pressure in the smaller droplet forces the contents of the smaller droplet to move to the lower pressure region in the larger droplet. To account for this phenomena, logic was included in the program that checked for the larger of two touching droplets and upon coalescing, the smaller droplet would be combined with the larger droplet and the new, larger droplet would remain at

the coordinates of the original large droplet. The program then continued checking all sites for further coalescing.

Once the logic of the main program was debugged and verified, several runs were performed on a 80486-DX50 PC. With the QuickBasic code, an eight minute simulation with an initial droplet population of 2,000 droplets took approximately eight hours. It was evident that a much faster version of the program was necessary before it would be very useful. The QuickBasic code was rewritten in C++ and the computational time was reduced to approximately 5 minutes. A flowchart of the program logic is shown in Figure 5.2.

After numerous runs with the program, it became clear that the most important element in the simulation was the rate of droplet growth for each time step. Several analytical treatments for the rate of droplet growth were found in both the steam and atmospheric sciences literature. Umur and Griffith (1965) developed the form given in equation 2.14 for the droplet radial growth rate for dropwise steam condensation. McCormick and Westwater (1966) expressed the growth rate as given in equation 2.15. Gose, et al., (1967) developed the following equation for the growth rate

$$\frac{dr}{dt} = 2.075\frac{k_l\left(T_d - T_w\right)}{i_{fg}\,\rho_l} \qquad\qquad 5.4$$

Forms for the droplet growth rate from the atmospheric sciences are usually given when describing droplet growth in cloud structures. There are some similarities with the present problem, but the heat transfer process is decidedly different as is the geometry. In cloud droplets, the heat released during condensation has to be diffused back into the surroundings as opposed to into a cold heat exchanger surface. In addition, the droplets are always assumed to be spherical in shape.
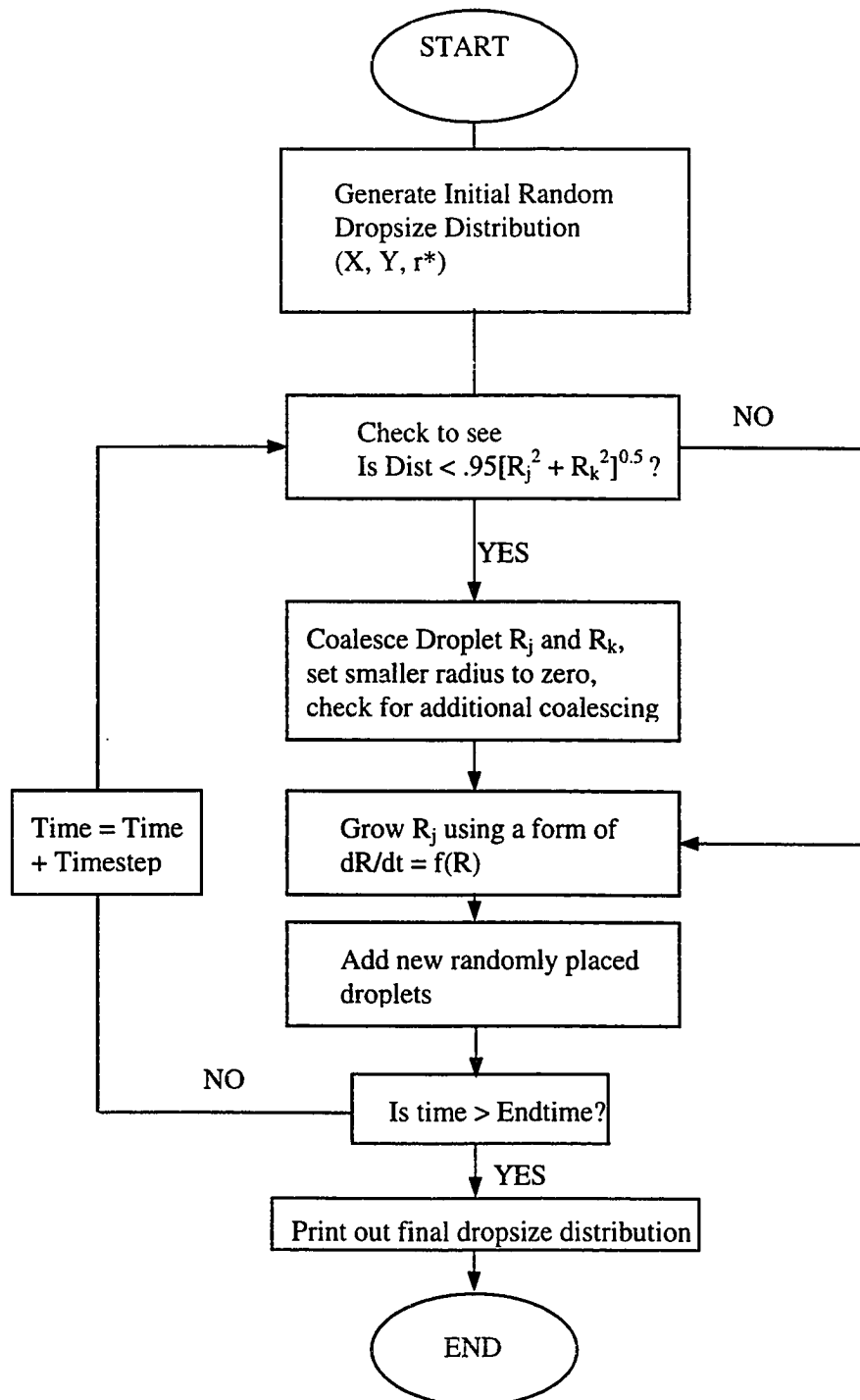
Figure 5.2. Logic flowchart for C++ condensation simulation.

An example of an atmospheric droplet growth equation is given by Chodes, et al., (1974):

$$\frac{dr}{dt} = \frac{(S-C)}{r^2} \left[\frac{i_{fg}^2 \, \rho_l}{k_g \overline{R}_g T_g^2} + \frac{\rho_l}{\rho_g D} \left(\frac{r + \left(\frac{2\pi}{R_g T_g}\right)^{1/2} \left(\frac{D}{\alpha}\right)}{r} \right) \right]^{-1} \qquad 5.5$$

where S is the supersaturation level for the cloud. This equation took into account the vapor and temperature fields surrounding a spherical droplet. Chodes used equation 5.5 to determine the condensation coefficient for droplet growth in clouds.

Using any of the above equations or variants of them produced droplet growth rates that were orders of magnitude too large when compared to the experimental droplet growth. It was decided to use a combination of the results from both fields of study to develop an expression for the droplet growth rate for this study. Referring back to the work done by Umur and Griffith (1965), they had developed a general expression for the condensation rate w on a drop with a radius of curvature r given by

$$w = \left(\frac{2\alpha}{2-\alpha}\right)\left(\frac{g}{2\pi \overline{R}_g}\right)^{1/2} \frac{P_g}{T_g^{0.5}} \left[1 - \frac{P_i^*}{P_g} e^{\frac{2\sigma v_l}{r \overline{R} T_i}} \right] \qquad 5.6$$

This general form was then simplified for the condition of a saturated vapor (shown in equation 2.11), which was not the case for the present model. Keeping the general form of equation 5.6, the interfacial heat transfer coefficient was then expressed as

$$h_i = \frac{w i_{fg}}{T_g - T_i} \qquad 5.7$$

Umur and Griffith presented the final simplified form of the interfacial heat transfer coefficient as given in equation 2.12. The primary result of their simplification was the

elimination of T_i in equations 5.6 and 5.7. The temperature T_i, is not an easily obtained

extensive measurement in most condensing systems. Figure 5.3 was taken from

Minkowycz and Sparrow (1966) and showed the relative magnitudes of the temperature

profiles in a condensing system. The majority of the temperature drop occurred through

the mixed air-water vapor region. This emphasized the role of diffusional resistance in

the boundary layer. This resistance was a result of the accumulation of noncondensable
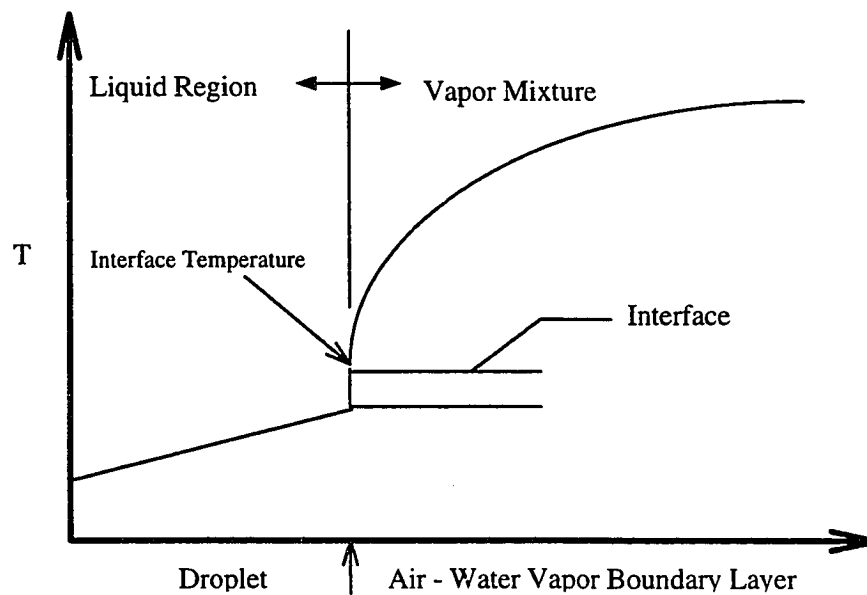
gases in the boundary layer

Figure 5.3. Temperature profiles at the boundary layer for condensation in the presence of non-condensable gases.

When used, this temperature was *always* either estimated or approximated by another

convenient temperature. The conditions for the present model suggested a convenient

estimate of the interface temperature.

The liquid droplet resting on the cold surface does have a temperature distribution through it, but relative to the temperature distribution through the vapor above the droplet, it is very small. Thus, it may be assumed that the droplet temperature is approximately equal to the surface temperature. Now, net condensation cannot occur unless the temperature at the surface is below the saturation or dew point temperature. So, a first approximation to the interface temperature T_i is defined as

$$T_i = \frac{T_{sat} + T_w}{2}$$

and

$$T_R \geq T_{sat} \geq T_i \geq T_w$$

5.8

This is a convenient definition since all of the temperatures are known a priori or can easily be estimated for given conditions.

Next, as discussed in the literature review, the condensation coefficient still seemed to be the subject of debate. A value of approximately 0.45 was most often found in the steam literature. Several experimental studies have determined this value of the condensation coefficient for the condensation of pure, saturated steam with no non-condensable gases present (Maa, 1983). Similarly, cloud chamber experiments have shown a value of approximately 0.034 for the condensation of water vapor under normal atmospheric conditions in clouds (Chodes, et al., 1974). Equation 2.24 (Okuyama and Zung, 1967) allowed the condensation coefficient to vary with the radius of the condensing droplet. Both fields of study acknowledged that the condensation coefficient is a convenient parameter to manipulate in a model so that good agreement can be made with experimental data. A coefficient value of 0.034 was used for the initial evaluation with the present model since this value consistently appeared in the atmospheric condensation literature and that condensation process closely paralleled the current work.

Maa (1983) started with the expression for the droplet growth rate given by Umur and Griffith (1965) and derived the following equation for the droplet growth rate

$$\frac{dr}{dt} = \frac{T_{sat} - T_w}{\rho_l i_{fg}} \left(\frac{1 - \dfrac{r^*}{r}}{\dfrac{1}{2k_l} + \dfrac{1}{h_i}} \right)$$

5.9

The critical radius r^* was given by Cary (1992) as

$$r^* = \frac{2\sigma T_w}{i_{fg} \rho_l \left(T_s - T_w\right)}$$

2.28

Equations 5.6, 7, 8, and 2.28 form the core of equations needed to determine the droplet radius as a function of time and the rate of droplet radius change with time as a function of droplet size. These equations were used to build an Engineering Equation Solver (EES®) worksheet. EES has all of the psychrometric relations and thermodynamic data for air/water systems built into it's program. Appendix II shows a printout of the EES worksheet for the droplet growth model.

Results of the Droplet Growth Model

The EES portion of the model addressed only the droplet growth portion of the overall condensation model. Still, this growth was *the* critical element in the condensation model. The droplet growth rate determined from the very start of the simulation what the terminal distribution would be. If the rate was too slow then, for given ambient conditions, the terminal droplets would be too small and spaced too far apart (relative to experimental data). Conversely, if the rate was too high, the droplet distribution rapidly evolved to just a few very large droplets.

Figure 5.4 shows the droplet growth rate as a function of the droplet radius for the conditions shown. The rate of droplet growth changed rapidly as a function of radius especially for droplets less than approximately ten microns in radius. As air temperature increased the rate of initial droplet growth also increased. All temperatures show that the growth rate became asymptotic after the droplet radius reached approximately ten microns. The differing starting radii for the various temperatures was because the critical radius changed relative to the air temperature. The starting radius for the model was taken as two times the critical radius. Values of 1.5 (Glicksman and Hunt, 1972) and 3.0 (Umur and Griffith, 1965) have been used for steam condensation models. The reasoning was that a droplet embryo at the critical radius is just stable. Droplets smaller tended to disappear spontaneously, whereas larger droplets may continue to grow. For the temperatures of 1.5°, 3.5°, 5.5°, and 7.5° C the critical radii were 0.48 μm, 0.35 μm, 0.25 μm, and 0.19 μm respectively. As seen in equations 2.25 - 28, as the temperature difference between the air and the wall increases (subcooling) the critical radius has to become smaller. Increasing growth rate with temperature also follows from equation 2.14. The temperature difference between the air and surface was the primary driving potential for growth.
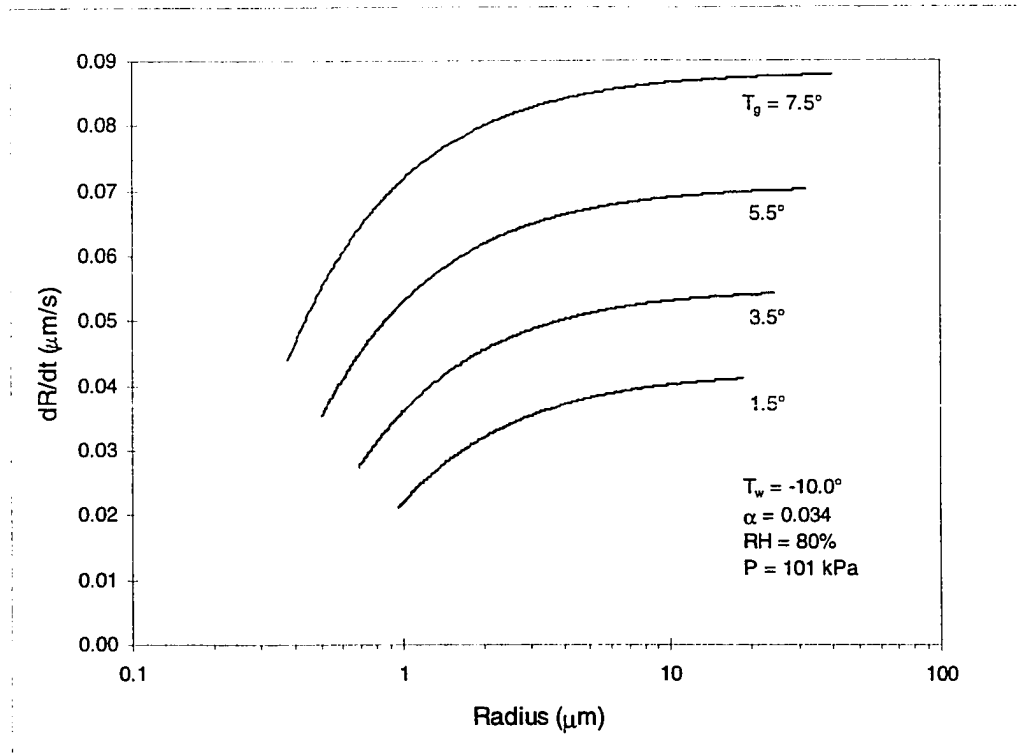
Figure 5.4. Droplet growth rate as a function of droplet radius for various air
temperatures.

Figure 5.5 shows the effect of varying atmospheric pressure on the droplet growth

rate. Even though the ambient pressure term was present in equation 5.6, it had a very

weak influence on the condensation process in the range of pressures normally

encountered in psychrometric processes. The three pressures shown in Figure 5.5 are 98,

101, and 105 kPa (standard atmospheric pressure is 101 kPa).
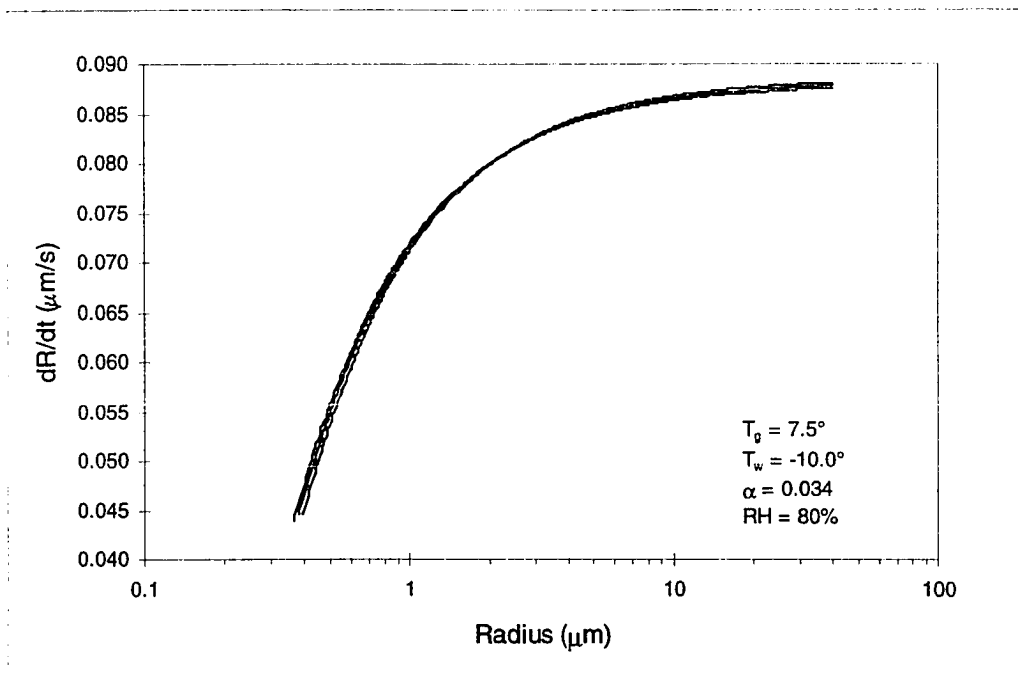
Figure 5.5. Droplet growth rate as a function of droplet radius for various ambient air pressures.

The effect of varying plate temperatures is shown in Figure 5.6. As with increasing air temperature (Figure 5.4), decreasing plate temperature, at a fixed air temperature, leads to a larger driving potential for droplet growth. Here, the initial growth rates increased rapidly then started to become asymptotic at radii of approximately six microns. The growth rate at a plate temperature of 0.0° C was very nearly constant at a value of about 0.02 μm/s and as the plate temperature approached the air temperature the growth rate would continue to decrease. For this study, the plate temperature was held at -10.0° C for all experimental runs. At higher plate temperatures, it was found that the droplets would not freeze or would take hours before beginning to freeze. At temperatures less than -10.0° C, the condensed droplets would freeze in such

short times, especially at high air temperature and relative humidity, that few heat transfer data or images could be acquired.
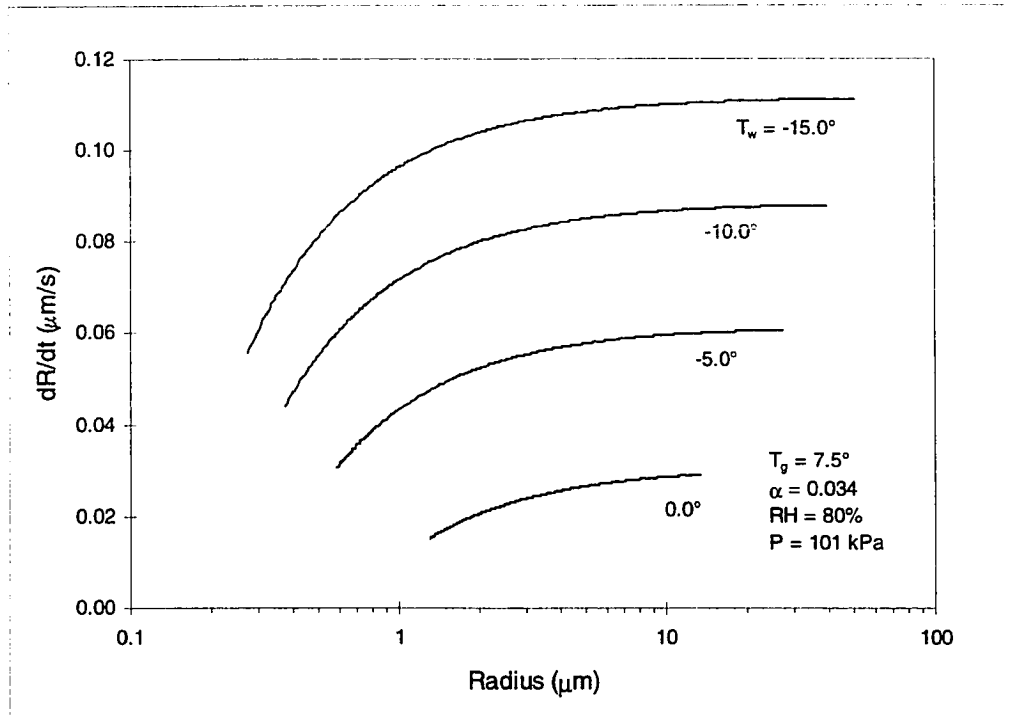
Figure 5.6. Droplet growth rate as a function of droplet radius for several plate temperatures.

Figure 5.7 shows the effect of different values for the condensation coefficient on the rate of droplet growth. Three of the values for α were constant and one varied with the radius of the droplet. Values of one for the condensation coefficient were often used when evaluating other factors in droplet growth. As seen in this figure, when $\alpha = 1.0$, there was a very rapid rise in the growth rate and the rate stayed at a high level. This translated into very rapid droplet growth in the early stages of condensation which continued during the later stages when direct growth should not be the dominant growth

mechanism. In the late stages of droplet growth, coalescence with other droplets had

been shown to be the primary means of droplet growth (McCormick and Westwater,

1966). A value of 0.45 for the condensation coefficient was often used in the steam

literature. Tanaka and Hatamiya (1986) determined this value from experiments with low

pressure condensation of saturated steam that had been thoroughly purged of

noncondensables. As with $\alpha = 1.0$ this value had an initial rapid rate change

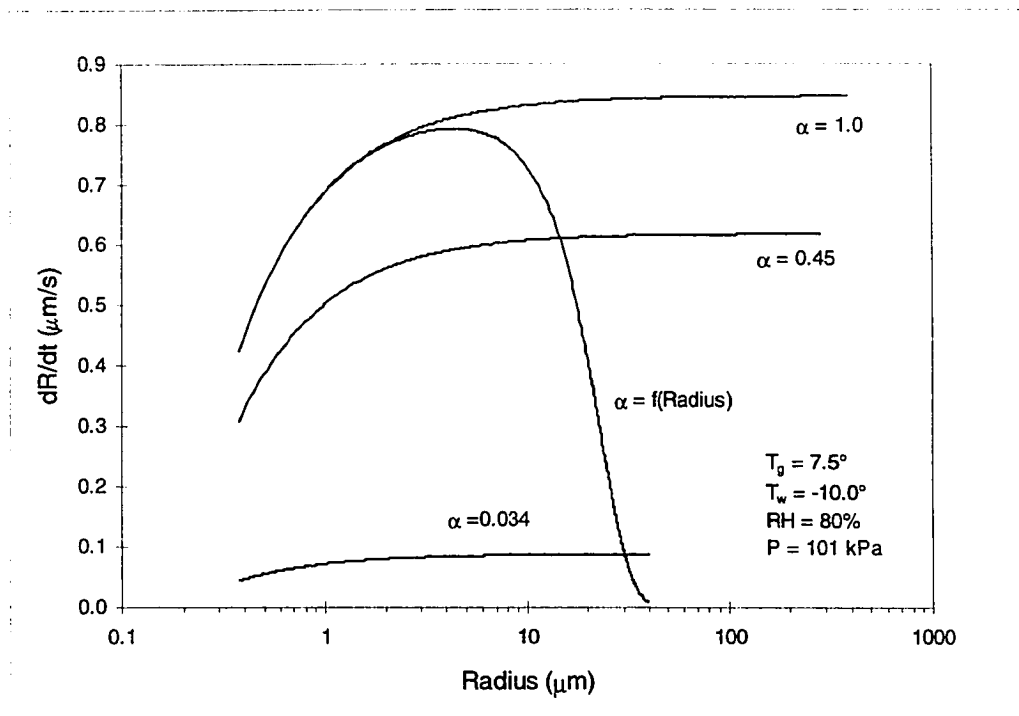

Figure 5.7. Droplet growth rate as a function of droplet radius for various values of the condensation coefficient.

until a radius of approximately ten microns. For a five minute simulation at the

conditions shown in Figure 5.7, these values of the condensation coefficient led to

terminal droplet radii of over 250 microns. These values for the radii were almost a

factor of five greater than radii found under similar experimental conditions. Both values, especially $\alpha = 1.0$, intimated that the majority of the vapor particles that strike the surface were converted into the liquid phase. For perfect saturated vapor conditions this may be approached, but for atmospheric condensation where the mass fraction of noncondensable gases are much greater than the fraction of water vapor, the conversion to the liquid phase is not as efficient.

This introduces the curve representing the condensation coefficient as a function of the droplet radius. The equation describing this relationship was given in Chapter II (eqn. 2.24). Here, the value for δ, the rotation partition function, was taken as equal to one. From a physical standpoint, this form of the condensation coefficient was very satisfying. It allowed for the rapid growth of the droplets but then rapidly fell off as the droplet radius increased. This paralleled the growth history of an individual droplet. Unfortunately, like the previous higher values for α, this function led to droplets that were too large compared to experimental values. This was because the initial rate of growth was very similar for the function at $\alpha = 1.0$ and this caused the initial population of droplets to grow much faster than actually occurred.

Finally, the value for $\alpha = 0.034$ showed a very slow initial increase in the droplet growth rate and rapidly became asymptotic at a relatively low value of about $0.1 \ \mu m/s$ for droplet radii greater than one micron. This value of the condensation coefficient was taken from the atmospheric literature where its value seemed to be well accepted (Hagen, et al., 1989). This value appeared to account for the noncondensable gases present in these type condensation processes and allowed only moderate (relative to the other values of α) growth of a droplet. For simulations using this value of α, the terminal droplet radii showed good agreement with those found from experimental data.

Figure 5.8 gives the effect of different levels of ambient relative humidity on the droplet growth rate. For the conditions listed, this figure is similar to Figures 5.4 and 5.6. As ambient humidity levels increased, the critical radius decreased and the rate of droplet growth increased rapidly through droplet radii of approximately three micron. As expected, at a very low level of relative humidity the droplet growth rate was the lowest and was approximately constant at 0.018 μm/s.
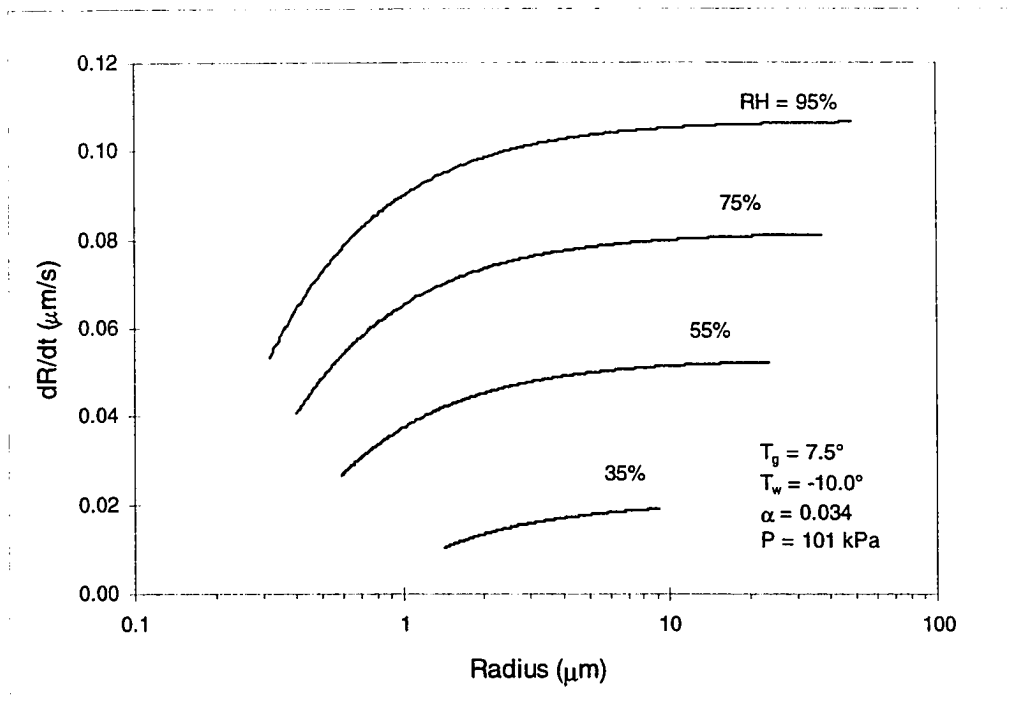

Figure 5.8. Droplet growth rate as a function of droplet radius for several levels of ambient air relative humidity.

This was so because the driving potential for mass transfer was the difference in density. The mass transfer rate for a process is often expressed as (ASHRAE, 1993)

$$\dot{m} = \bar{h}_m A \left(\rho_i - \rho_g \right) \qquad 5.9$$

where the density difference is evaluated at surface and air temperature respectively.The larger the density difference, the higher the mass flux across the interface onto the droplets. This agreed with droplet growth observed during experimental condensation runs.

The second portion of the model simulated the actual nucleation, growth, and coalescence of droplets over a specified time period. Variables that could be manipulated included the initial number of droplets, contact angle for the droplets on a given surface, and the droplet growth rate. Time steps of one second were found to be adequate. Total length of a given simulation was based on experimental observations for the total time from the start of the condensation process to the point when the liquid droplets nucleated to ice. This simulation program was executed on a Pentium class machine and depending on the simulation, a run would take from five minutes to approximately one hour. Several simulations were made with the model to estimate the effects of the above variables. Figure 5.9 shows the effect of the initial droplet population on the mass of liquid water that condensed onto the surface for the conditions of the simulation listed. The program took as an input the total number of droplets to be used as the initial droplet population. The radius of the droplets in the initial population was assumed to be twice the critical radius for the conditions of the simulation. This population of initial droplets was then assigned to random positions on a 700 x 700 micron grid. The complete logic and flow for the program was discussed earlier in this chapter. Initial droplet populations of 500, 1,000, 3,000, and 5,000 were each started on an eight minute condensation simulation. Normally, for a surface at -10.0° C, freezing would occur at some point in the condensation process.
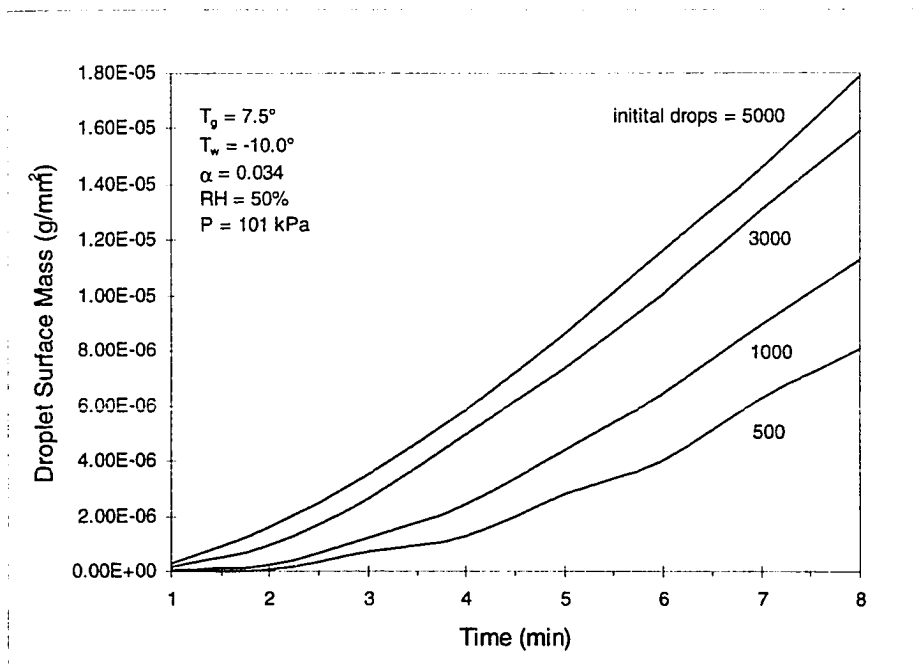
Figure 5.9. Effect of initial droplet population on total droplet surface mass accumulated during an eight minute simulation.

These simulations did not include this nucleation time. That is, the droplets would continue to grow as liquid droplets as long as the simulation was allowed to run.

Intuitively, it follows that if one starts with more droplets on the surface and the droplets can grow and combine, more mass will result on the surface. For initial populations of 3,000 and 5,000 droplets, the mass of water was approximately 1.6 and 1.8 grams/mm^2 respectively. There was a difference of approximately 10% between these two values. Comparing the 1,000 to the 3,000 droplet population however, the difference was almost 32%. This indicated that if the starting droplet population was approximately 3,500 or more, there would be little difference in the terminal masses.

Another way to appraise the effect of the initial droplet population is to consider the cumulative area covered by droplets during the simulation. This is shown in Figure

5.10. This figure shows that the starting populations of 3,000 and 5,000 droplets have reached approximately the same percentage of area covered by droplets of about 62%. In fact, the 5,000 droplet curve was asymptotic at this point. The two lesser populations were still at approximately 52% and 43% for 1,000 and 500 droplets respectively. The area coverage figure of approximately 60% was significant for the two higher populations because that was a percentage that frequently appeared in the steam literature (Tanaka, 1975, and Rose and Glicksman, 1973). This supported using starting droplet populations of at least 3,000.
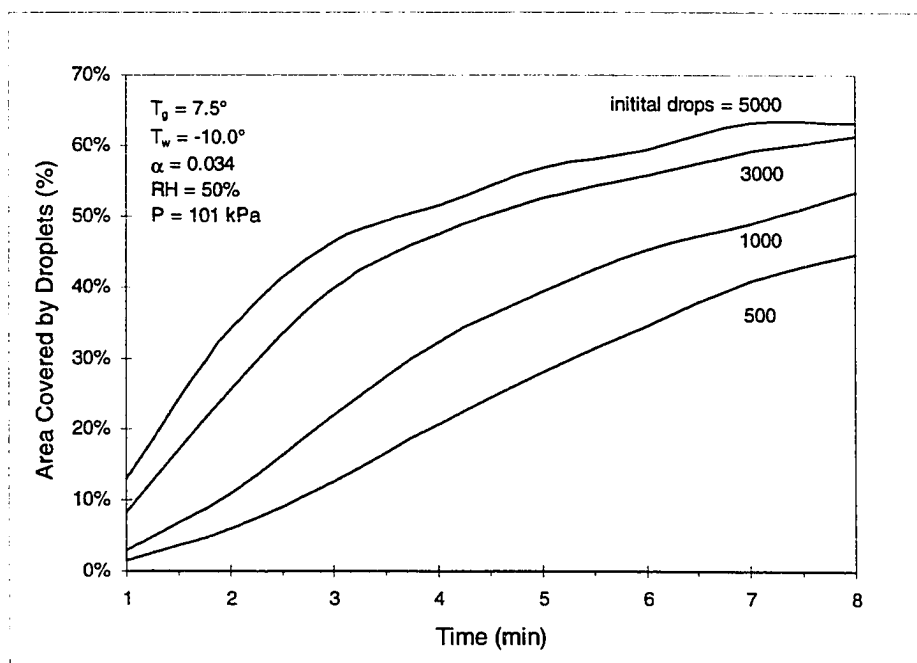
Figure 5.10. Effect of initial droplet population on the percentage of the total surface area covered by droplets as a function of time.

The effect of the condensation coefficient on the droplet growth rate was presented in an earlier section. Here, the effect has been taken into the simulation

program and the results of two values for the condensation coefficient are shown in Figure 5.11. The mass of water condensed when the condensation coefficient was allowed to vary as a function of the droplet radius was almost 200% greater than the amount given for a constant value of α. This same effect had been shown earlier when describing the effects of α on the droplet growth rate. As with the initial droplet population however, the effect of α may also be estimated by considering the cumulative percentage of surface area covered by droplets.
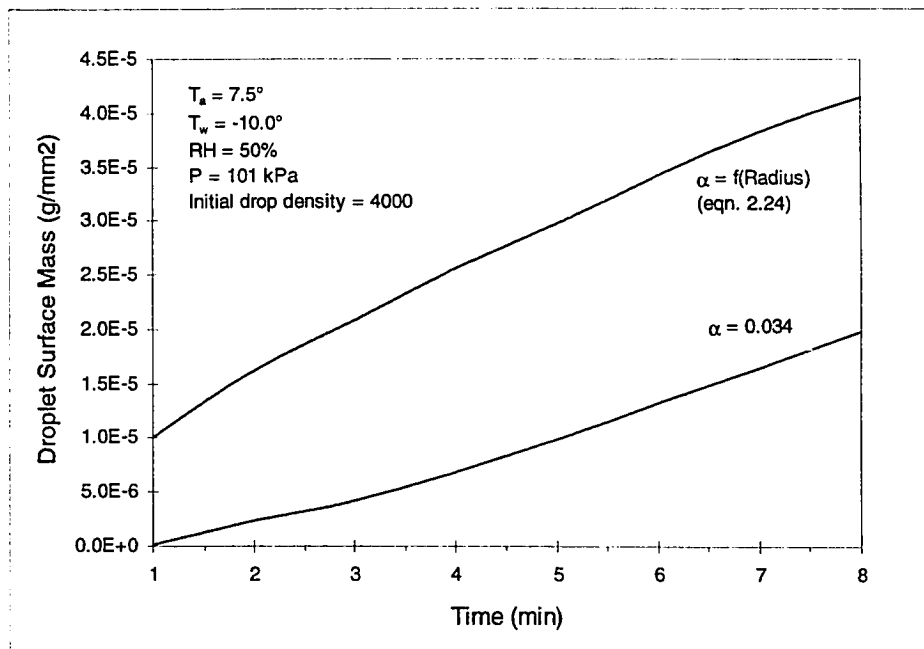
Figure 5.11. Effect of condensation coefficient on mass of water condensed onto a flat surface.

Figure 5.12 shows that for $\alpha = 0.034$ the area covered was approximately 62% and that the curve had gone asymptotic at that level. The condensation coefficient given by equation 2.24 was shown to be at a covering percentage of about 75%. This was

considerably above the 55 - 65% coverage found both in the steam literature and from experimental observations. These figures supported the use of $\alpha = 0.034$ for these type condensation processes.
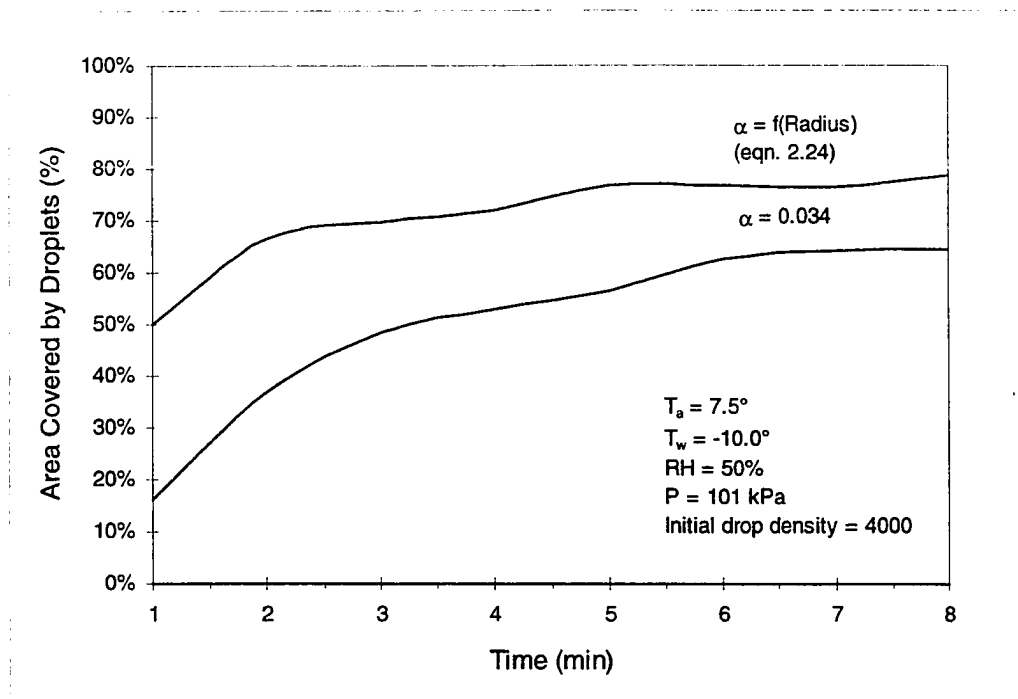
Figure 5.12. Effect of the condensation coefficient on cumulative percentage area covered by droplets as a function of time.

Finally, Figure 5.13 shows the effect on the condensation model of a varying contact angle. This was how the proposed model accounted for different surfaces in the dropwise condensation process. Uncoated metals tend to have high surface energies and thus have low contact angles. Values of 65 - 90° have been reported for copper and aluminum surfaces (Ahlborn, 1976). Conversely, polymer coatings commonly have surface energies much lower than 20 mN/mm^2 and are extremely hydrophobic (Cary, 1992). These surfaces exhibit contact angles of 90 - 115° for water (Ahlborn, 1976).

Contact angles of 85°, 100°, and 110°, for uncoated copper, silicone conformal coated copper, and sulfur long-chain polymer coated copper respectively, were used for the three surface treatments.

Figure 5.13 shows that for increasing contact angles, the total mass condensed onto the surface as a function of time also increased. There was approximately a 32% difference in total mass after eight minutes of simulation time between contact angles of 85° and 100°. Between contact angles of 100° and 110° the percent difference was about 20%. These differences were dependent on the total time the simulation was allowed to run.
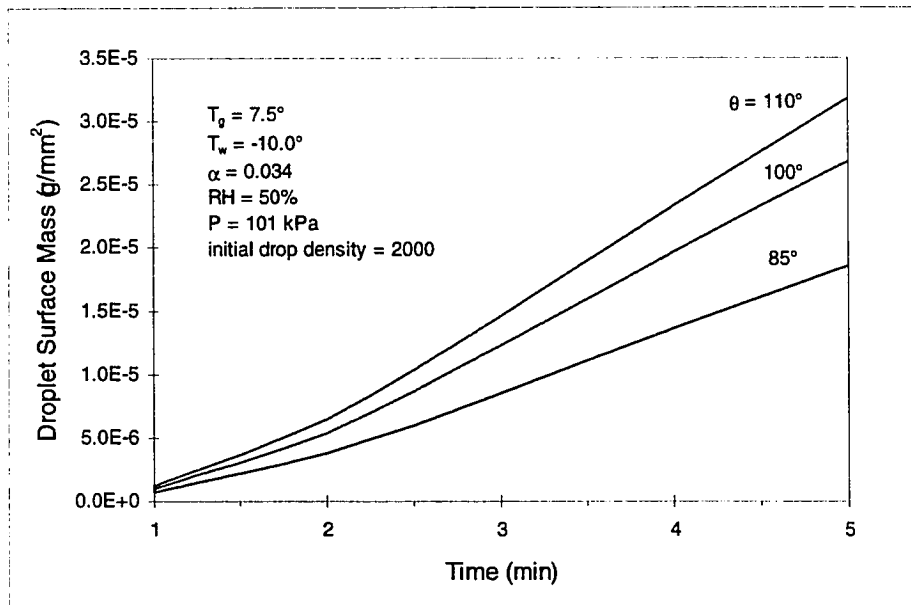
Figure 5.13. Effect of contact angle on mass of water condensed onto a surface as a function of time.

Dropsize Distributions

The preceding section results were obtained by evaluating the dropsize

distribution at discrete time intervals. The volume and mass allowed for convenient

quantitative evaluation of the model's output. The actual distribution of sizes becomes

important if one is involved with modeling the initial stages of frost or ice growth on cold

surfaces (Tao and Besant, 1992). Droplet distribution data, especially time series data, do

not easily lend themselves to analysis. Figure 5.14 shows the "messy" result of a time

series for a simulation at T_g = 7.5° C, T_w = -10.0° C, RH = 50%, θ = 100°, r* = 0.67 μm,

and an initial droplet population of 4000 drops.
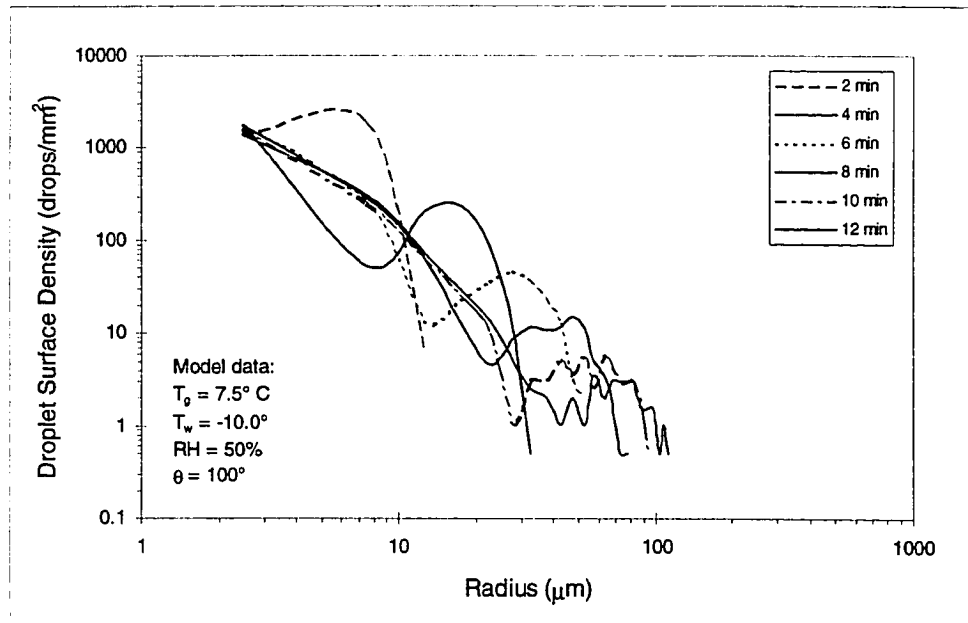
Figure 5.14. Dropsize distribution from model simulation at 2 minute intervals.

The time series are shown in two minute increments to allow the trends to become

visible. The early distributions showed a relatively clean initial decay followed by a bell-

shaped peak. The latter stages of the simulation all had this general characteristic as well.

In general the distributions all had this same structure. Family and Meakin (1988) found very similar droplet distribution structures for simulations of vapor deposition of tin on a sapphire surface. The bimodal distribution was evidenced in their studies as well. They described their distribution as an initial power-law decay, superimposed on a monodispersed, bell-shaped distribution peaked at the mean cluster size of the of the given distribution. They suggested scaling of these type distributions would be given by plotting $s^\tau N_t(s)$ against s/S_{max}. Where s^τ was the size at some time t, $N_t(s)$ was the number of droplets of size r at that time, and S_{max} was the value of the mean cluster size for that time. Using the nomenclature for this study the resulting scaling equations would be given as

$$\ln(r_{range}^\tau N(r_{range})) \quad \text{and} \quad \ln\left(\frac{r_{range}}{R_{max}}\right) \qquad 5.10$$

Figure 5.15 shows the resulting plot using the scaling equations for the simulation data as described above. There are several interesting features in this figure. The best scaling was obtained with $\tau = 2.0$ which compared favorably with the value of $\tau = 1.67$ Family and Meakin found for their data. Abscissa values of zero corresponded to the peaks of the distribution (R_{max}) or the mean cluster size. This was also the value that generated the highest volume of condensate for a given radius range over the range of radii of the distribution. The scaling data can now be regressed which leads to a linear expression (y = a + bx) for the number of droplets at a given size with a maximum range size and at a specific time. The regression results are given by

$$N_t\left(r_{range}\right) = 11728\left(\frac{r_{range}}{R_{t,max}}\right)^{-1.85} r_{range}^{-2.0} \qquad 5.11$$
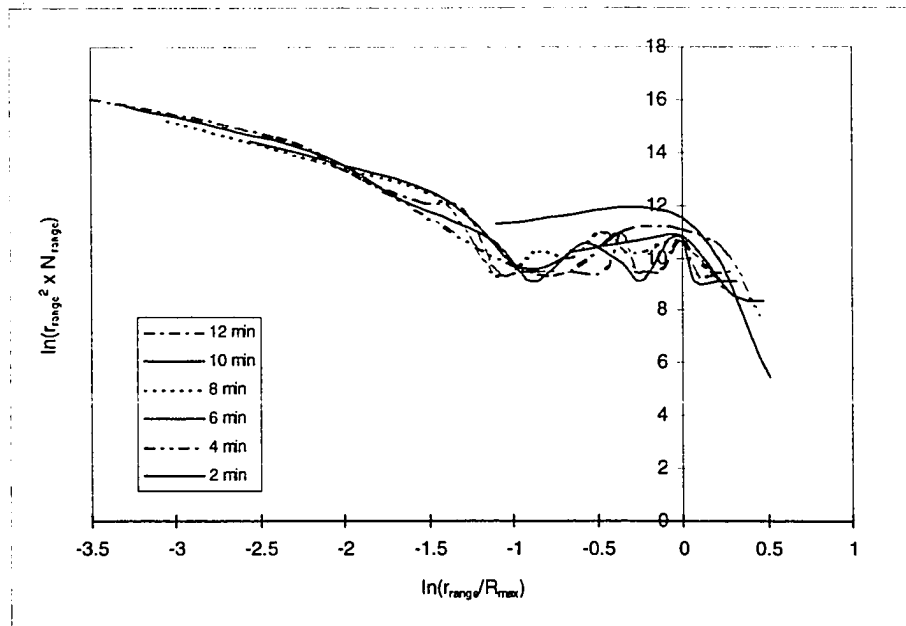
Figure 5.15. Scaling of the condensation drop-size distributions shown in Figure 5.14.

This regression equation has a coefficient of determination of 0.84. Other, higher order regression equations ($y = a + bx + cx^2 + dx^3 + ... + hx^7$) were available with higher coefficients of determination, but the increased complexity of these equations did not warrant their use. This is illustrated in Figure 5.16, where the 12th minute of the simulation of Figure 5.14 is shown with the scaling given by equation 5.11 and with a 7th order regression curve. The higher order (h.o.) curve provided a better fit to the model distribution at the smaller radii than did the linear model. However, the linear model was much better at predicting the larger radii. From a practical standpoint, the larger radii are the "more important" droplets on the surface at this time for two reasons. First, the larger droplets contain the majority of the mass of condensate on the surface (recall that $V \sim r^3$). This is reflected by the correspondence between the mean cluster size and the largest volume fraction contribution of any of the radii ranges.
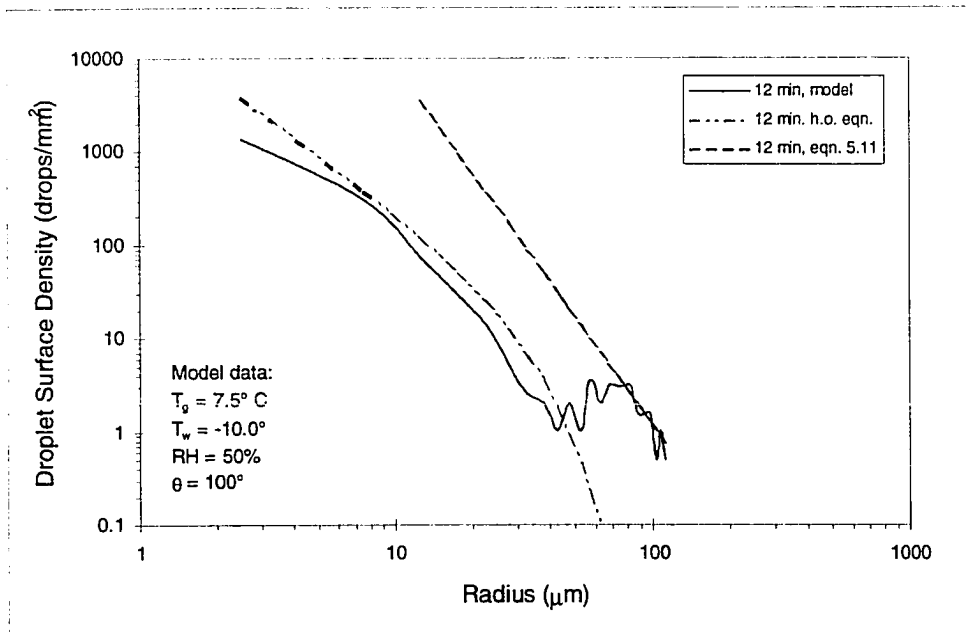
Figure 5.16. Comparison of linear and higher order scaling regression to 12th minute simulation data of Figure 5.14.

Secondly, the droplets equal to or larger than the mean cluster size are the sizes that generally freeze first and are the initial sites for subsequent frost growth. The linear model provided better estimates of both of these quantities.

Figure 5.17 shows ratios of the regression dropsize estimate divided by the model dropsize distribution. This figure quantified the goodness of the estimate for the two regression forms. Ratios of 1.0 indicated exact agreement between the regression and the model data. The linear model ratios were consistently close to 1.0 in the region of the mean cluster size and deviated rapidly at radii values greater than 100 and less than 70 μm. The higher order regression showed good agreement for radii in the range of 7.5 to 30 μm and around 40 μm. Again, these radii were not significant from a physical standpoint based on the volume fraction of condensate on the surface, and because only the larger sizes were important to ice nucleation and frost growth.
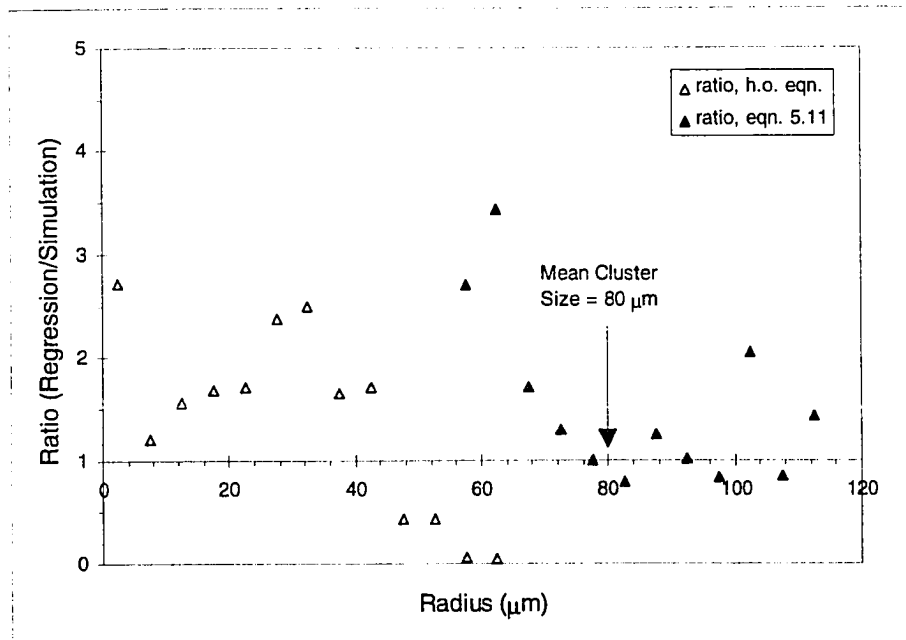
Figure 5.17. Comparisons of goodness of fit for linear model versus a higher order
scaling regression.

Conclusions

This chapter presented the development and results of a model that simulated the
dropwise condensation of atmospheric vapor onto a cold surface. The model included
several extensive variables as well as the stochastic nature of the nucleation and growth
process. Variables included were; air temperature, surface temperature, air relative
humidity, and water contact angle (varies with surface type). The effects of these
variables were described and quantified when possible.

During the development and evaluation of the condensation model used in the present study, several conclusions were drawn

A. The droplet growth term in the model is *the* critical element in the model.

B. The interface temperature governs the heat transfer to the droplet and must be in describe by terms that the engineer can use.

C. The condensation coefficient used in the model must be applicable. Values from the steam literature result in unreasonable droplet growth rates.

D. The initial droplet population is important for reasonable terminal dropsize distributions.

E. The scaling form provides a convenient method of estimating the dropsizes around the mean cluster size for a given distribution.

CHAPTER VI

COMPARISON OF EXPERIMENTAL RESULTS WITH MODEL

In this chapter, the experimental results are compared to those predicted by the model. Many of the potentially misleading model results were identified in Chapter V during the development of the model. Here, as comparisons are made and discussed, shortcomings and further improvements to the model will be suggested.

The following variables were previously identified as important to the condensation process and the dropsize distribution through the statistical analysis of the experimental data and evaluation of perturbations of the model;

1. Surface Treatment (evaluated through contact angle)

2. Ambient Moisture Level (humidity ratio or relative humidity)

3. Air Temperature

Given the above variables as inputs to the model and conditions of an experiment, comparisons were made based on several extensive measurements which were evaluated at the terminal point (ice nucleation) or as a function of time;

1. Total Volume (Mass) of Condensate on the Surface and

2. Distribution of Droplet Sizes.

For the range of experimental values used for this work, it was found that the level of heat transfer nor the Reynolds number exerted significant influence over the time at which the liquid droplets nucleated to ice. This is not to say that these mechanisms were not present, but that the constant surface temperature of -10.0° C essentially "locked" the heat transfer rate and the effect of changing the Reynolds number was not measurable on the time for nucleation to occur. Thus, neither of these factors were

included explicitly in the model or, subsequently, in the following comparisons of experimental data and the condensation model.

Primary Results

As found during the development and evaluation of the model, the volume (mass) of condensate per unit area was a convenient means of presenting condensation data. Figure 6.1 shows the comparison of experimental data at a low air temperature and low relative humidity to a simulation of the dropwise condensation process under the same conditions.

Figure 6.1. Comparison of model to experimental data for dropwise condensation at low temperature, low relative humidity and on an uncoated copper surface.

These data represent all tests done at the above conditions for condensation on a polished, uncoated copper plate. The time series data for the model and experiment agree very well over the entire range of values. Error bars on the model indicate the sensitivity (or uncertainty) of the model. As described in the experimental results chapter, freezing times at these conditions were usually much longer than for any other conditions. Thus, even at long run-times, the model accurately predicted the amount of condensate on the surface as a function of time. Uncertainty on the experimental data was approximately $\pm$ 5%. Figure 6.2 shows the result of taking the ratios of the mass of condensate (g/mm^2) on the respective surfaces for the model and the experimental value for the conditions shown in Figure 6.1. Ratios of 1.0 indicate perfect agreement between the model estimate and the experimental data.
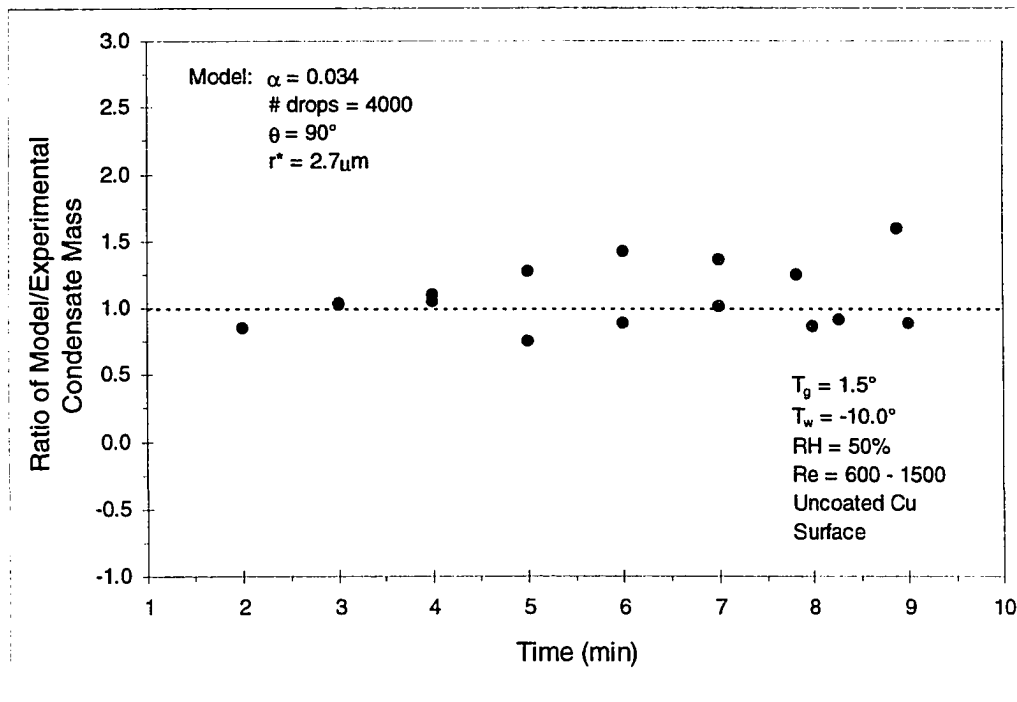
Figure 6.2. Ratios of model to experimental condensate mass data of Figure 6.1.

The majority of the data points are within a band of ±0.25 with only a few between 0.25 and 0.5. This shows very good agreement between the model and the experimental data.

The comparisons made for the previous figures were for condensation on an uncoated, polished copper surface (0.2 - 0.4 µm rms roughness). Figure 6.3 shows the time series comparison for the model and experimental data for condensation on a copper surface coated with a silicone conformal polymer. The data set in Figure 6.3 is shifted higher on the ordinate axis relative to the data shown in Figure 6.1 which indicates more mass per unit area under conditions of higher humidity. In addition, the delay in nucleation time is evidenced by the number of data points that are further out on the time scale. This was a result of the delaying effect of the silicone conformal coating.
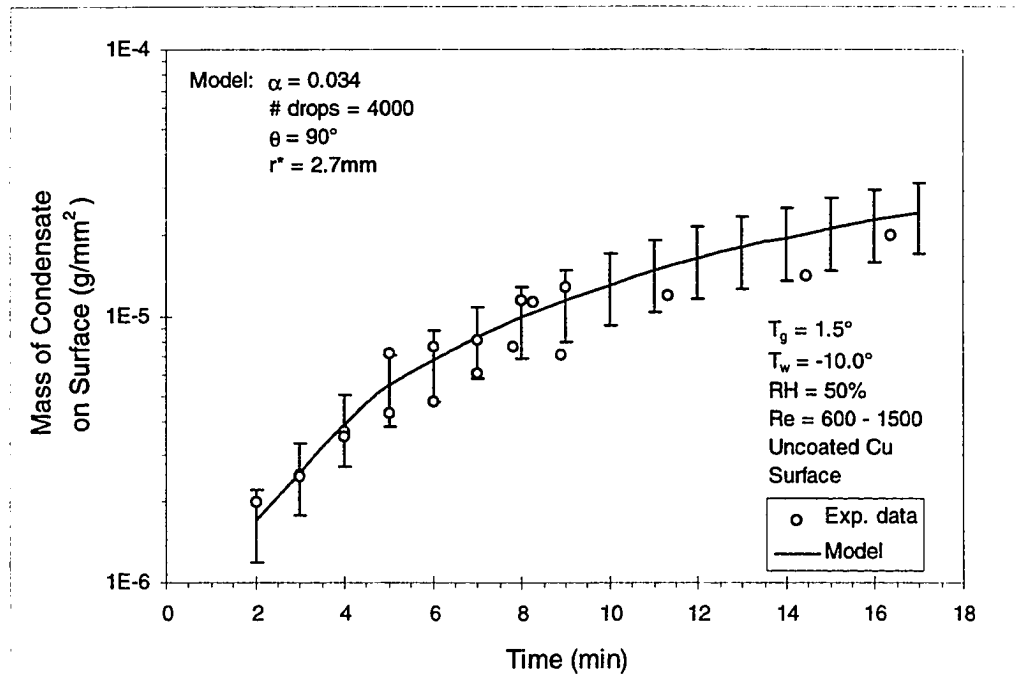

Figure 6.3. Comparison of model to experimental data for dropwise condensation at low temperature, low relative humidity on a copper surface coated with a silicone conformal polymer.

As with the uncoated example in Figure 6.1, there appears to be excellent agreement
between the model estimates and the experimental values. A sensitivity analysis for the
various inputs to the model under the conditions shown in Figure 6.3 yielded a ± 30%
range to the model estimate. This sensitivity is represented by the vertical error bars on
the solid line in Figure 6.3. Figure 6.4 shows the ratio of the model to the experimental
data. Overall, the ratio plot shows deviations of less than 0.5 from the unit line with
many points less than 0.25. Few values below the unit line would indicate that the model
is, in general, slightly over-predicting the mass of condensate on the surface. Recall
however, that the volume of a droplet varies with the cube of the radius of curvature and
as such small changes in the contact angle will result in large volume changes.
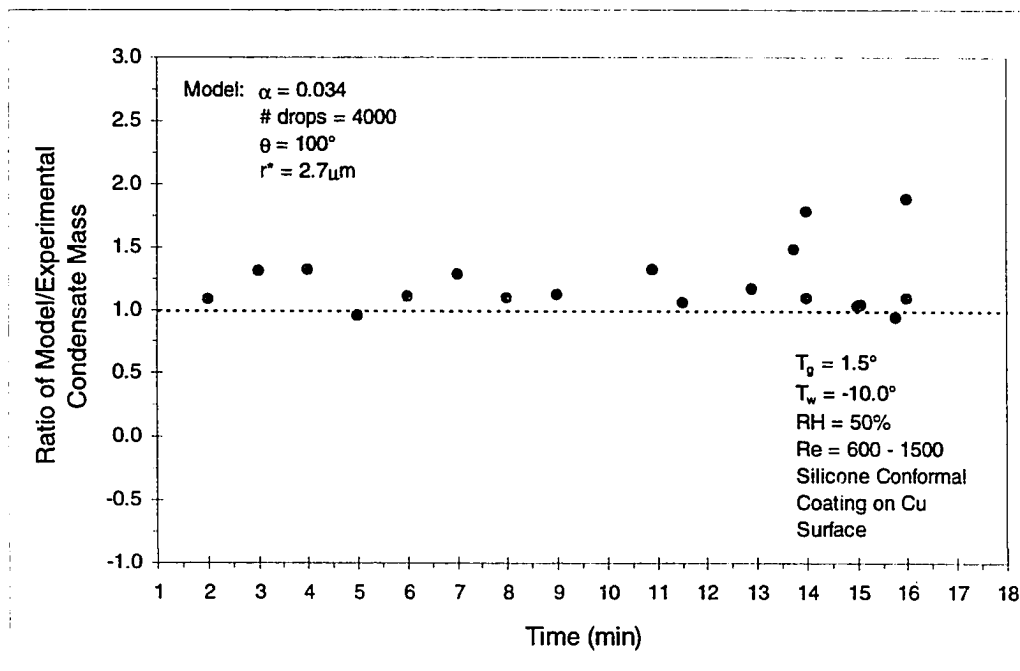
Figure 6.4. Ratios of model to experimental condensate mass data of Figure 6.3.

From a practical standpoint, the conditions of these data are not very common for heat pump systems operating in the heating mode. More common conditions would be higher humidity at a given dry bulb temperature. Figure 6.5 displays a comparison of the model and experimental data for the conditions of $T_g = 1.5$ and RH = 85%. These data are for condensation on a copper surface coated with a silicone conformal coating. As with the previous data comparisons, this figure shows that the model has the same trend and is well centered in the experimental data. Figure 6.6 shows the ratio data for this comparison. In this figure the ratios indicate that the model is in excellent agreement with the experimental data through about seven minutes of the condensation process. The model then begins slightly to overestimate the condensate mass on the surface. The model still does very well however, considering the spread in the experimental data.
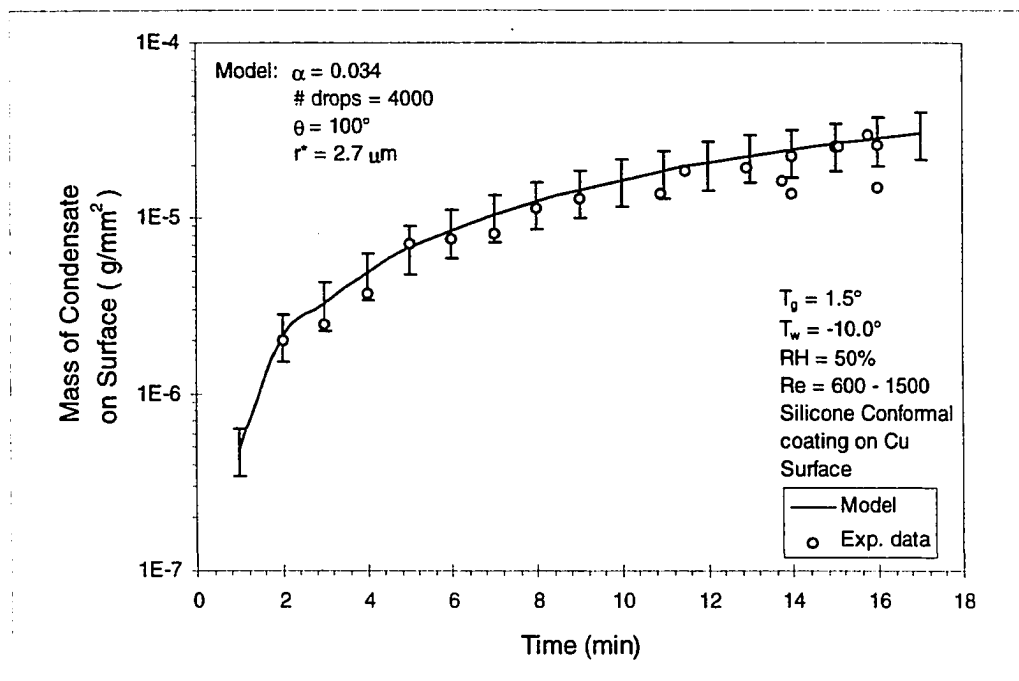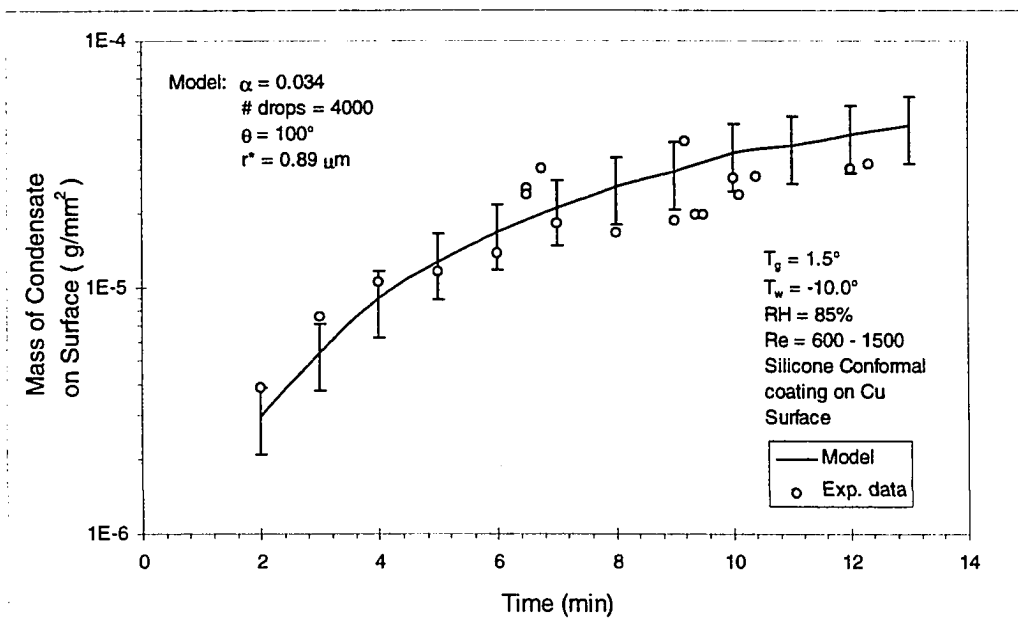

Figure 6.5. Comparison of model to experimental data for dropwise condensation at low temperature, high relative humidity on a copper surface coated with a silicone conformal polymer.
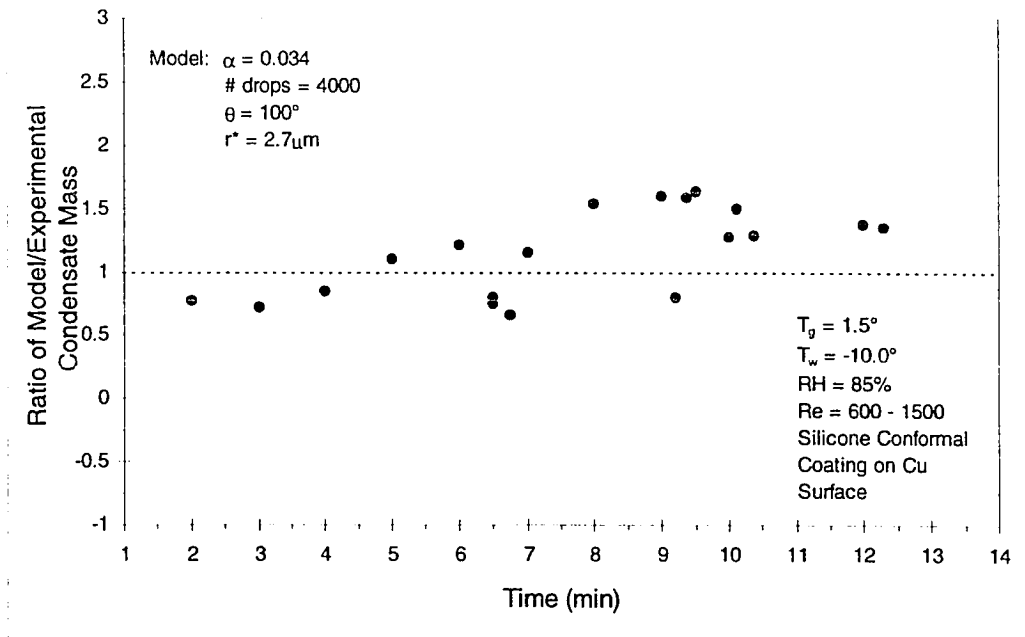
Figure 6.6. Ratios of model to experimental data of Figure 6.5.

The consistently excellent comparison results to the experimental data indicate that the model is indeed emulating the dropwise condensation process under varying conditions and surface treatments. Further comparisons for other experimental conditions are included in the appendices.

Another objective of this research was to provide useful descriptions of the dropsize distributions. In the modeling chapter, a scaling form for the time-series dropsize distributions was developed. Though a good quantitative tool, it is usually desirable to have a qualitative description of the distributions as well. Figure 6.7 is a time-series of images from the condensation model shown in one minute increments. Refer to Figure 4.24 in Chapter IV, page 91, for a qualitative comparison. Both figures show the rapid droplet growth from the initial high density microscopic droplets through to the lower surface density, larger droplets of the terminal dropsize distribution at six

Figure 6.8 shows the droplet surface density for the images shown in Figure 6.7. Note the

similarities between this series of distributions and the distribution shown in Figure 5.14.

Figure 6.9 shows the dropsize distribution for the experimental data shown in Figure 4.24

Figures 6.8 and 9 are very similar though differences are apparent. Most noticeable is the

more complete distribution information for the droplet sizes smaller than about 7.5 mm.

This was a result of the limitations of the optical system used to capture the experimental

images. The microscopy system could not resolve droplets less than five microns in

diameter. Otherwise, the distributions have the same characteristic peaks and valleys.

The scale differences for the ordinate also distort comparison of the general slope of the

peaks. The scaling form for dropsize distribution time-series described in Chapter V can

be applied to the data shown in Figure 6.9. The results of this scaling are given in Figure

6.10.

Figure 6.11 shows the regression form given in equation 5.11 applied to the data

of Figure 6.9. The linear form predicts the droplet sizes centered around the mean cluster

size for each distribution of the time series. As with the model data described in Chapter

V, the linear form was appropriate because it provided information about droplets

important to the total mass fraction of the system.

Figure 6.12 is a single image from the simulation of the data shown in Figure 6.7.

This is the dropsize distribution for the termination of the condensation period and at the

start of the ice nucleation process. This is a qualitative description of the data, and it

shows the same structure as that seen in the laboratory.
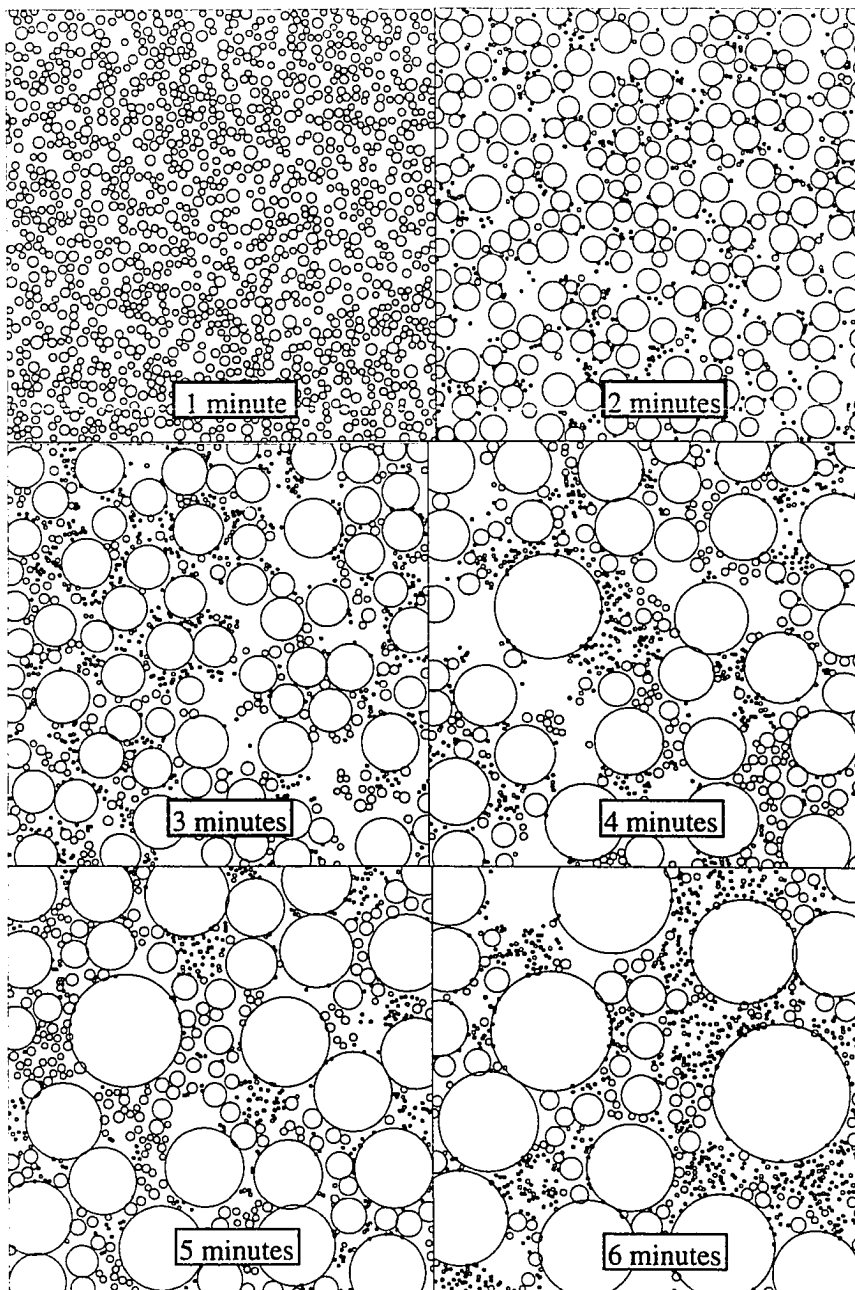
Figure 6.7. Dropwise condensation model time series for condensation on a copper surface. $T_g = 7.5°$ C, RH = 85%
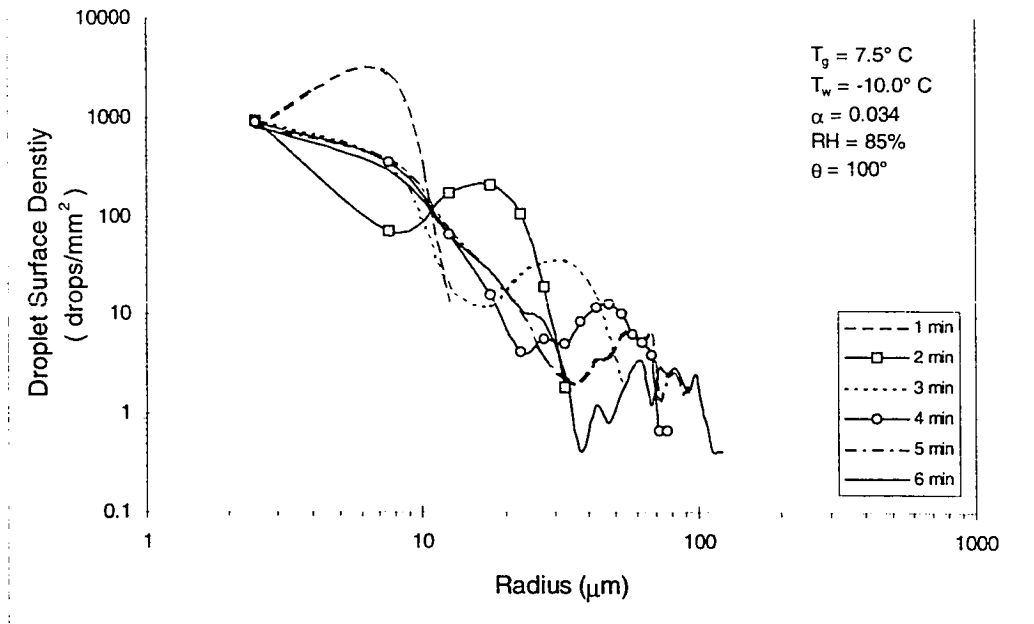
Figure 6.8. Dropsize distribution for the images in Figure 6.7.
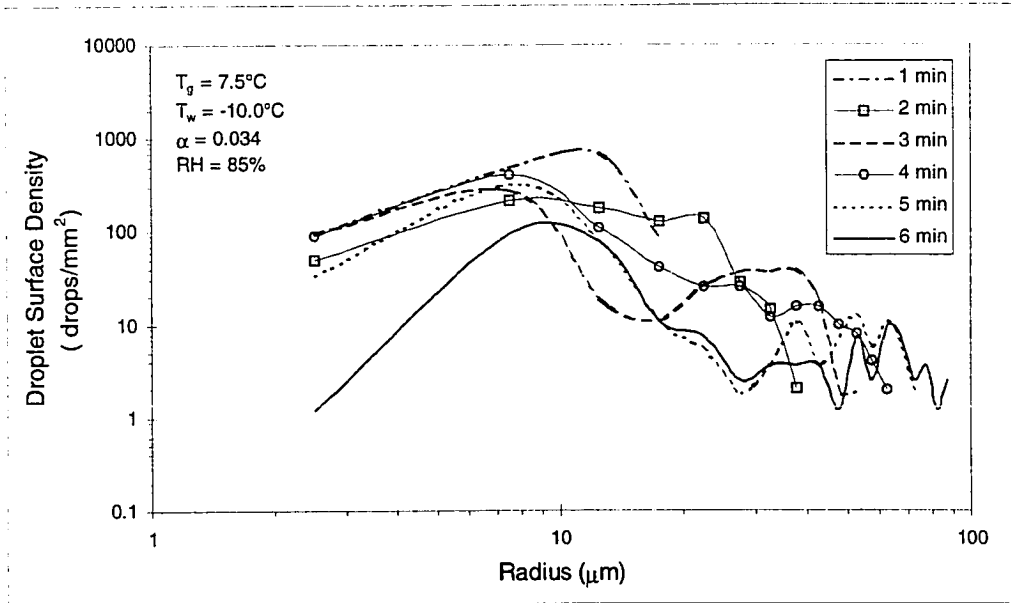
Figure 6.9. Dropsize distribution for experimental images shown in Figure 4.24.
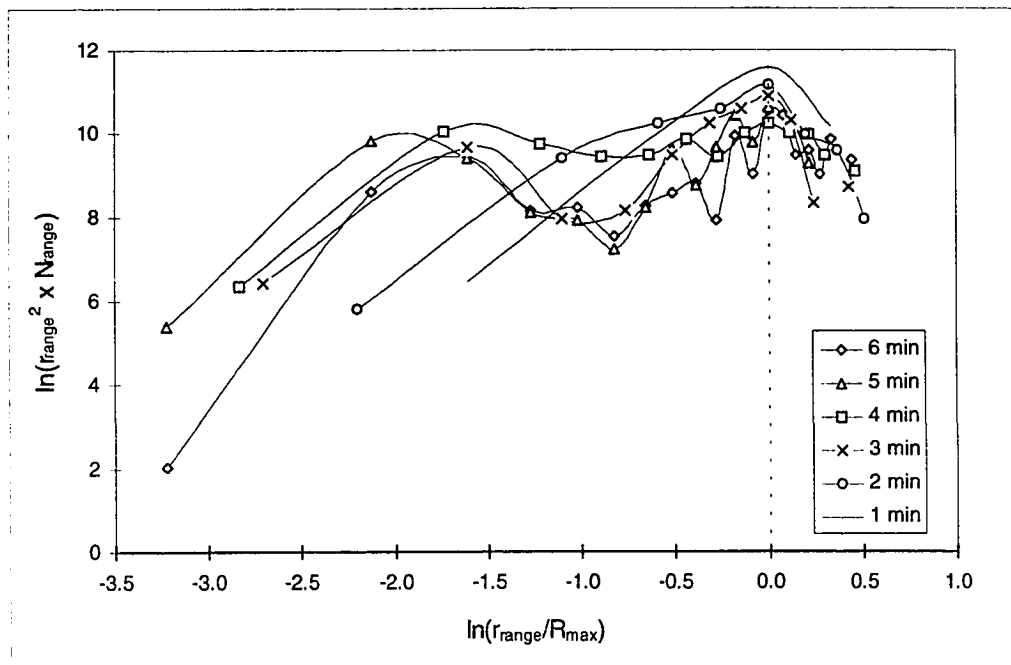
Figure 6.10. Scaling for dropsize distribution applied to experimental data of Figure 6.9.
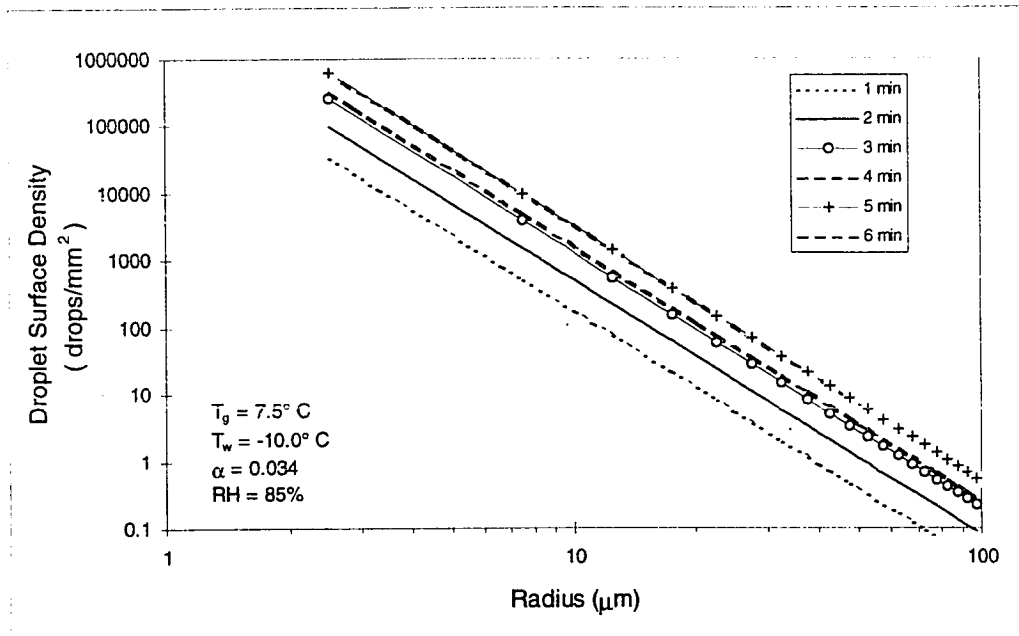
Figure 6.11. Result for scaling equation 5.11 applied to experimental data of Figure 6.9.
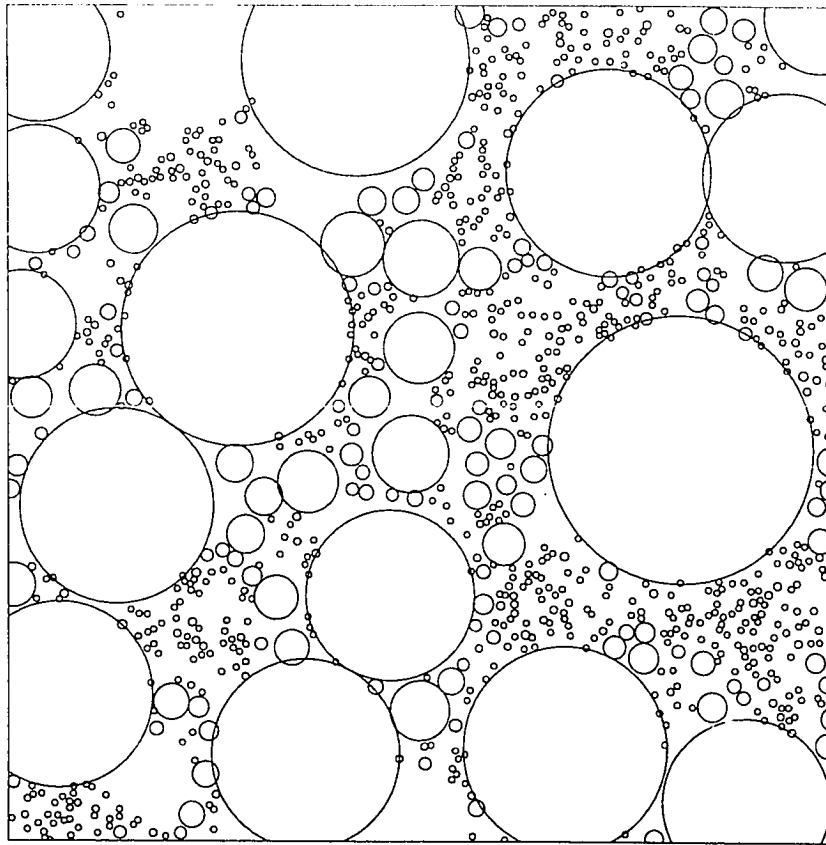
Figure 6.12. Sixth minute of simulation run for $T_g = 7.5°$, RH = 85%, and $\theta = 100°$.

Other Results

A major drawback to the use of the model is that prior knowledge concerning the mean cluster size is required. Even with the scaling of the model data, if the nucleation time for the liquid condensate conversion to ice is not known, the proper termination of the simulation is in question. A technique was developed that would allow the determination of the mean cluster size given appropriate operating conditions (within the range of values for this study). Through a succession of correlation equations, the mean cluster size was estimated with an uncertainty of ±25 %. The process is as follows;

First, the conditions for the estimate must be determined. These would include an estimate of the Re, Gr, and Pr evaluated at some given levels of air temperature, relative humidity and surface treatment. Now use is made of equation 4.11 to estimate the Nu for the stated conditions.

Next, the nucleation time (nucleation from liquid to ice) can be estimated by

$$Nuctime = 41.3 A^{2.6} Nu^{-1.4} W^{-0.6} T_g^{-0.25} \qquad 6.1$$

where A is the ratio of the surface contact angle to a contact angle of 90°, and W is the difference in humidity ratios evaluated for the bulk air and at the surface temperature. This equation resulted from a multiple linear regression of all data taken for this study. The regression had a coefficient of determination of 0.71. With an estimate of the nucleation time given by the above equation, a prediction can now be made for R_{max}. Again, the results of regressing the data yields the following equation for R_{max}

$$R_{max} = 8575 W^{1.5} T_g^{-0.27} Nuctime^{0.77} Re^{0.44} A^{-0.57} \qquad 6.2$$

The coefficient of determination for this equation was 0.69. Now that the mean cluster size has been estimated, the droplet surface density or the mass of the system about the mean cluster size can be evaluated. Equation 5.11 would be used to determine the number of droplets on the surface of size Rmax as well as the numbers of droplets for the ranges on either side of R_{max}. Alternatively, a further regression of the experimental data yielded the following equation for the surface droplet density.

$$N(R_{max}) = 1.28 \times 10^5 R_{max}^{-2.33} \qquad 6.3$$

Unlike equation 5.11 however, equation 6.3 only provides droplet density estimates for the mean cluster size.

Suggested Improvements

In general, the model correlates very well with the experimental data. The model does seem to err on the conservative side when estimating the volume of condensate on the surface.

One criticism of the present model is that it is valid only for a flat plate geometry. This is decidedly different from the high density, parallel fin geometry found on typical heat-pump heat exchangers. The ability of the model to address different finned geometries would be of great utility.

Another very useful addition would be the ability to model "normal" condensation processes. The droplet growth problem for this type of condensation is very different from the steam systems as discussed in earlier chapters. This type of growth and removal of droplets from the surface of the heat exchanger is essentially what all models in the steam literature have addressed. It is an important process in the air conditioning industry and any improvement in the understanding or enhancement would benefit manufacturers and consumers.

CHAPTER VII

CONCLUSIONS AND RECOMMENDATIONS

The effects of hydrophobic coatings on the dropwise condensation process for a flat horizontal copper plate held at a temperature much lower than the surrounding air has been investigated. Extensive qualitative and quantitative data were taken to describe these effects in terms of dropsize distributions, heat transfer, mass transfer, and imaging of the droplets in terms of various extensive properties. A model was developed that accurately predicted the dropsize distribution as a function of time for a given set of ambient conditions. A general scaling form for the surface droplet density was developed and found to be in good agreement with similar forms for vapor deposition studies. A method to predict the Nusselt number, nucleation time, mean cluster size and the droplet surface density in terms of extensive properties that are known a priori was also developed.

Conclusions

1. The droplet growth rate is the critical factor in the model of the dropwise condensation process. Droplet growth rates from the steam literature caused orders of magnitude errors for droplet growth compared to experimental results of this study.

2. The condensation coefficient as used in the steam literature should not be used for atmospheric condensation in the range of air conditioning processes. The values typically cited in the steam literature are for a homogeneous medium with little or no non-condensable gases present. Condensation coefficient values from the cloud physics literature provide better results because the conditions of condensation are

very similar. The condensation coefficient is a prominent component in the present model and the value of 0.034 from the cloud physics literature allowed a ±25% agreement with the experimental data.

3. The use of a hydrophobic surface coating on copper markedly delays the onset of ice nucleation versus an uncoated copper surface. This was shown through the application of an analysis of variance on the experimental data. Depending on ambient conditions, the surface coating caused a delay in nucleation time of from 35 to 68% versus the uncoated copper surface. This delay brings about concomitant differences in the amount of condensate on the surface. The additional time allowed for condensation to occur before the droplets nucleate to ice permits a greater total amount of water vapor to condense on the surface. This was typically 15 to 25% more condensate on the coated surface compared to the uncoated surface.

4. The initial droplet population is important to the simulation of the dropwise condensation process to allow reasonable terminal dropsize distributions. If the starting droplet population was too sparse, the simulation would severely underpredict terminal dropsize distributions and total mass present on the surface. A starting value of 4000 or greater critical radii droplets resulted in model estimates that agreed within ±25% of the experimental values for dropsize distributions and condensate mass. Higher starting values did not improve the model results but did increase the computational time required for the simulation.

Recommendations

The results of the present work have generated the following recommendations for future research.

1. The geometry used for the present work was for a flat plate only. Studies on parallel fin elements would be very useful because they are more typical of heat pump heat exchanger geometry. Perhaps the current results could be extended to simple flat, parallel fin geometries through symmetry.

2. The dynamics of the droplet growth during the early stage of condensation were modeled based upon a few key simplifications. The most important of which was the estimate of the interface temperature. As noted in the literature review, this temperature determines the driving potential for heat transfer through the interface from the gaseous to the liquid phase. Further work is suggested to allow better understanding of the role of interfacial heat transfer and more importantly, the exact nature of the interface temperature.

3. Investigating the droplet condensation, growth, and subsequent removal from a condensing heat exchanger operating in a normal air-conditioning process would be a logical extension of the modeling and experimental work of this study. This is a common process, especially in hot and humid climates, and better understanding of the process could lead to improvements in air-conditioning heat exchanger design or manufacture.

4. The use of the hydrophobic coating technology has been investigated in full-scale tests at Texas A&M (Parker, 1995). This was a short term test but it did show the potential of the coatings. Further long term lab tests or extended field tests would demonstrate more conclusively the effect of the coatings and any ancillary benefits (shedding of condensate, inhibition of corrosion, etc.).

NOMENCLATURE

D   droplet diameter (as noted)

$\mathcal{D}$ diffusion coefficient for water into air (m/s)

G   droplet growth rate

Gr   Grashof Number (dimensionless ratio of buoyancy to viscous forces)

h heat transfer coefficient (W/m^2°C)

$\bar{h}$ average heat transfer coefficient

h_{dci} droplet heat transfer coefficient (W/m^2°C)

i   heat of vaporization (kJ/kg)

k   thermal conductivity (W/mK)

M   molecular weight

N   droplet size distribution

N(r)   drop size distribution function

Nu   Nusselt Number (dimensionless heat transfer coefficient)

p   pressure (kpa)

Pr   Prandtl Number (dimensionless ratio of momentum and thermal diffusivities)

Q   heat transfer (W)

r   radius (as noted)

$\bar{R}$ universal gas constant

R   gas constant for vapor (kJ/kgK)

Ra   Rayleigh Number (dimensionless product of Grashof and Prandtl numbers)

R_d characteristic droplet dimension

Re   Reynolds Number (dimensionless ratio of inertia and viscous forces)

R_{max} maximum droplet radius (as noted)

R_s droplet separation dimension

S   conduction shape factor

Sc   Schmidt Number (dimensionless ratio of momentum and mass diffusivities)

T   temperature (°C)

t   time (s)

v   specific volume (m^3/kg)

W_a work of adhesion (dynes/cm^2)

θ contact angle (degrees)

Γ surface concentration of vapor

α condensation coefficient

β accommodation coefficient

ρ density (kg/m^3)

σ surface tension (dynes/cm^2)

∞ bulk vapor

SUBSCRIPTS

crit   critical

g   vapor

i   interface

l   liquid

lv   liquid-vapor interface

m   mass

sl   solid-liquid interface

sv   solid-vapor interface

s   saturation

w   wall or surface

REFERENCES

Ahlborn, G., H., 1976, "Development of a Hydrophobic Substance to Mitigate Pavement Ice Adhesion," Environmental Protection Agency, Office of Research and Development, EPA-600/2-76-242, Washington, D.C..

ASHRAE, 1991, "Chapter 44: Unitary Air Conditioners and Unitary Heat Pumps," *1991 ASHRAE Handbook-Equipment*, American Society of Heating, Refrigerating, and Air-Conditioning Engineers, Atlanta, Georgia.

ASHRAE, 1993, "Chapter 4: Mass Transfer," *1993 ASHRAE Handbook-Fundamentals*, American Society of Heating, Refrigerating, and Air-Conditioning Engineers, Atlanta, Georgia.

ASTM, 1972, Manual on the use of Thermocouples in Temperature Measurement, ASTM Special Technical Publication 470, American Society of Testing and Materials, Philadelphia, Pennsylvannia.

Bird, R. B., Stewart, W. E., and Lightfoot, E. N., 1960, *Transport Phenomena*, John Wiley and Sons, Inc., New York, p. 399.

Carey, V. P., 1992a, *Liquid-Vapor Phase-Change Phenomena: An Introduction to the Thermophysics of Vaporization and Condensation Processes in Heat Transfer Equipment*, Hemisphere Publishing Corporation, New York, pp. 342-344.

Carey, V. P., 1992b, *Liquid-Vapor Phase-Change Phenomena: An Introduction to the Thermophysics of Vaporization and Condensation Processes in Heat Transfer Equipment*, Hemisphere Publishing Corporation, New York, pp. 343-344

Carey, V. P., 1992c, *Liquid-Vapor Phase-Change Phenomena: An Introduction to the Thermophysics of Vaporization and Condensation Processes in Heat Transfer Equipment*, Hemisphere Publishing Corporation, New York, p. 348.

Chen, C.S., 1974, "Evaluation of the Water Vapor Diffusion Coefficient in the Drop

Growth Equation," *Journal of the Atmospheric Sciences*, Vol. 31, pp. 845-847.

Churchill, S.W., 1977, "A Comprehensive Correlating Equation for Laminar,

Assisting, Forced and Free Convection," *AIChE Journal*, Vol. 23, No.1, pp. 10-

16.

Department of the Air Force, 1978, *Engineering Weather Data*, AFM 88-29,

Washington, D.C.

Dorsey, N. E., 1948, "The Freezing of Supercooled Water," *Transactions of the*

American Philosophical Society, Vol. 38, Part 3, pp. 246-327.

Fujii, T., 1991, *Theory of Laminar Film Condensation*, Springer-Verlag, New York.

Fukuta, N. and Walter, LaA., 1970, "Kinetics of Hydrometeor Growth From a Vapor-

Spherical Model," *Journal of the Atmospheric Sciences*, Vol. 27, pp. 1160-1172.

Glicksman, L.R., and Hunt, A.W., 1972, "Numerical Simulation of Dropwise

Condensation," *International Journal of Heat and Mass Transfer*, Vol. 15, pp.

2251-2269.

Graham, C., and Griffith, P., 1973, "Drop Size Distributions and Heat Transfer in

Dropwise Condensation," *International Journal of Heat and Mass Transfer*,

Vol.16, pp. 337-346.

Hagen, D.E., Schmitt, J., Trueblood, M., Carstens, J., White, D.R., and Alofs, D.J.,

1989, "Condensation Coefficient Measurement for Water in the UMR Cloud

Simulation Chamber," *Journal of the Atmospheric Sciences*, Vol. 46, No. 6, pp.

803-814.

Hautman, J., and Klein, M.L., 1991, "Microscopic Wetting Phenomena," *Physical*

Review Letters, Vol. 67, No.13, pp. 1763-1766.

Hinkle, D.E., Wiersma, W., and Jurs, S.G., 1994, *Applied Statistics for the Behavioral Sciences*, 3rd ed., Houghton Mifflin Company, Boston, p. 403.

Holden, K.M., Wanniarachchi, A.S., Marto, P.J., Boone, D.H., and Rose, J.W., 1987, "The Use of Organic Coatings to Promote Dropwise Condensation of Steam," ASME JOURNAL OF HEAT TRANSFER, Vol. 109, pp. 768-774.

Igoshin, Vol.A., Postol, Vol.I., Paasivuori, P., and Khakala, R., 1989, "Surface Influence on Adhesion of Ice," *Soviet Journal of Friction and Wear*, English translation, Vol. 10, No.2, pp. 111-114.

Incropera, F.P., and DeWitt, D.P., 1985, *Fundamentals of Heat and Mass Transfer*, John Wiley and Sons, New York, pp. 323.

Itagaki, K., 1983a, "Adhesion of Ice to Polymers and Other Surfaces," *Physiochemical Aspects of Polymer Surfaces, Volume 1*, Edited by K.L. Mittal, Plenum Press, New York.

Itagaki, K., 1983b, "The Implications of Surface Energy in Ice Adhesion," *Journal of Adhesion*, Vol. 16, pp. 41-48.

Jellinek, H.H.G., Kachi, H., Kittaka, S., Lee, M., and Yokota, R., 1978, "Ice Releasing Block-copolymer Coatings," *Colloid and Polymer Science*, Vol. 256, pp. 544-551.

Katoh, H., Suzuki, K., Kariyazono, Y., Ohtsuki, F., Sato, K., and Saeki, H., 1989, Durability of Coated Steel in Sea Ice Regions, *Proceedings of the Eighth International Conference on Offshore Mechanics and Arctic Engineering*, American Society of Mechanical Engineers, Volume III, pp. 213-220.

Landy, M., and Freiberger, A., 1967, "Studies of Ice Adhesion I. Adhesion of Ice to Plastics," *Journal of Colloid and Interface Science*, Vol. 25, pp. 231-244.

LeFevre, E.J., and Rose, J.W., 1964, "Heat Transfer Measurements During Dropwise Condensation of Steam," *International Journal of Heat and Mass Transfer*, Vol. 7, pp. 272-273.

Maa, J.R., 1983, "The Role of Interfaces in Heat Transfer Processes," *Advances in Colloid and Interface Science*, Vol. 18, pp. 227-280.

Marto, P.J., Looney, D.J., Rose, J.W., and Wanniarachchi, A.S., 1986, "Evaluation of Organic Coatings for the Promotion of Dropwise Condensation of Steam," *International Journal of Heat and Mass Transfer*, Vol. 29, No. 8, pp. 1109-1117.

McBride, J.M., 1992, "Crystal Polarity: A Window on Ice Nucleation," *Science*, Vol. 256, No. 8, p. 814.

McCormick, J.L., and Baer, E., 1963, "On the Mechanism of Heat Transfer in Dropwise Condensation," *Journal of Colloid Science*, Vol. 18, pp. 208-216.

McCormick, J.L., and Westwater, J.W., 1966, "Drop Dynamics and Heat Transfer During Dropwise Condensation of Water Vapor on a Horizontal Surface," *Chemical Engineering Progress Symposium Series*, Vol. 62, pp. 120-134.

Meakin, P., 1992, "Steady State Behavior in a Model for Droplet Growth, Sliding, and Coalescence: the Final Stage of Dropwise Condensation," *Physica A*, Vol. 183, pp. 422-438.

Mikic, B.B., 1968, "On Mechanism of Dropwise Condensation," *International Journal of Heat and Mass Transfer*, Vol. 12, pp. 1311-1323.

Mills, A.F., and Seban, R.A., 1967, "The Condensation Coefficient of Water," *International Journal of Heat and Mass Transfer*, Vol. 10, pp. 1815-1827.

Minkowycz, W.J., and Sparrow, E.M., 1966, "Condensation Heat Transfer in the

Presence of Noncondensables, Interfacial Resistance, Superheating, Variable

Properties, and Diffusion," *International Journal of Heat and Mass Transfer,*

Vol. 9, pp. 1125 - 1144.

Mussalli, Y.G., Gordon, L.S., and Daly, S.F., 1987, "Frazil Ice Control Using

Electromechanical Vibrators and Ice-resistant Coatings," *Waterpower '87,*

Proceedings of the International Conference on Hydropower, American Society

of Civil Engineers, Portland, Oregon.

National Institute for Standards and Testing, 1972, "Manual on Temperature

Calibration for State Laboratories," Washington, D.C..

O'Neal, D.L., and Tree, D.R., 1985, "A Review of Frost Formation in Simple

Geometries," *ASHRAE Transactions*, Vol. 91, Part 1, p. 267.

O'Neal, D.L., Anand, N.K., Peterson, K.T., and Schliesing, S., 1989, "Determination

of the Transient Response Characteristics of the Air-Source Heat Pump During

the Reverse Cycle Defrost," ESL/88-05R, ASHRAE Project 479-TRP, Energy

Systems Laboratory, Texas A&M University, College Station, Texas.

Ostin, R. and Johannesson, G., 1991, "A Polymeric Approach to Counteract Frosting

in Air-to-Air Heat Exchangers," *Heat Recovery Systems & CHP*, Vol. 11, No. 5,

pp. 415-421.

Parker, B.D., 1995, The Effects of Outdoor Heat Exchanger Hydrophobic Treatment on

the Performance of an Air Source Heat Pump," Masters Thesis, Texas A&M

University, College Station, Texas.

Peters, G., and Eggebrecht, J., 1991, "Structure and Thermodynamics of Vapor

Condensate in a Finite System," *Journal of Physical Chemistry*, Vol. 95, pp. 909-

920.

Pingry, J., R., and Engdahl, R., B., 1965, "Surface-moisture Phenomena under Icing Conditions," *Humidity and Moisture, Measurement and Control in Science and Industry*, Vol. II, pp. 355-362, Reinhold Publishing, New York.

Rose, J. W., and Glicksman, L.R., 1973, "Dropwise Condensation - The Distribution of Drop Sizes," *International Journal of Heat and Mass Transfer*, Vol. 16, pp. 411-425.

Saito, H., and Tokura, I., 1991, Heat and Mass Transfer in the Frosting Process on Cold Surfaces, *Freezing and Melting Heat Transfer in Engineering, Selected Topics on Ice-water Systems and Welding and Casting Processes*, Chapter 13, K.C. Cheng and N. Seki eds., John Wiley and Sons, New York.

Schmidt, D., Coburn, C., DeKoven, B., Potter, G., Meyers, G., and Fischer, D., 1994, "Water-based non-stick Hydrophobic Coatings," *Nature*, Vol. 368, pp. 39-41.

Schmidt, E., Schurig, W., and Sellschopp, W., 1930, "Versuche über die Kondensation von Wasserdampf in Film und Tropfenform," *Technische Mechanik und Thermodynamik*, Vol. 1, pp. 53-63.

Schrage, R.W., 1953, *A Theoretical Study of Interphase Mass Transfer*, Columbia University Press, New York.

Song, Y., Xu, D., and Lin, J., 1991, "A Study on the Mechanism of Dropwise Condensation," *International Journal of Heat and Mass Transfer*, Vol. 34, No. 11, pp. 2827-2831.

Sparrow, E.M., Minkowycz, W.J., and Saddy, M., 1967, "Forced Convection Condensation in the Presence of Noncondensables and Interfacial Resistance, *International Journal of Heat and Mass Transfer*, Vol. 10, pp. 1829-1845

Stambaugh, Leo, Private Communications, Texas Utility Electric Company, Dallas, Texas, August 13, 1990.

Sugawara, S., and Katusuta, K., 1966, "Fundamental Study on Dropwise Condensation," *Proceedings of the 3rd International Heat Transfer Conference*, Vol. 2, pp. 354-361.

Sucec, J., 1985, *Heat Transfer*, WM. C. Brown Publishers, Dubuque, Iowa.

Tanaka, H., 1975a, "A Theoretical Study of Dropwise Condensation," ASME JOURNAL OF HEAT TRANSFER, Vol. 97, pp. 72-78.

Tanaka, H., 1975b, "Measurements of Drop-Size Distributions During Transient Dropwise Condensation," ASME JOURNAL OF HEAT TRANSFER, Vol. 97, pp. 341-346.

Tanaka, H., and Shigeo, H., 1975, "Drop Size Distributions and Heat Transfer in Dropwise Condensation - Condensation Coefficient of Water at Low Pressures," ASME JOURNAL OF HEAT TRANSFER, Vol. 97, pp. 1671-1676.

Tanaka, H., 1981, "Effect of Knudsen Number on Dropwise Condensation," ASME JOURNAL OF HEAT TRANSFER, Vol. 103, pp. 606-607.

Tanaka, H, and Hatamiya, S., 1986, "Drop-Size Distributions and Heat Transfer in Dropwise Condensation - Condensation Coefficient of Water at Low Pressures," *Proceedings of the 8th International Heat Transfer Conf.*, San Francisco, Vol. 4, pp. 1671-1676

Tanasawa, I. 1978, "Dropwise Condensation; The Way to Practical Applications," *Proceedings of the Sixth International Heat Transfer Conference*, Toronto, pp. 393-405.

Tao, Y.X, and Besant, R.W., and Mao, Y., 1993, "Characteristics of Frost Growth on a Flat Plate During the Early Growth Period," *ASHRAE Transactions*, Vol. 99, Part 1.

Umur, A., and Griffith, P., 1965, "Mechanism of Dropwise Condensation," ASME JOURNAL OF HEAT TRANSFER, Vol. 87, pp. 275-282.

Viovy, J.L., Beysens, D., and Knobler, C.M., 1988, "Scaling Description for the Growth of Condensation Patterns on Surfaces." *Physical Review A*, Vol. 37, No. 12, pp. 4965-4970.

Welch, J.F., and Westwater, J.W., 1961, "Microscopic Study of Dropwise Condensation," *Proceedings of the 1961-1962 International Heat Transfer Conference*, ASME, Part II, pp. 302-309.

Young, David, J., 1980, "Development of a Northern Climate Residential Air-Source Heat Pump," *ASHRAE Transactions*, Vol. 86, Part 1, pp. 671-686.

APPENDIX A

Included in this appendix are figures showing comparisons of the model to experimental data. Refer to Chapter V for more detailed explanations concerning these comparisons.

Figure A.1. Comparison of model to experimental data, uncoated copper surface, $T_g = 1.5°$ C, 85%RH.

Figure A.2. Comparison of model to experimental data, uncoated copper surface,
$T_g = 7.5°$ C, 50%RH.
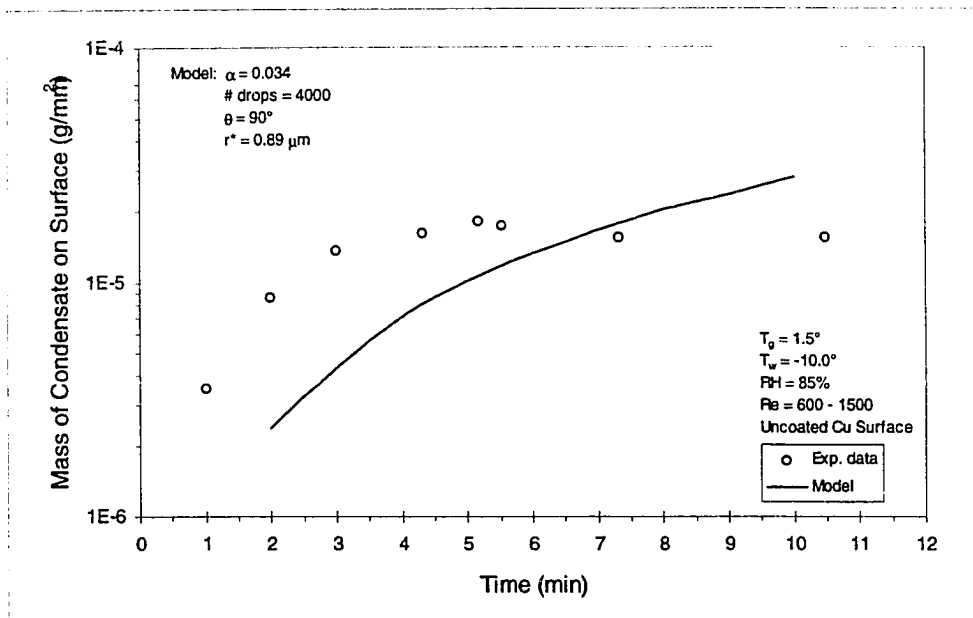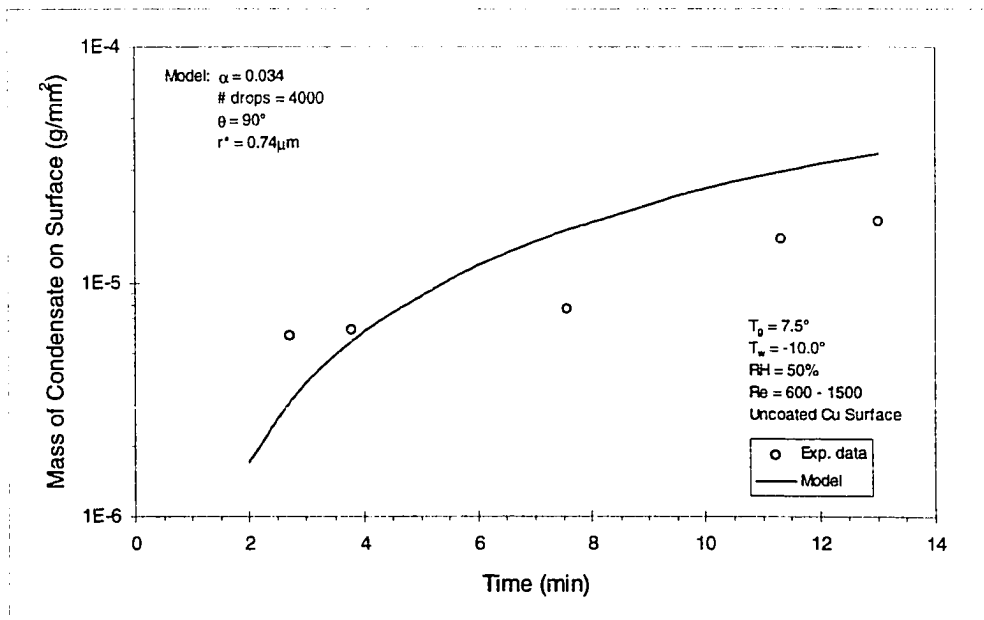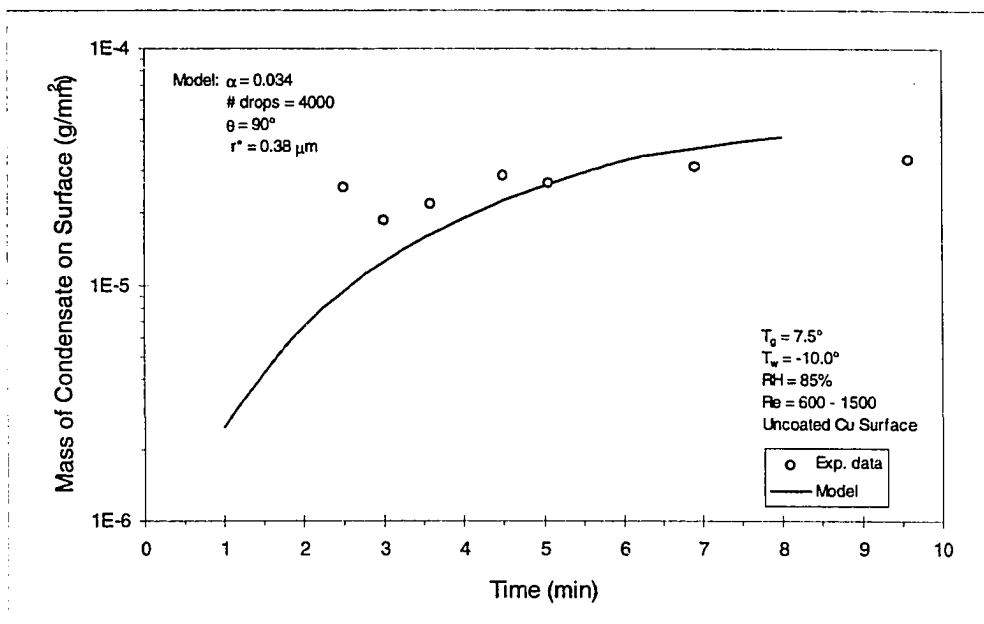

Figure A.3. Comparison of model to experimental data, uncoated copper surface,
$T_g = 7.5°$ C, 85%RH.
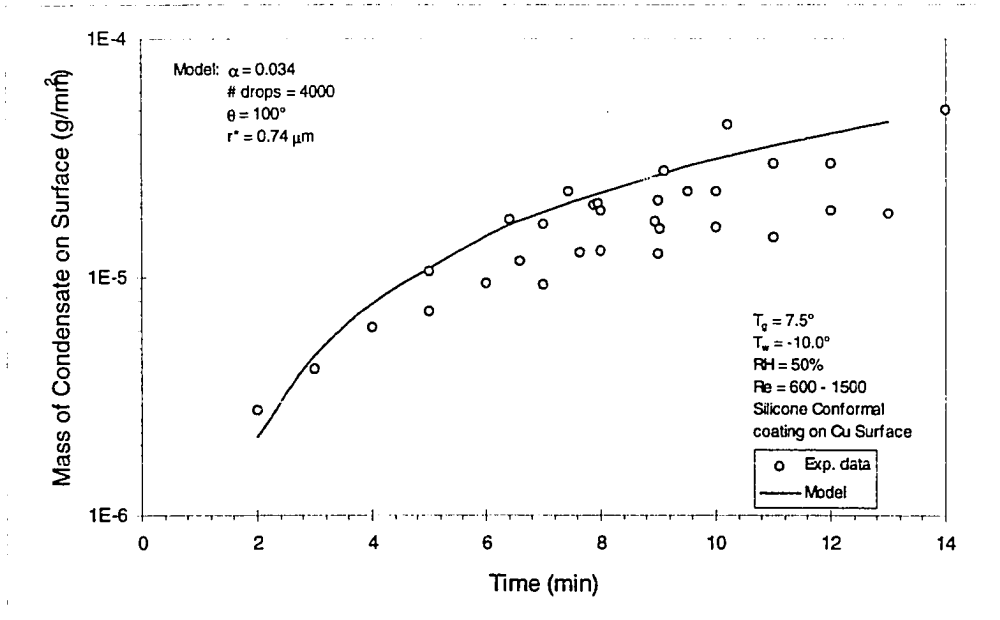
Figure A.4. Comparison of model to experimental data, silicone conformal coating on copper surface, T_g = 7.5° C, 50% RH.
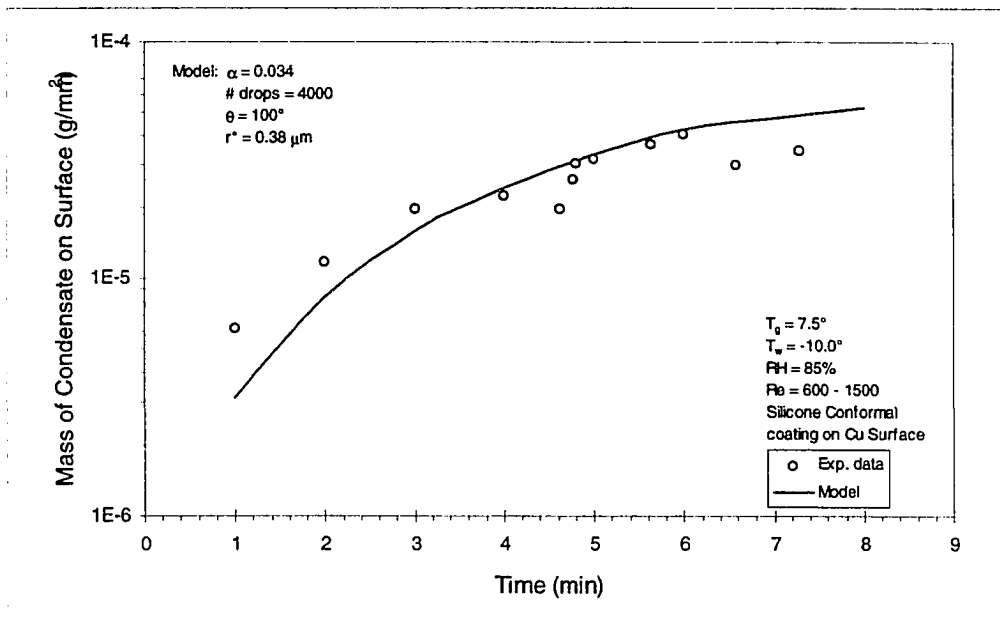
Figure A.5. Comparison of model to experimental data, silicone conformal coating on copper surface, T_g = 7.5° C, 85% RH.

Figure A.6. Comparison of model to experimental data, sulfur long-chain polymer coating on copper surface, $T_g = 1.5°$ C, 50% RH.

Figure A.7. Comparison of model to experimental data, sulfur long-chain polymer coating on copper surface, $T_g = 1.5°$ C, 85% RH.
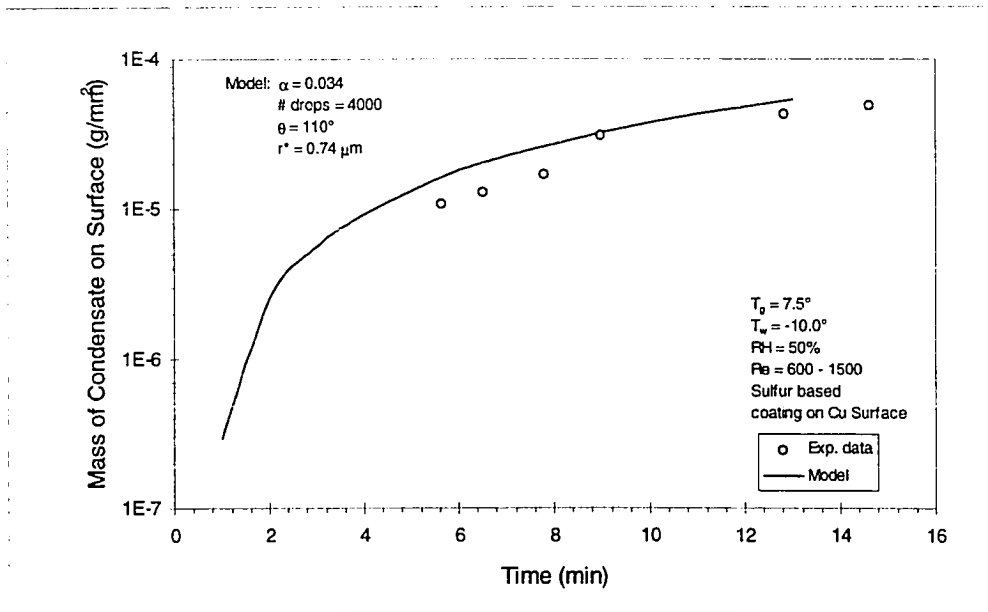
Figure A.7. Comparison of model to experimental data, sulfur long-chain polymer coating on copper surface, $T_g = 7.5°$ C, 50% RH.
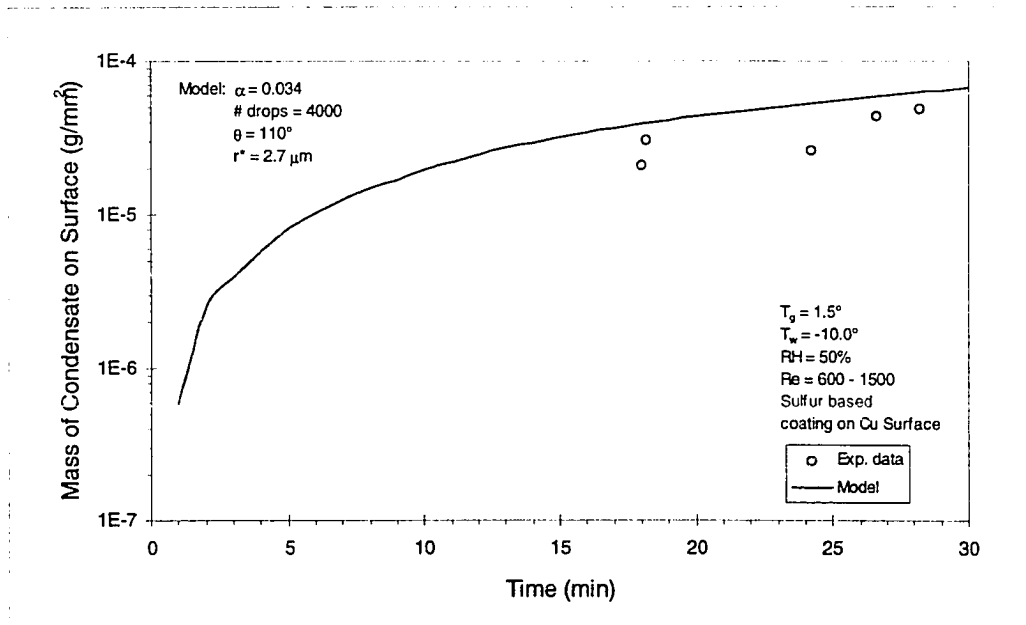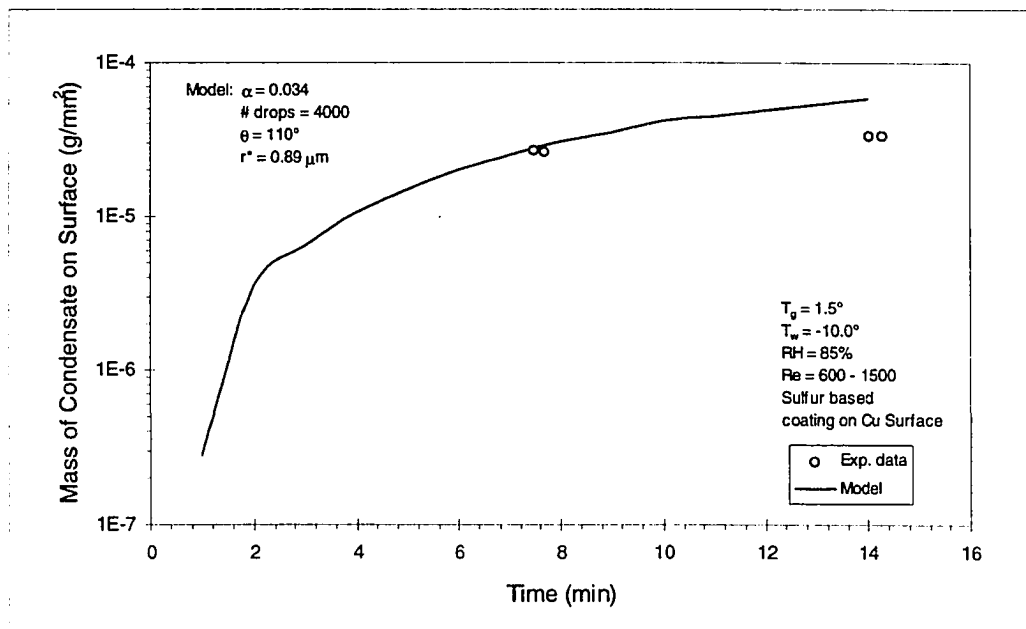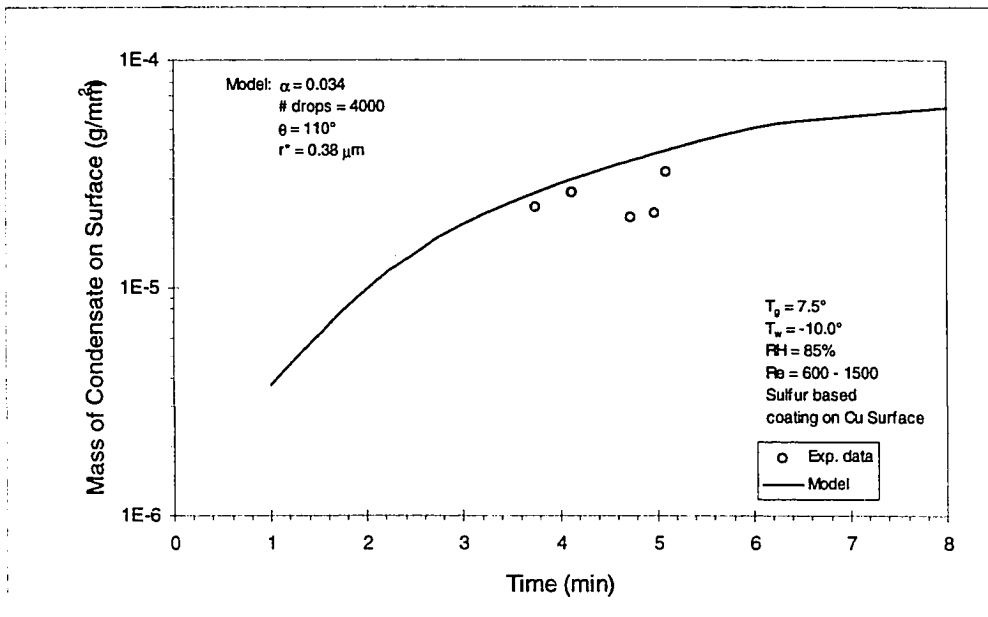

Figure A.8. Comparison of model to experimental data, sulfur long-chain polymer coating on copper surface, $T_g = 7.5°$ C, 85% RH.

APPENDIX B

Included in this appendix are printouts of the Engineering Equation Solver (EES) worksheet used to evaluate the droplet growth rate expressions and the TurboC simulation program code. Each of these printouts are "internally" documented.

Following is the EES droplet growth model (brackets { } indicate comments in EES).

{function block}

FUNCTION Psat(T)	{this is a saturation pressure for water vapor ASHRAE 1993, pg 6.7}

$c_8 := -5.8002206e3$
$c_9 := -5.516256$
$c_{10} := -4.8640239e-2$
$c_{11} := 4.1764768e-5$
$c_{12} := -1.4452093e-8$
$c_{13} := 6.5459673$
$Psat := exp(c_8/T + c_9 + c_{10}*T + c_{11}*T^2 + c_{12}*T^3 + c_{13}*ln(T))$
END

{Constants}

Rgas= 461	{287 for air, 481 for steam, 461 for moist air, gas constant J/kg K}
Tpl = 263	{plate temp. use as constant for simulations vs experimental}
Ti = (Tsat+Tpl)/2	{estimate for interface (liq - vap) temperature}
T1=274.5	{air temperature}
p1=101	{ambient pressure, varies with experiments}
rh1 = .5	{ambient relative humidity}
alpha = .034	{condensation coefficient, Atmospheric Sciences, is .4 for steam}

{Function calls}

Tsat = dewpoint(AIRH2O, t=T1,p=p1, R=rh1)   {Saturation temperature for
                                                    given conditions (K)}

Hsat = enthalpy(AIRH2O, t=T1,p=p1,R=1)   {enthalpy of saturated moist
                                                    air, (kJ/kg)}

Hair = enthalpy(AIRH2O, t=T1,p=p1, R=0)   {enthalpy of dry air,
                                                    (kJ/kg)}

Vair = volume(AIRH2O,t=T1,p=p1, R=rh1)   {sp vol of ambient air,
                                                    m^3/kg)}

Kliq = conductivity(WATER, t=((Tpl+Tsat)/2), p=p1) {thermal conductivity of
                                                    liquid water, W/mK}

Vliq = volume(WATER, t=Tpl, p=p1)   {sp volume of liquid water,
                                                    m^3/kg)}

W1 = humrat(AIRH2O, t=T1, p=p1, R=rh1)   {humidity ratio at given
                                                    conditons, (kgvap/kgda)}

Vl = volume(AIRH2O,t=T1,p=p1, R=1)   {volume of saturated
                                                    air/water vapor mix}

Vg = volume(AIRH2O,t=T1,p=p1, R=0)   {volume of air/water mix}

{heat and mass transfer Equations}

{cond. coeff. as function of radius, Chen, 1974}
{alpha = 1*exp(-2*PI*(R*1000000)^2*sig*1000/Rgas/Tsat)}

{surface tension of H2O in contact with its vapor (N/m), Cary pg.42}
sig =.2358*(1-Tsat/647.3)^1.256*(1-.625*(1-Tsat/647.3))

Pw=101*W1/(.62198+W1)   {water vapor partial pressure for ambient, (pa)}
Ps=Psat(Tsat)

Has = (Hsat-Hair)*1000   {latent heat of vaporization, (J/kg)}

{condensation rate on drop of radius R, (kg/m^2/s), Umur & Griffith, 1965}
wumur = ((2*alpha)/(2-alpha))*(9.81/2/pi/Rgas)^.5*(Psat(T1)/(T1^.5))*(1-
((Psat(Ti)/Psat(T1)))*exp(2*sig*Vliq/R/Rgas/Ti))

Hiumur = wumur*Has/(T1-Ti)   {Interfacial heat transfer coefficient,
                                     (W/m^2K) Umur & Griffith, 1965}

rcrit=2*sig*Vliq*Tpl/(Has*(Tsat-Tpl))   {Cary, pg. 346, and Tanaka, 1986}

{integral of drop growth equation}

{drop growth rate, (mm/s), Maa, 1983}
dRdt=((Tsat-Tpl)*Vliq/(Has))*((1-rcrit/R)/((1/(2*Kliq))+(1/Hiumur)))

{use 2*Rcrit for initial radius (Umur & Griffith)}
R=2*rcrit+INTEGRAL(dRdt, Time)

dRdtmic = dRdt*1000000   {get dRdt into microns}
Rmic = R*1000000   {get Radius into microns}

Following is the TurboC droplet growth and coalescing program (// indicates a comment).

// the following program was originally written by John Bryant in Quickbasic
// Mr. Curtis Boecker rewrote the original code in turboC, and I am indebted to him.

```
#include <stdio.h>
#include <stdlib.h>
#include <string.h>
#include <math.h>
#include <time.h>

#define MAXDIM 5000
#define MAXSIZE 700
#define TRUE    1
#define FALSE   0
//
// dimension arrays and define variables
//
FILE *fp;
char str[80];
float rad[MAXDIM];
float Xpos[MAXDIM];
float Ypos[MAXDIM];
float minx, maxx, miny, maxy;
float dist;
float dx, dy;
int snumber;          // site number
float initrad;
```

```
float GetF(char *txt)
{
    printf("%s",txt);
    gets(str);
    return (float)atof(str);
}

int GetI(char *txt)
{
    printf("%s",txt);
    gets(str);
    return (int)atoi(str);
}
// statements that generate the circles for the Postscript file output
//
void DrawCircle(float x, float y, float r)
{
    float X, Y, R;

    X = x/MAXSIZE*(maxx-minx)+minx;
    Y = y/MAXSIZE*(maxy-miny)+miny;
    R = r/MAXSIZE*(maxx-minx);
    fprintf(fp,"\n %8.3f %8.3f %8.3f c", X, Y, R);

}
//
// section to check for droplet coalescing
//
void Coalesce(int j, int k)
{
    float rj3, rk3, newrad;

    for(;k<snumber;)
    {
// calculate new radius, and determine index for new drop (j is new index)
        rj3 = rad[j]*rad[j]*rad[j];
        rk3 = rad[k]*rad[k]*rad[k];
        newrad = (float)pow( (rj3+rk3), 1.0/3.0 );
        if(rad[j]<rad[k])
        {
            rad[k] = newrad;
            rad[j] = 0.0;
```

```
                j=k;
            }
            else
            {
                rad[j] = newrad;
                rad[k] = 0.0;
            }
            for(k=0;k<snumber;k++)
            {
                if(rad[k]<initrad) continue;
                if(j==k) continue;
                dx = (float)(Xpos[j]-Xpos[k]);
                dy = (float)(Ypos[j]-Ypos[k]);
                dist = (float)sqrt( dx*dx + dy*dy );
                if ( dist < 0.95*(rad[j]+rad[k]) ) break; // coalesce these two
            }
        }
    }
}
//
// statements to write output files
//
void WriteFiles(int n)
{
    char basename[9];
    char fname[13];
    int i;

    sprintf(fname, "%da3.dat", n);
    fp = fopen(fname, "w");
    if(!fp)
    {
        printf("\nError Opening File %s", fname);
        exit(1);
    }

    for(i=0;i<snumber;i++)
        if(rad[i]>0.0) fprintf(fp,"%5d,  %12.4f\n", i, rad[i]);

    fclose(fp);

    sprintf(fname, "%da3.ps", n);

    fp = fopen(fname, "w");
```

```
    if(!fp)
    {
        printf("\nError Opening PostScript Output File!\n", fname);
        exit(1);
    }
//
// the next section is the header information for the Postscript file
//
    fprintf(fp,"%%!PS-Adobe-3.0 EPSF-3.0");
    fprintf(fp,"\n%%%%BoundingBox: 108 72 540 504");
    fprintf(fp,"%!DropDist");
    fprintf(fp,"\n%%PAGE HEADER START");
    fprintf(fp,"\n/d {lineto stroke} def");
    fprintf(fp,"\n/m {newpath moveto} def");
    fprintf(fp,"\n/c {newpath 0 360 arc stroke} def"); // draw circle
    fprintf(fp,"\n/xshow { dup stringwidth pop ");
    fprintf(fp,"-2 div 0 rmoveto show } def");
    fprintf(fp,"\n/yshow { dup stringwidth pop ");
    fprintf(fp,"-2 div 0 exch rmoveto ");
    fprintf(fp,"\n        90 rotate show -90 rotate } def");
    fprintf(fp,"\n/rshow { dup stringwidth pop neg 0 rmoveto show } def ");
    fprintf(fp,"\n72 72 scale"); // all units now in inches
    fprintf(fp,"\n0.0 setgray");
    fprintf(fp,"\n0.005 setlinewidth");
    fprintf(fp,"\n%%PAGE HEADER END");
    minx=1.5;maxx=7.5;
    miny=1.0;maxy=7.0;
    fprintf(fp,"\nnewpath");
    fprintf(fp,"\n%4.1f %4.1f moveto", minx, miny);
    fprintf(fp,"\n%4.1f %4.1f lineto", maxx, miny);
    fprintf(fp,"\n%4.1f %4.1f lineto", maxx, maxy);
    fprintf(fp,"\n%4.1f %4.1f lineto", minx, maxy);
    fprintf(fp,"\nclosepath stroke");

    for(i=0;i<snumber;i++)
        if(rad[i]>0.0) DrawCircle(Xpos[i], Ypos[i], rad[i]);

    fprintf(fp,"\nshowpage");

    fclose(fp);

}
```

```
void main(void)
{
//
// section that defines timestep, endtime, and print increment
//
    int i, j, k;
    int done;
    time_t t;
    float endtime;
    float timestep, Time, ptime=60.0;
    float rj3, rk3;
    float dtime=60.0;
    float x, drdt;


//
// section that allows user input of endtime, initial radius, timestep
// and number of initial droplets
//
    printf("\n\nJohns PhD Droplet Program\n");
    endtime = GetF("Enter End Time            ==> ");
    initrad = GetF("Enter Initial Droplet Radius ==> ");
    snumber = GetI("Enter Number of Sites        ==> ");
    timestep =GetF("Enter Time Step              ==> ");

    if(snumber>MAXDIM)
    {
        printf("\n\nToo Many Sites for Dimensions\n");
        exit(1);
    }

    srand((unsigned) time(&t));

    for(i=0;i<snumber;i++)
    {
        Xpos[i] = (float)(rand() % MAXSIZE);
        Xpos[i]+= (float)(rand() % 1000)/1000.0;
        Ypos[i] = (float)(rand() % MAXSIZE);
        Ypos[i]+= (float)(rand() % 1000)/1000.0;
        rad[i]  = initrad;
//      printf("\n%4d %10.4f  %10.4f  %10.4f", i, Xpos[i], Ypos[i], rad[i]);
    }

//
```

```
//  loops checking for distance between drops (coalescing) and
//  incrementing the time step
//
    for(Time=0.0;Time<endtime;Time+=timestep)
    {
        printf("\ntime is %f",Time);
        for(j=0;j<snumber;j++)
        {
            if(rad[j]<initrad) continue;
            for(k=j+1;k<snumber;k++)
            {
                if(rad[k]<initrad) continue;
                dx = (float)(Xpos[j]-Xpos[k]);
                dy = (float)(Ypos[j]-Ypos[k]);
                dist = (float)sqrt( dx*dx + dy*dy );
                if ( dist < 0.95*(rad[j]+rad[k]) )
                {
                    Coalesce(j, k);
                    break;
                }
            }
        }


    }


//
//  the next section contains the curve-fit equation for radial
//  droplet growth. these equations used data were that were
//  generated in the EES simulation.  a curvefit program was used
//  to develop a best fit of the data. the designation of, for
//  example, 785 indicates a curvefit for droplet growth with a
//  7C air temperature and 85% RH.
//

        for(i=0;i<snumber;i++)
          if(rad[i]>0.0)
          {
                x = (-1.469 + 10.778*rad[i])/(1.0 - 3.3145*rad[i]);
//  eqn for 185hi x = (-1.10231 + 14.268*rad[i])/(1.0 - 4.8869*rad[i]);
//  eqn for 185mid x = (-1.27 + 12.536*rad[i]) / (1.0 - 4.077*rad[i]);
//  eqn for 750  x = (-1.35189 + 15.503*rad[i]) / (1.0 - 4.915*rad[i]);
//  eqn for 785  x = (-0.538 + 23.706*rad[i]) / (1.0 - 9.8425*rad[i]);
//  eqn for 150  x = (-2.6743 + 5.2567*rad[i]) / (1.0 - 1.2299*rad[i]);
```

```
                drdt = exp(x);
                rad[i] += drdt*timestep;
            }
//
//  section to write files at one minute increments of the simulation
//
        if(Time>=ptime)
        {
          WriteFiles((int)Time);
          ptime+=60.0;
        }

        if(Time>dtime)
        {
          for(i=0;i<snumber;i++)
                if(rad[i]==0.0) rad[i]=initrad;
          dtime+=30.0;
        }

    }
}
```

VITA

John Arthur Bryant was born in Jersey City, New Jersey on October 6, 1954. His parents are Frank and Florence Bryant. He married Elizabeth Rister in August, 1977, and has one son, Stephen.

He graduated from Roswell High School, Roswell, New Mexico, in 1972 and joined the U.S. Army in January, 1973. After serving three years in Germany, he returned to New Mexico. He attended New Mexico State University in Las Cruces, New Mexico and graduated in December, 1982. He worked as a construction engineer with the Veteran's Administration before returning to New Mexico State University to teach in the Department of Engineering Technology. While with the Department of Engineering Technology, he completed his master's degree in Mechanical Engineering from the University of Texas at El Paso in 1987. He joined a mechanical consulting firm in El Paso and also worked for an HVAC controls company before coming to Texas A&M to work on his doctoral degree. At present, he is a visiting professor in the Mechanical and Industrial Engineering Department at the University of Texas at El Paso.

His interests include instrumentation, single and two-phase heat transfer, HVAC system design, operation, and control, and building energy conservation. He has published numerous papers on building energy use monitoring and instrumentation.

His permanent mailing address is:

John A. Bryant

719 Espolon

El Paso, Texas 79912